國　立　交　通　大　學

電機與控制工程研究所

碩士論文

利用聚焦離子束製作之 Fresnel 微透鏡

Fresnel Microlens Fabrication by Focused Ion Beam Milling

研 究 生：黃 建 勳

指導教授：邱 一　博士

中華民國九十五年十月

利用聚焦離子束製作之 Fresnel 微透鏡

Fresnel Microlens Fabrication by Focused Ion Beam Milling

研 究 生：黃建勳 Student: Chien-Hsun Huang

指導教授：邱 一 Advisor: Yi Chiu

國立交通大學 電機學院

電機與控制工程研究所

碩士論文

A Thesis
Submitted to Department of Electrical and Control Engineering
College of Electrical and Computer Engineering
National Chiao Tung University
In Partial Fulfillment of the Requirement
For the Degree of
Master
In

Electrical and Control Engineering

October 2006

Hsinchu, Taiwan, R.O.C.

中華民國九十五年十月

中文摘要

隨著資訊科技的進步，高容量及高速度的資料存取的需求和重要性亦顯著增加，而光儲存科技在裡面扮演著極為重要的角色，其中，對於光儲存系統的效能，光學讀取頭的設計有著舉足輕重的影響力。

微型化和輕量化的要求推動了更小更輕的光學資料儲存系統的發展；近年來，微機電製程技術在 IC 半導體產業的快速進展之下有了重大的發展，而利用微光機電技術製作之微光學讀取頭乃是實現可攜式且高容量的光儲存系統的途徑之一。在本研究中，微光學讀取頭是由微光學平台及固定在雙軸致動器的聚焦透鏡所組成的，其中的聚焦透鏡正是本論文研究的主要方向。

本論文中所提及到的微透鏡有兩種：一種為直接利用聚焦離子束蝕刻氮化矽薄膜所製作出來的 Fresnel 微透鏡，此種微透鏡是以氮化矽做為材質；而另一種則是利用接觸式的黃光微影技術，配合著聚焦離子束所產生的灰階光罩，所製作出來的 Fresnel 微透鏡，此種微透鏡是以正光阻 AZ4620 為材質，而灰階光罩的材質則是以氮化矽為主。

關於微透鏡及灰階光罩的表面形貌和厚度大小已經設計完成，而其製作程序亦於此論文中被提出；另外，利用原子力顯微鏡進行其二維及三維的量測。對直徑大小為 20 微米的氮化矽微透鏡進行量測，其數值孔徑約為 0.64，近似於 DVD 讀取頭的規格要求。本研究的最終目標是欲在微光學讀取頭中，實現一個整合於微光學平台之微透鏡，而其直徑大小為 600 微米，數值孔徑為 0.65。

Abstract

With the progress of information technology, the demand and importance of high capacity and high speed data storage systems rise significantly. In data storage systems, optical data storage technology plays a key role. Moreover, the design of optical pick-up heads has great influence in the performance of the optical data storage system.

The requirement of miniaturization and lightness pushes the development of more miniaturized and lighter optical data storage system. Recently, the Micro Electro Mechanical Systems (MEMS) technology has been developed greatly with the rapid progress in the IC semiconductor industry. Micro optical pick-up heads fabricated by Micro-Opto-Electro-Mechanical System (MOEMS) technology can be used to realize portable high-capacity optical storage systems. In this research, the micro optical pick-up head is composed of a micro optical bench and a focusing lens mounted on a two-axis actuator. The study of focusing lenses is the major topic in this thesis.

Two kinds of focusing lenses are proposed in this thesis. One is the Fresnel microlens in silicon nitride fabricated by focused ion beam (FIB) milling. The other one is the Fresnel microlens in positive photoresist AZ4620 produced through the contact-mode photolithography with the FIB-milled gray scale mask in silicon nitride.

The profile and thickness of the microlenses and gray-scale masks have been designed. The fabrication process has also been proposed. 2D and 3D profiles of the lenses and masks were measured by the atomic force microscopy (AFM). For the microlens in nitride with a diameter of 20 μm, the numerical aperture (N.A.) of the lens was measured as 0.64, close to the specification of a DVD optical pick-up head. The ultimate target of this research is to realize a focusing microlens with a diameter of 600 μm and N.A. of 0.65, integrated with the micro optical bench in a micro pick-up head.

致謝

轉眼間，碩士班的研究生涯結束了！一路上，縱使遇到了許多的挫折和困難，最後還是完成了我的研究，而在這充滿歡笑和淚水的過程中，有許許多多的感謝存在著；首先，要感謝的是我的指導教授邱一博士，他總是能給我很多專業的指導跟建議，在我遇到研究瓶頸時，能夠指引我正確的方向，啟發了我最正確的研究精神和態度，我相信在老師的指導之後，必定能在未來有所發展，在這邊真心地向老師說聲:「老師，謝謝您！」

再來，我要感謝的是實驗室的成員們；感謝實驗室的學長姐 俊毅、嘉豪、依纖、志偉、育杉、文中和英傑，謝謝你(妳)們在實驗的過程中，傳授我研究上許多實用的經驗和建議；感謝和我一起奮鬥的同學 忠衛、均宏、炯廷和亦謙，和你們一起在實驗室打拼的回憶，是我一輩子都不會忘記的；感謝總是帶給我歡笑的學弟 繁果、煒智、昇儒、子麟、弘諳和昌修，你們總是可以在我研究辛勞的時候，給我最大的助力和鼓勵；另外，要感謝和我同實驗室的邱俊誠教授的學生 修權、修涵、子毅、祐任、文凱、一凡、亞書、建賢、基恩和嘉宏，有你們的研究生涯中，增加了更多值得回味的回憶；特別要感謝的是及光電所的 企桓學長、機械所的志柏 同學及清大動機所的 宗霖學弟，謝謝你們在我實驗中給我不少的建議和幫忙，使我的研究更加地順利。

最後，要感謝的是我的父母和兄妹，因為有你(妳)們，總是能在我遇到研究瓶頸時，給我最佳的支持和鼓勵，讓我在全世界最幸福可靠的避風港裡，得到最舒適的休息；特別要感謝的是，我可愛的女友 筱雯，妳那可愛又充滿溫暖的微笑，總是在我最挫折的時候，給我最大的鼓勵，謝謝妳！最後的最後，讓我再次表達我的感謝，謝謝你(妳)們，有你(妳)們的回憶會是我最重要的寶物！

黃建勳 謹識

中華民國九十五年十月

新竹 交大

Table of Content

中文摘要……………………………………………………………………………i

Abstract……………………………………………………………………ii

誌謝………………………………………………………………………iii

Table of Content…………………………………………………………iv

List of Figures……………………………………………………………vi

List of Tables……………………………………………………………ix

Chapter 1 Introduction…………………………………………………1

1-1 Motivation……………………………………………………………1

1-2 Microlens……………………………………………………………4

1-2-1 Refractive Microlens………………………………………………4

1-2-2 Diffractive Microlens………………………………………………7

1-2-3 Gray Scale Mask……………………………………………………10

1-3 Focused Ion Beam System…………………………………………14

1-4 Objectives and Thesis Overview……………………………………19

Chapter 2 Principle and Design………………………………………21

2-1 Material Properties …………………………………………………21

2-1-1 Photoresist AZ4620………………………………………………21

2-1-2 Silicon Nitride……………………………………………………25

2-2 Fresnel Microlens Design……………………………………………27

2-3 FIB Pattern Design…………………………………………………32

2-3-1 Fresnel Microlens Pattern…………………………………………32

2-3-2 Gray Scale Mask Pattern…………………………………………33

2-4 Summary……………………………………………………………35

Chapter 3 Fabrication Process……………………………………………………...37

3-1 FIB Milling of Silicon Nitride.……………………………………..…….37

3-2 Microlens in Photoresist………………………………………..……..39

3-3 Summary……………………………………………………...………..41

Chapter 4 Measurement and Experiment……………………..………………...42

4-1 Test Pattern Measurement…………………………………...…………42

4-2 Microlens and Mask Pattern Measurement……………..………………...48

4-3 Optical Experiment…………………………………..………………...59

4-4 Summary…………………………………………………………..……..63

Chapter 5 Conclusion and Future Work…………………………………..……..64

5-1 Conclusion…………………………………………………….…………64

5-2 Future Work……………………………………………………….……...64

References…………………………………………………………………….......65

List of Figures

Figure 1-1 Conventional optical pick-up head……………….……………………...…2

Figure 1-2 SEM micrograph of the free-space integrated optical pick-up head…...…3

Figure 1-3 Diagram of the MEMS-based optical pick-up head…………………....…3

Figure 1-4 Different types of optical functions………………….……………….....…4

Figure 1-5 Reflow process of the microlens……………………..……………....…5

Figure 1-6 SEM micrograph of the refractive microlens (diameter: 300 μm)…....….6

Figure 1-7 SEM micrographs of a microlens array cured by UV light…….……...…6

Figure 1-8 SEM micrographs of mirolens arrays fabricated in fused silica……....…6

Figure 1-9 Blazing of a lens resulting in a reduced thickness…………………......…8

Figure 1-10 Schematic diagrams of (a) a continuous Fresnel zone plate and (b) a multiple-level binary microlens……………………………………………9

Figure 1-11 Fabrication process of a four level microlens by the binary method….…9

Figure 1-12 SEM micrograph of the out-of-plane micro-Fresnel lens........…………...10

Figure 1-13 Schematic diagram of a three-level gray-scale mask pattern and the resulting photoresist structure………….……………………………...11

Figure 1-14 SEM of the three gray levels patterned in AZ4620 photoresist resulting from a similar mask pattern in Figure 1-13……………..…..………….....11

Figure 1-15 Optical micrograph of the gray-scale mask……………………..……...12

Figure 1-16 SEM of a diffractive optical element in a quartz substrate……………..12

Figure 1-17 (a) A laser direct-writing gray-scale microlens mask and (b) the etched 16-level microlens structure……………………………………………...13

Figure 1-18 Schematic diagram of a basic FIB system……………………………...15

Figure 1-19 Schematic diagram of the basic FIB column…………………………...16

Figure 1-20 Schematic diagram of a dual-beam FIB column arrangement………....16

Figure 1-21 Diffractive lens on silicon by use of FIB milling. It was characterized by the AFM with a tapping mode. (a) 2D profile in the horizontal direction. (b) SEM micrograph of the fabricated device…………………….………...17

Figure 1-22 SEM micrograph of the nano wine glass made by FIB milling……...18

Figure 2-1 Solubility versus the transmittance for the photoresist samples…………23

Figure 2-2 Solubility versus the transmittance for AZ4620………………………....24

Figure 2-3 (a) Refractive index and (b) extinction coefficient of LPCVD nitride......26

Figure 2-4 Schematic diagram of N.A.………...…………………………………....27

Figure 2-5 Schematic diagram of microlens design………………………………....29

Figure 2-6 Profile of the silicon nitride microlens………………..………………...31

Figure 2-7 Profile of the AZ4620 microlens……………………...………………....33

Figure 2-8 Gray-scale pattern of the nitride microlens in 512×512 pixels..............…33

Figure 2-9 Gray-scale pattern transfer………………………………….…………....35

Figure 2-10 Gray-scale mask pattern for the AZ4620 microlens in 512×512 pixels..35

Figure 3-1 Schematic diagram of the fabrication process…………..……………....38

Figure 3-2 SEM micrograph of the KOH etching process………......……………....38

Figure 3-3 SEM micrograph of the (a) microlens and (b) gray-scale mask………....39

Figure 3-4 Schematic diagram of the exposure process……….........……………....40

Figure 3-5 OM micrograph of the microlens in AZ4620 of diameter 35 μm……......41

Figure 4-1 SEM micrograph of the test pattern. (Conditions: 480x and 0.3 nA)…....44

Figure 4-2 AFM profile result of the test pattern……………..…......……………....44

Figure 4-3 Diagram of the spot profile…………......……………………..……......45

Figure 4-4 Ion-milled spot size versus beam current for various dwell time for 1200x magnification……………………………………….........……………....45

Figure 4-5 Actual distance versus pixel step size for various beam current for (a) 480x and (b) 1200x magnification…………………......……………....46

Figure 4-6 Depth versus dwell time for various beam current for (a) 480x and (b) 1200x magnification…………………………………...…………....47
Figure 4-7 Depth versus pixel step size for various dwell time for 1200x magnification and beam current of 1 nA…………….......…………....48
Figure 4-8 AFM measurement of the (a) middle region and (b) right-side region of the microlens pattern of diameter 100 μm……………....……….……....49
Figure 4-9 AFM measurement of the (a) middle region and (b) right-side region of the microlens pattern of diameter 50 μm………......……..…..……....50
Figure 4-10 AFM profile of the microlens pattern of diameter 50 μm……..……....51
Figure 4-11 AFM measurement of the microlens pattern of diameter 20 μm……....52
Figure 4-12 AFM measurement of the (a) middle region and (b) left-side region of the mask pattern of diameter 30 μm………………………..….……....53
Figure 4-13 AFM profile of the mask pattern of diameter 30 μm…………..……....54
Figure 4-14 2D profile of the (a) microlens and (b) gray-scale mask……….……....55
Figure 4-15 3D profile of the (a) microlens and (b) gray-scale mask……….……....56
Figure 4-16 Roughness of the (a) microlens and (b) gray-scale mask………………57
Figure 4-17 Comparison between the measured profile and designed profile for the silicon nitride microlens of diameter 20 μm…………….…………....58
Figure 4-18 Comparison between the measured profile and designed profile for the gray-scale mask of diameter 35 μm…………………………...……....58
Figure 4-19 Pattern size versus milled depth……………………………..……....59
Figure 4-20 Schematic diagram of the optical measurement……………..……....60
Figure 4-21 Image of the focused spot on the CCD camera…………..…………....61
Figure 4-22 Intensity profile of the focused spot………...……………………......61
Figure 4-23 Cross-section of the intensity profile in (a) the horizontal direction and (b) the vertical direction…….……..……………………………………......62

List of Tables

Table 2-1 Focal length calculation……………….....……………….……………...…28

Table 2-2 Calculated results of the silicon nitride microlens…..……………...…...…30

Table 2-3 Calculated results of the AZ4620 microlens………...….………………...…30

Table 2-4 Calculated results of sliced silicon nitride microlens…...……………...…31

Table 2-5 Calculated results of sliced AZ4620 microlens…………...……………...…31

Chapter 1 Introduction

1-1 Motivation

With the progress of the information technology, the demand and importance of data storage systems rise significantly. Due to the rapid growth of data and the trend of removable media, the high-capacity optical data storage systems are the focus of development. Therefore, the systems evolve from CD to DVD to become a high-capacity and removable storage system. The design of optical pick-up heads plays a key role and has great influence in the performance of the optical data storage system.

Figure 1-1 is the schematic of a conventional optical pick-up head. The optical pick-up head is composed of a laser diode, grating plates, a polarizing beam splitter, a collimator, a quarter wave plate, a 45° mirror, an objective lens, and photodiodes. The working principle of the optical pick-up head is that the laser emitted from the laser diode passes through the grating plates to produce two secondary beams in order to maintain the precise tracking of the light-spot. The beam passes through the polarizing beam splitter and is converted into a parallel beam by the collimator. Then, the beam becomes circularly polarized when passing through the quarter wave plate, and is focused on the surface of the disk (i.e., CD or DVD) by the objective lens after being reflected by the 45° mirror. The reflected beam from the disk becomes orthogonally linearly polarized with regard to the source beam after passing through the quarter wave plate and is reflected by the polarizing beam splitter into the detection photodiodes.

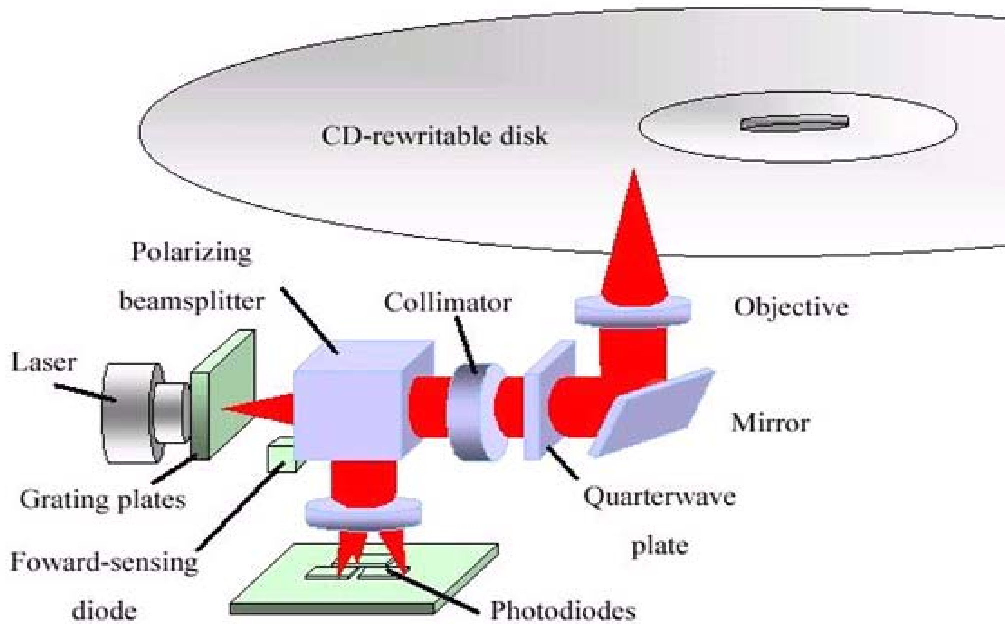

Figure 1-1: Conventional optical pick-up head

In conventional optical pick-up heads, a number of optical components are needed to detect the optical information signal. As a result of using discrete components, it becomes inevitably thick and large. Compared with the conventional pick-up head, miniaturized devices have the characteristics of shorter response time, less power consumption, and smaller size. In the trend of miniaturization, the Micro-Electro-Mechanical System (MEMS) is an appropriate choice since MEMS is a technology employing the semiconductor fabrication process to minimize electro-mechanical devices. Furthermore, MEMS devices can be integrated with signal processing circuits on the same chip, such as CMOS-MEMS technology, to reduce the noise interference and signal distortion.

Figure 1-2 is a monolithic free-space optical pick-up head developed by M. C. Wu et al. [1]. The pick-up head contains a semiconductor edge-emitting laser, a beam splitter, three miro-Fresnel lens (including one collimating lens and two focusing lenses), and two 45° reflective mirrors. All optical components are built

monolithically on the silicon substrates.

For a full functional micro optical pick-up head, the objective lens and/or the micro-actuator must be included, as shown in Figure 1-3. In this thesis, the micro objective lens in the optical pick-up head is the major topic. For a DVD application, the numerical aperture (N.A.) of the lens is 0.65.

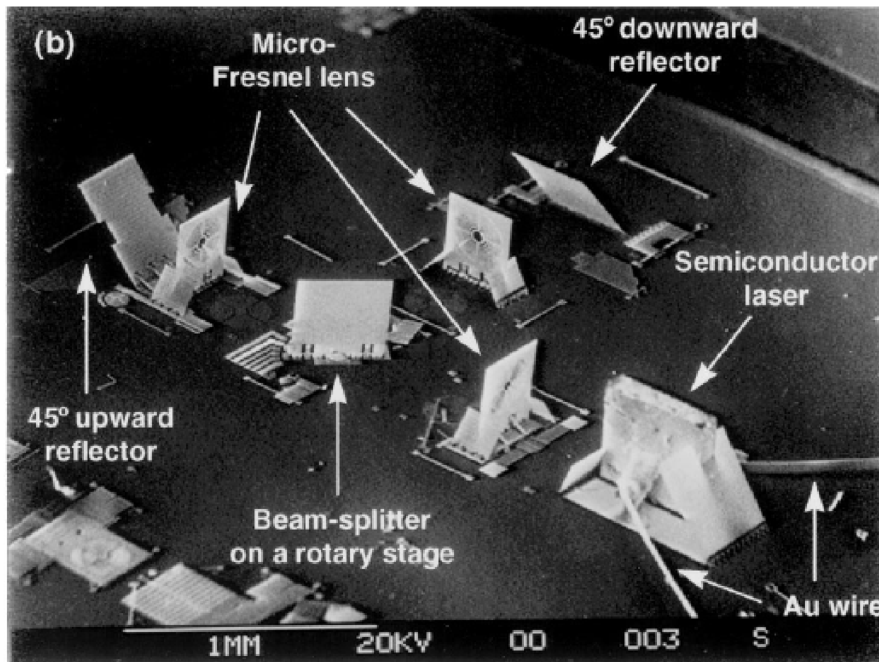

Figure 1-2: SEM micrograph of the free-space integrated optical pick-up head. [1]

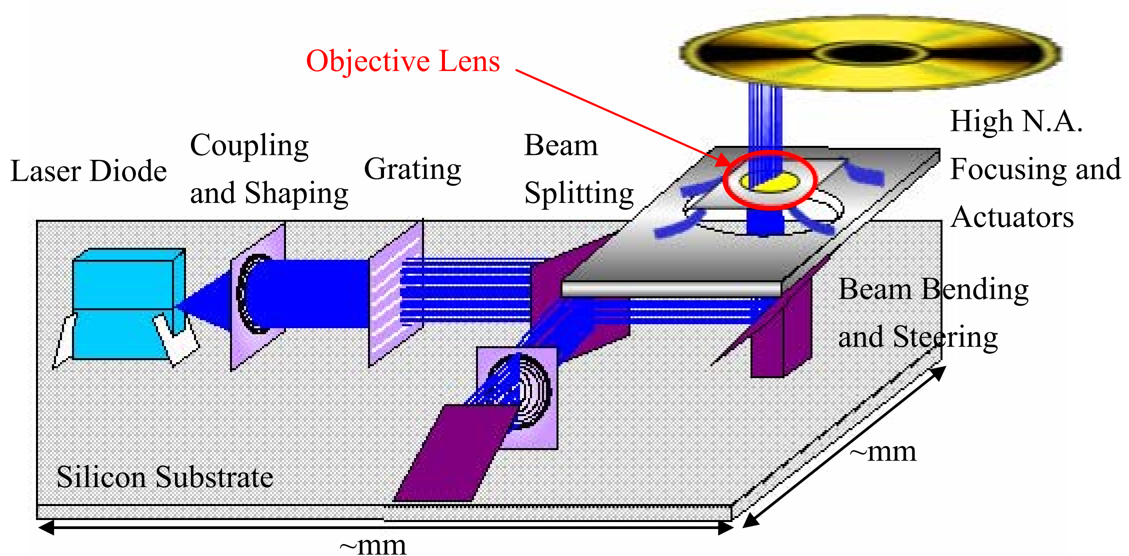

Figure 1-3: Diagram of the MEMS-based optical pick-up head.

1-2 Microlens

There are three types of focusing microlens in the micro-optics, namely the refractive type, the reflective type, and diffractive type, as illustrated in Figure 1-4 [2]. Among them, the refractive and diffractive microlens will be discussed in this section. In addition, different fabrication processes of the microlens developed in the past are also discussed in this section.

1-2-1 Refractive Microlens

A great variety of fabrication techniques have been applied to the fabrication of refractive optical elements (ROEs). Fabrication of refractive microlenses is often based on some analog physical process. Due to the analog nature of most fabrication techniques used for ROEs, their fabrication is often more difficult compared to the fabrication of diffractive optics. However, even the difficulties in the fabrication of refractive microlenses, the reflow methods have been used to fabricate the refractive microlens successfully.

In the reflow process shown in Figure 1-5, the photoresist is first spin-coated on the silicon substrate to the thickness necessary to produce lenses of given focal length when melted. Then, photolithography is used to define the pattern size of the microlens. Finally, heat is applied to melt the photoresist so that surface tension causes the resist to adopt a hemispherical form, and the microlens is completed.

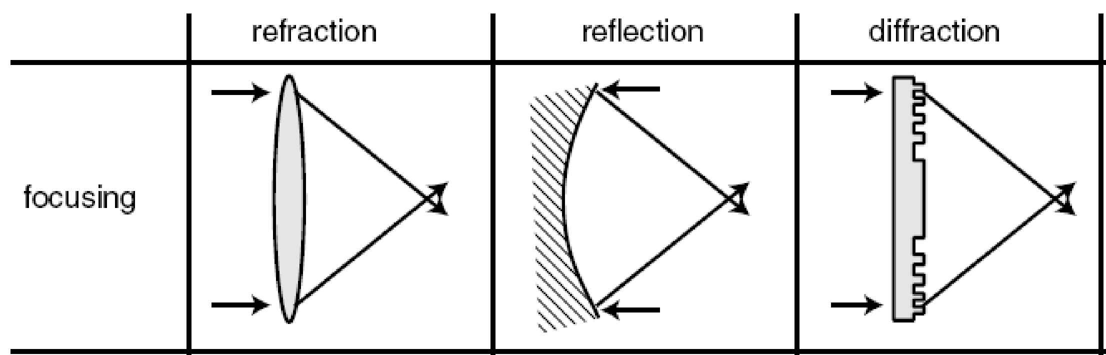

Figure 1-4: Different types of optical functions. [2]

Although the reflow process is simple, the focal length of the microlens is difficult to control. Figure 1-6 shows an out-of-plane refractive microlens fabricated with the reflow technique and mounted on a surface-micromachined vertical plate [3].

Refractive microlens can also be made from the pre-shaped photoresist by a laser direct write technique [4], the droplets method [5], as shown in Figure 1-7, or the ink-jet process [6]. Furthermore, the refractive microlens pattern can be transferred to the substrate by accurately controlling the substrate-to-photoresist etch selectivity in reactive ion etching (RIE). Figure 1-8 shows a F-number 4.2, 200 μm diameter microlens array and a F-number 0.86, 80 μm diameter linear microlens array in fused silica [7].

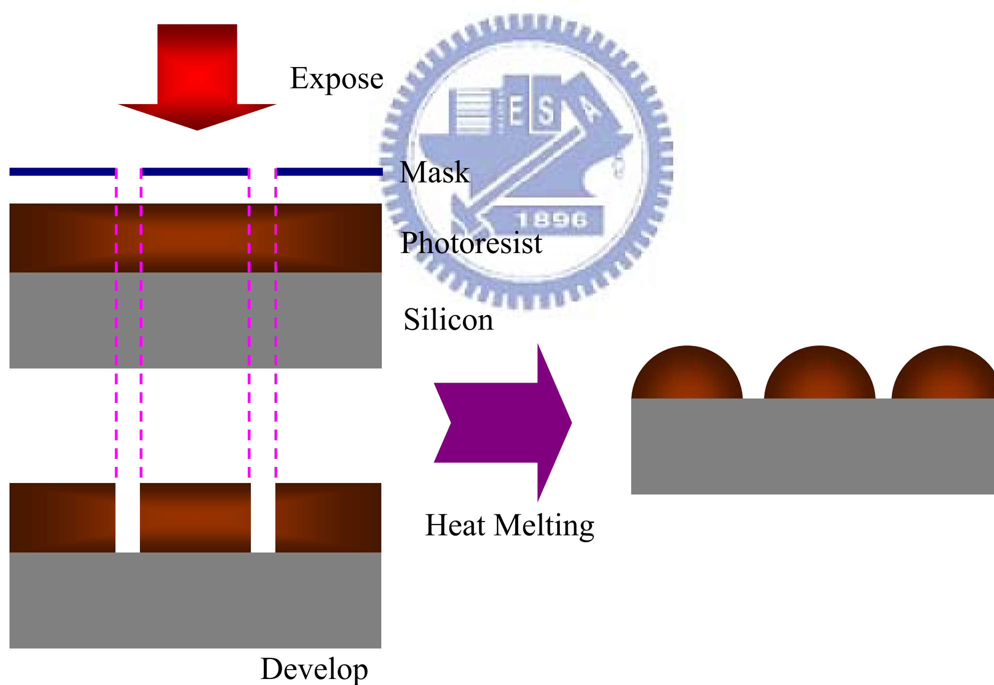

Figure 1-5: Reflow process of the microlens.

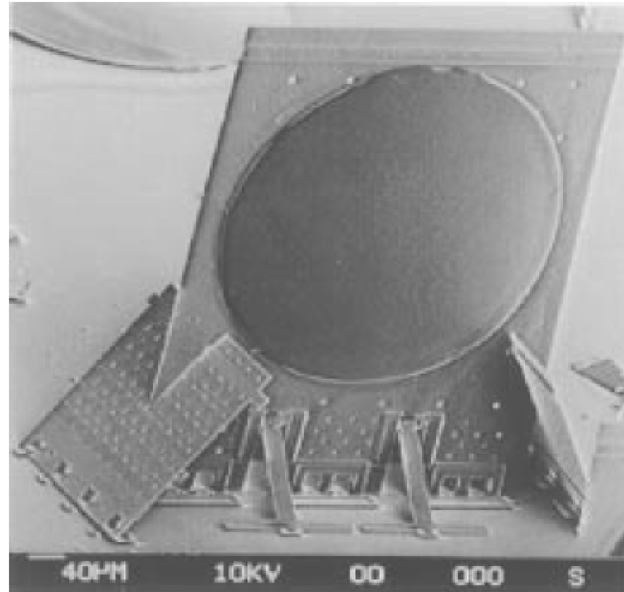

Figure 1-6: SEM micrograph of the refractive microlens (diameter: 300 μm). [3]

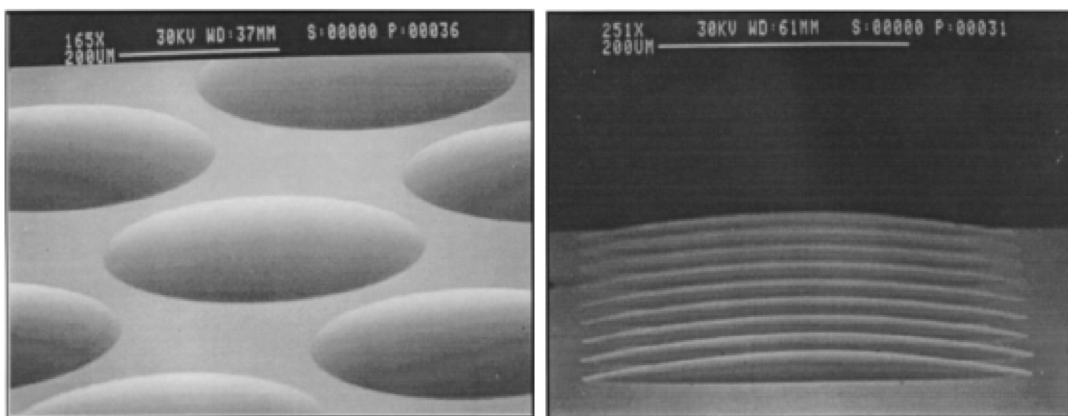

Figure 1-7: SEM micrographs of a microlens array cured by UV light. [5]

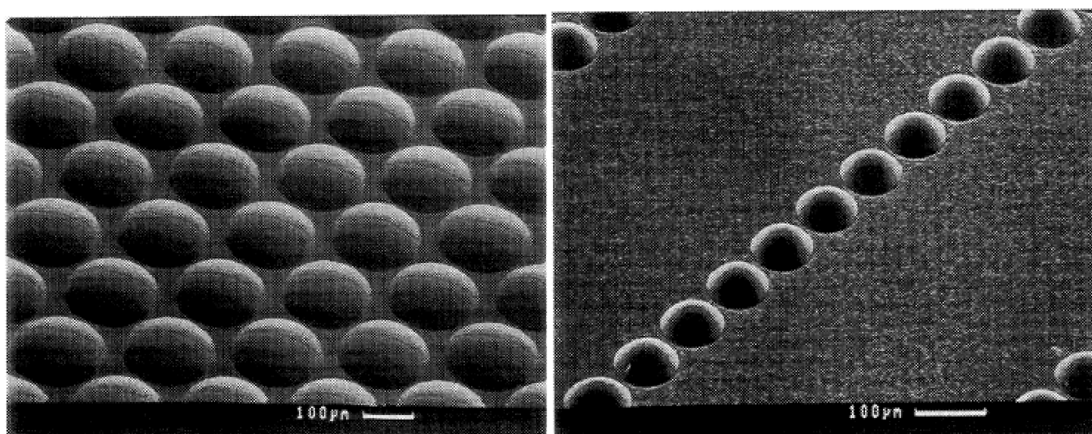

Figure 1-8: SEM micrographs of mirolens arrays fabricated in fused silica. [7]

1-2-2 Diffractive Microlens

In conventional macrooptics, the use of refractive elements dominates, while diffractive elements are only used in spectroscopy mostly. However, diffraction plays a much stronger role in microoptics. Diffractive optics can be viewed as an approach to the fabrication optimized for the lithographic techniques. In ROEs, the light is manipulated by analog phase elements of considerable thickness in relation to the optical wavelength. For micro components, such as aspheric lenses, in particular, the fabrication is impossible with mechanical profiling techniques (due to the small lateral extension) and very challenging with microlithography (due to the large phase depth of the component). The solution to the fabrication problem lies in the periodic nature of the light wave *U(x)*. If a light wave is delayed by one wavelength (corresponding to a phased lag of $\varphi=2\pi$), no difference to the original wave can be found, due to

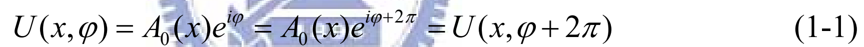

$$U(x,\varphi)=A_0(x)e^{i\varphi}=A_0(x)e^{i\varphi+2\pi}=U(x,\varphi+2\pi) \qquad (1\text{-}1)$$

For example, retardation occurs when the wave passes through a dielectric material (e.g., glass or photoresist). The insensitivity of the light wave to phase jumps of $2N\pi$ (N is an integer) allows one to reduce the thickness of an optical element without changing its effect on a monochromatic wave. In transmission the maximum thickness of the corresponding optical component can be reduced to

$$t_{\max}=\frac{\lambda}{n-1} \qquad (1\text{-}2)$$

where n denotes the refractive index of the component material and λ is the wavelength of the incident light, as shown in Figure 1-9. The blazing of continuous phase functions results in laterally periodic elements, and such profiling depths are readily fabricated with lithographic techniques.

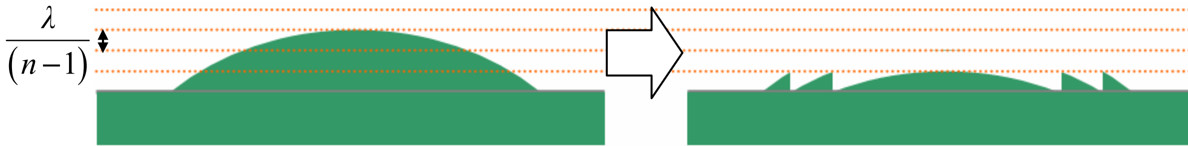

Figure 1-9: Blazing of a lens resulting in a reduced thickness.

Diffractive microlenses are very attractive for integration with free-space micro-optical bench (FS-MOB) because:

(a) their focal length can be precisely defined by photolithography;

(b) microlenses with a wide range of N.A. values can be defined;

(c) microlenses with diameters as small as a few tens of micrometers can be made;

(d) their thickness is on the order of an optical wavelength [8].

The thin construction is particularly suitable for the surface micromachining process because the thicknesses of the structure layers are only on the order of 1 μm.

There are two types of diffractive microlenses, one is the continuous kinoform lens, i.e., the Fresnel lens, and the other is the multiple-level binary microlens, as shown in Figure 1-10. Fabrication of binary microlenses on the silicon substrate has already been demonstrated. In the multiple-level microlenses, $\log_2 n$ masks are needed for the n-level lens. The fabrication steps of a four-level microlens are shown in Figure 1-11 as an example. In order to achieve better approximation of the lens, the number of levels should be as many as possible. The precision of the alignment is the key point in the method when the number of levels increases. Therefore, the complexity and the misalignment are the drawbacks of the process. Figure 1-12 shows the SEM micrograph of a binary micro-Fresnel lens with a diameter of 280 μm, a focal length of 500 μm, and an optical axis which is 254 μm above the silicon surface.

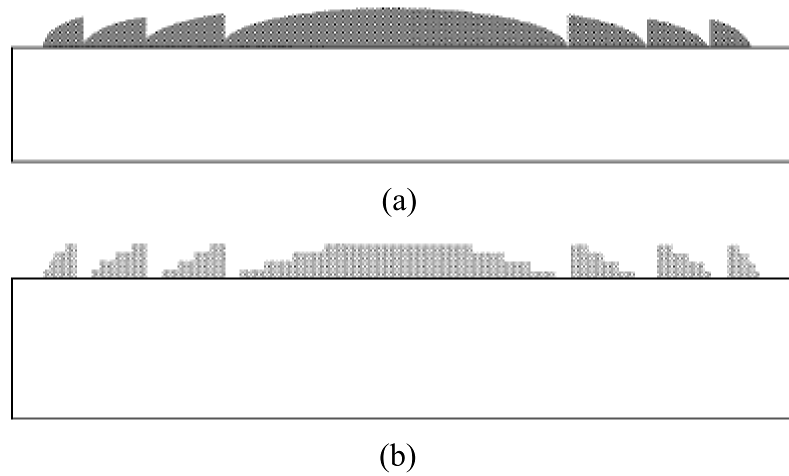

Figure 1-10: Schematic diagrams of (a) a continuous Fresnel zone plate and (b) a multiple-level binary microlens. [8]

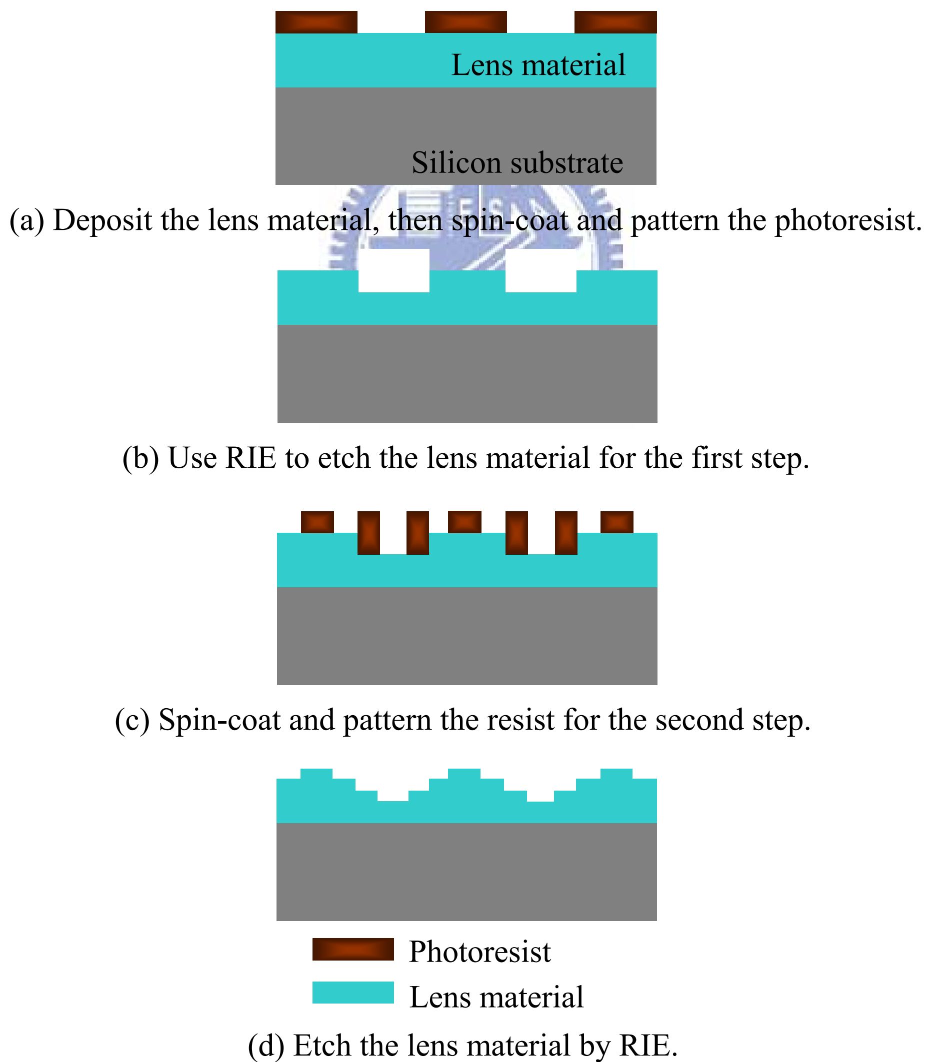

(a) Deposit the lens material, then spin-coat and pattern the photoresist.

(b) Use RIE to etch the lens material for the first step.

(c) Spin-coat and pattern the resist for the second step.

(d) Etch the lens material by RIE.

Figure 1-11: Fabrication process of a four level microlens by the binary method.

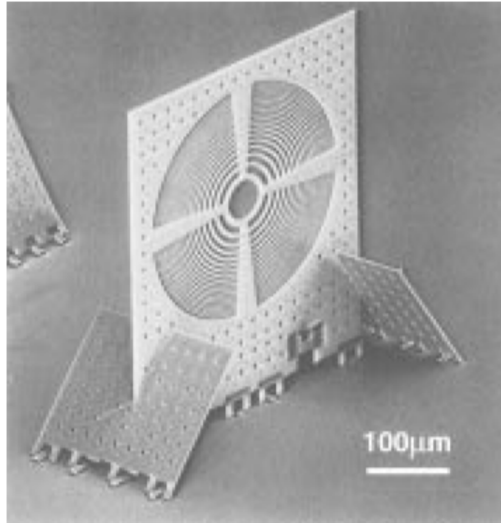

Figure 1-12: SEM micrograph of the out-of-plane micro-Fresnel lens. [8]

1-2-3 Gray Scale Mask

The gray-scale mask technology uses the sub-micrometer resolution and locally modulates the intensity of the ultra-violet (UV) light through the mask to fabricate the microlens. The technology takes one-mask photolithography for a three-dimensional structure, so this process is simpler than the binary method. There are several methods to fabricate the gray-scale mask which are described as follows.

(1) Half-tone Mask

Half-tone mask, as schematically shown in Figure 1-13, uses different square patterns in the mask to cause different gray levels [9]. The basic concept is that the resolution of the photolithography system must be larger than the minimum size of the pattern on the mask so that an averaged gray scale pattern can be formed on the surface of the photoresist. If the resolution of the photolithography system is smaller than the mask pattern, the pattern on the mask will be completely transferred to the photoresist and no gray scale effect can be achieved. Figure 1-13 is the schematic diagram of a three-level gray-scale mask pattern and the resulting photoresist structure, and the actual resist structure is shown in Figure 1-14.

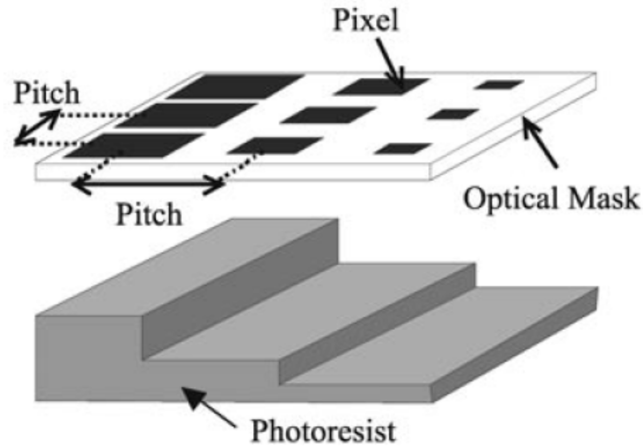

Figure 1-13: Schematic diagram of a three-level gray-scale mask pattern and the resulting photoresist structure. [9]

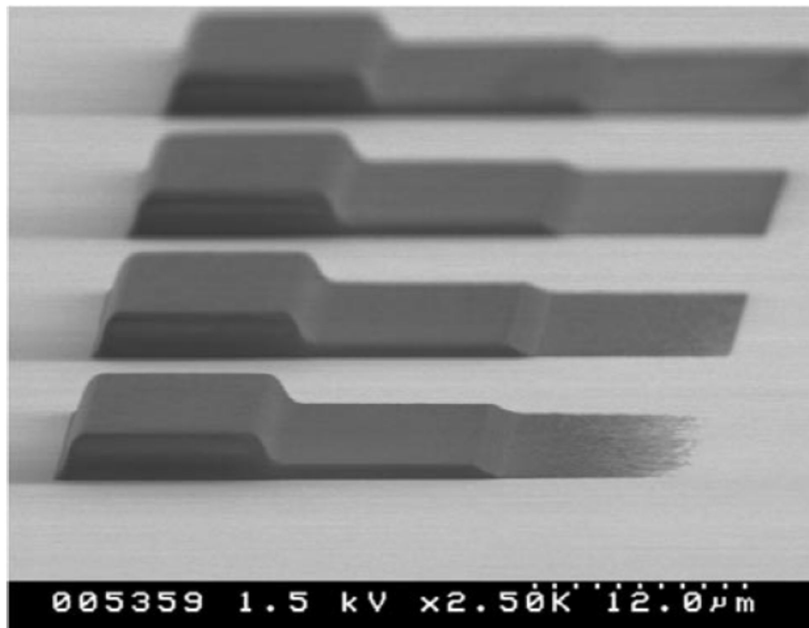

Figure 1-14: SEM micrograph of the three gray levels patterned in AZ4620 photoresist resulting from a similar mask pattern in Figure 1-13. [9]

(2) High-Energy Beam-Sensitive Glass (HEBS)

The HEBS glass used for the gray-scale mask consists of a low-expansion zinc borosilicate glass, i.e., a white-crown glass [10]. The base-glass composition consists of silica, metal oxides, nitrates, halides, and photoinhibitors. Typically, TiO_2, Nb_2O_5,

or Y_2O_3 are used as photoinhibitors to dope the silver-alkali-halide, i.e., $(AgX)_m(MX)_n$, complex crystals. These complex crystals are the HEBS materials, and will be changed by high energy beams, such as electron beams. The HEBS glass has different gray-scale levels with different illuminated energy, and the resolution is much higher due to the electron beam size. Figure 1-15 shows a gray-scale HEBS mask pattern, and Figure 1-16 is the SEM micrograph of the actual structure fabricated in a quartz substrate.

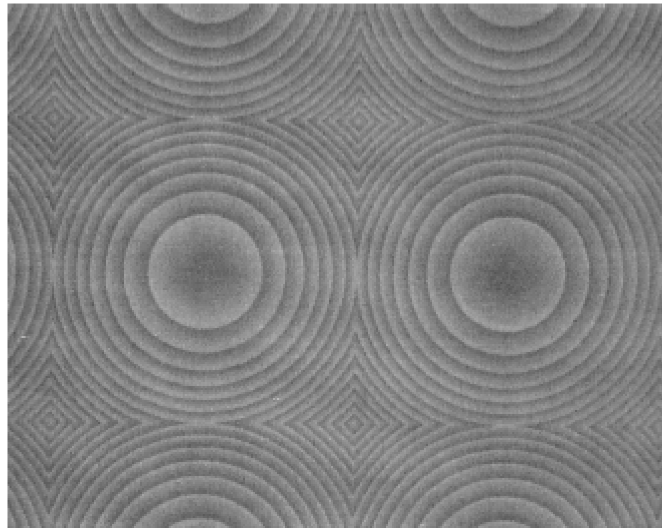

Figure 1-15: Optical micrograph of the gray-scale mask. [10]

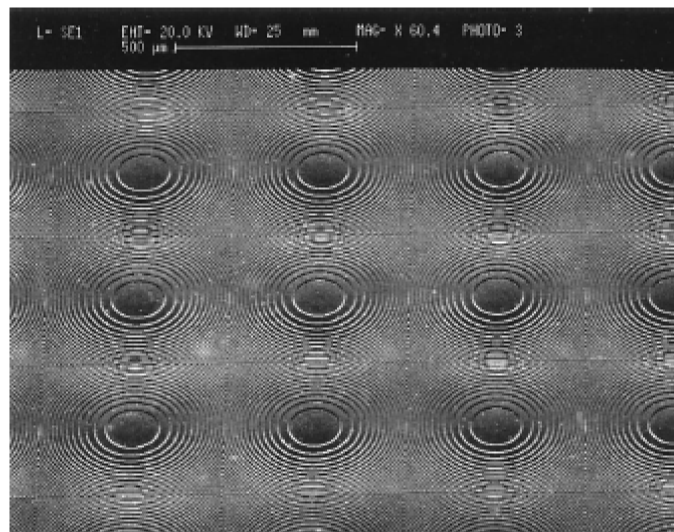

Figure 1-16: SEM of a diffractive optical element in a quartz substrate. [10]

(3) Laser Direct Writing

The laser direct-writing gray-scale masks also have been applied to fabricate diffractive microlenses. Figure 1-17(a) shows the laser-written sixteen-level microlens pattern before the etching process, and Figure 1-17(b) is a microphotograph of the etched microlens [11].

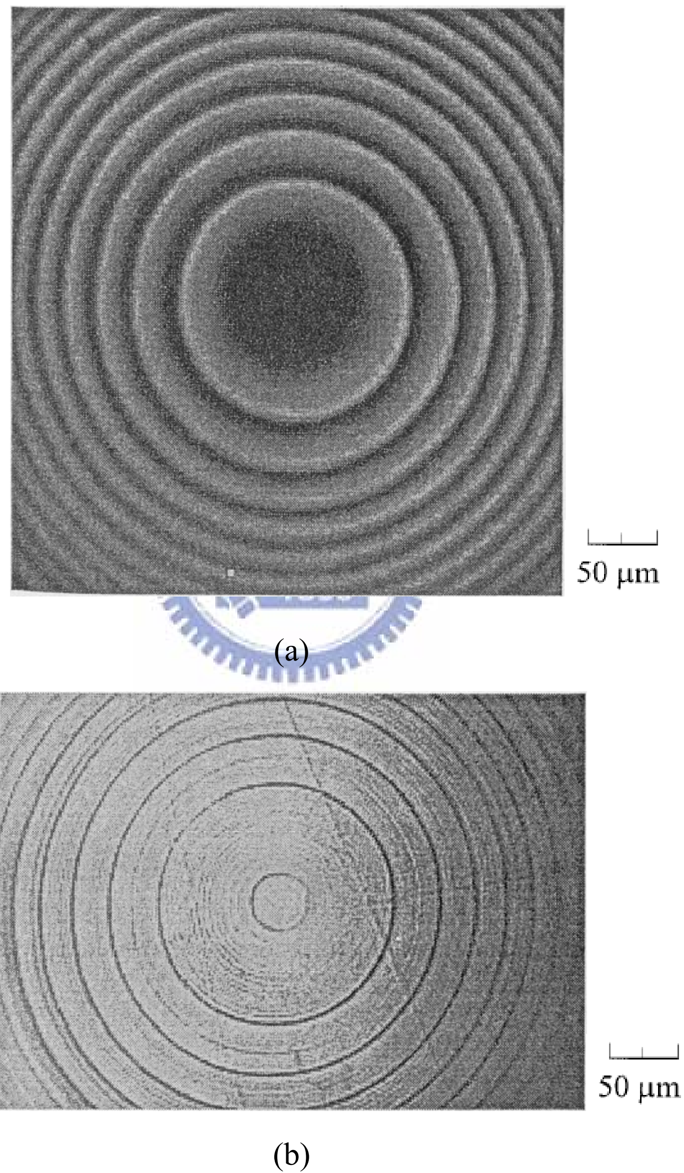

Figure 1-17: (a) A laser direct-writing gray-scale microlens mask and (b) the etched 16-level microlens structure. [11]

(4) Focused Ion Beam (FIB)

Finally, FIB can be used to mill the substrate to fabricate the microlenses. Compared with other conventional techniques, such as laser direct writing and electron-beam direct lithography, it has the advantage of one-step fabrication without any pattern transfer steps. The substrate material selectivity is not required. This method is investigated in this research and the details of the FIB system will be stated as follows.

1-3 Focused Ion Beam System

A focused ion beam system is a mask-less processing equipment used to make a wide variety of small structures in various materials by utilizing sputtering etching or ion beam induced deposition. Since the 1980s, it has been used in photo-mask repair, modification of the wiring of integrated circuits, processing and observation of cross sections of integrated circuits.

The typical FIB instrument consists of a vacuum chamber, a liquid metal ion source (LIMS), an ion column, a sample stage, detectors, gas inlets, and a computer to control the complete system as shown in Figure 1-18 [12]. The capabilities of the FIB for small probe sputtering are made possible by the LMIS, which can provide a source of ions of ~5 nm in diameter. Several metallic elements or alloy sources can be used in a LMIS, and gallium (Ga) is currently the most commonly used material. Once the Ga ions are extracted from the LMIS, they are accelerated through a potential down the ion column. Figure 1-19 is a schematic diagram of the FIB column. The sample stage typically provide 5-axis movement (X, Y, Z, rotation, and tilt), and all five axis stage motions may be motorized for automatic positioning. Typically, the imaging detector of the FIB system is used to collect secondary electrons for image information. Gas delivery systems can be used in conjunction with the ion beam to

produce site specific deposition of metals, such as Platinum (Pt) or Tungsten (W), or insulators or to provide enhanced etching capabilities. All the devices and systems are controlled by a computer.

FIB instruments may be stand-alone single beam instruments. Alternatively, FIB columns have been incorporated into other analytical instruments such as a scanning electron microscope (SEM), Auger electron spectroscopy, transmission electron microscope (TEM), or secondary ion mass spectrometry. The most common one is a FIB/SEM dual-beam instrument, as is used in this research. The electron beam can be used for imaging without concern of sputtering the sample surface, so very creative ion beam milling and characterization can be obtained. In addition, electron beam deposition of materials can be used to produce very low energy deposition that will not affect the underlying surface of interest as dramatically as ion beam assisted deposition. The column arrangement of the dual-beam FIB systems is shown in Figure 1-20.

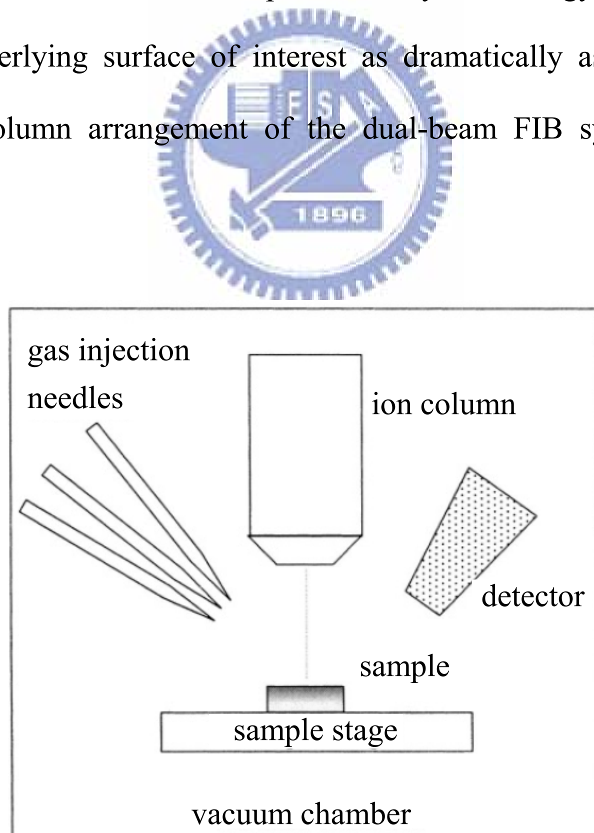

Figure 1-18: Schematic diagram of a basic FIB system. [12]

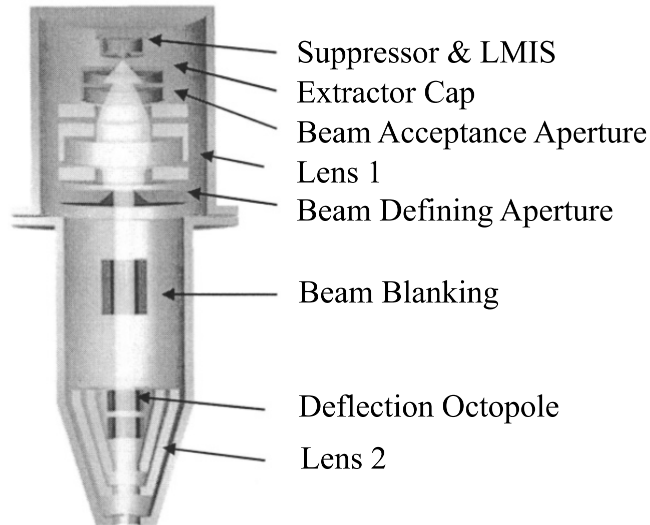

Figure 1-19: Schematic diagram of the basic FIB column. [12]

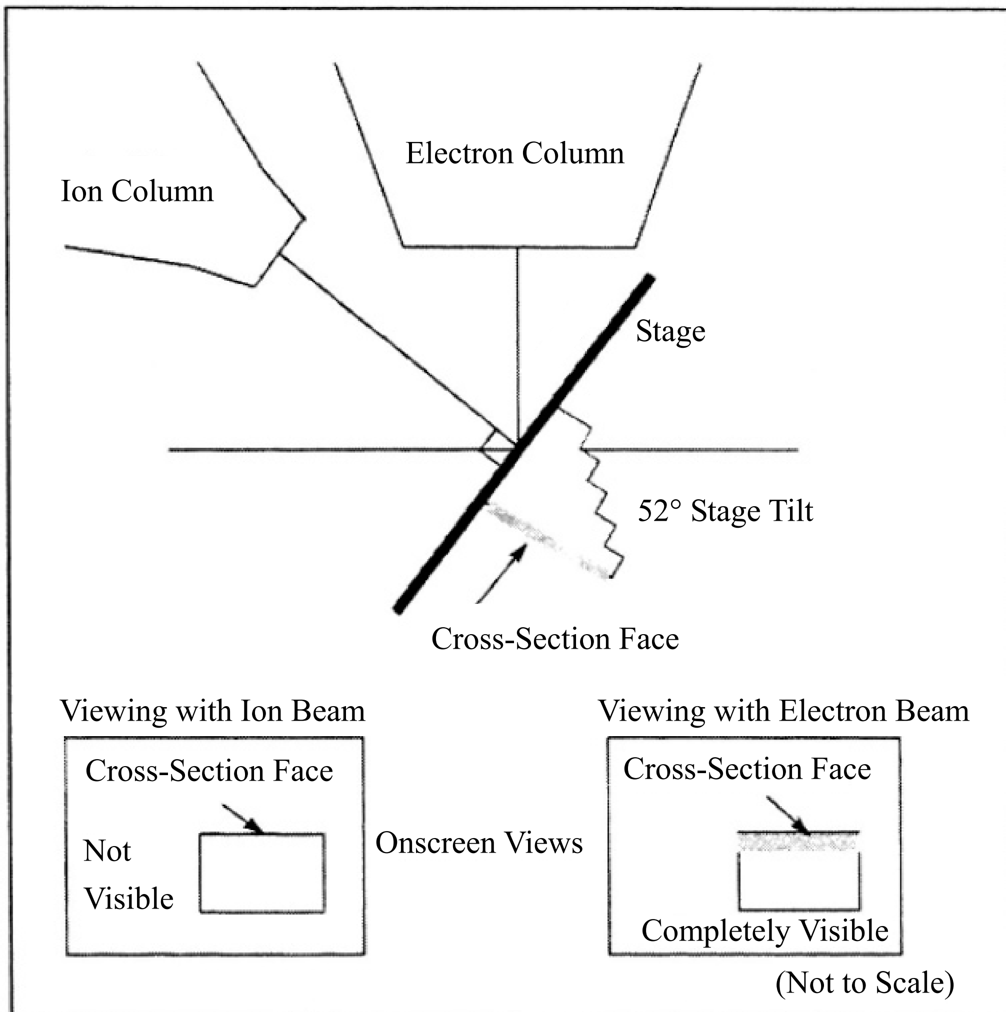

Figure 1-20: Schematic diagram of a dual-beam FIB column arrangement. [12]

FIB systems have been used for the modification or fabrication of prototype optoelectronic and magnetic devices, integrated circuits, the preparation of specimens for material analysis, and the micromachining of MEMS. In addition, FIB milling can be used to fabricate diffractive microlenses. Figures 1-21(a) and 1-21(b) show diffractive lenses with a designed depth of 1.06 μm fabricated on silicon [13]. Also, some interesting thoughts have been demonstrated by using FIB systems, such as a nano wine glass made by carbon deposition or ion beam milling, namely a "nano milling machine" or a "nano lathe" [14]. The SEM micrograph of the nano wine glass produced with the "nano milling machine" is shown in Figure 1-22.

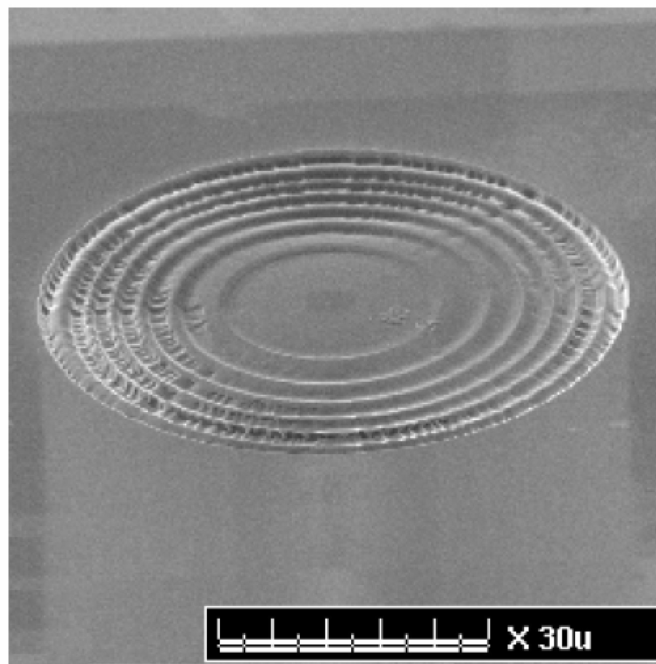

(a)

Figure 1-21: Diffractive lens on silicon by use of FIB milling. It was characterized by the AFM with a tapping mode. (a) 2D profile in the horizontal direction. (b) SEM micrograph of the fabricated device. [13]

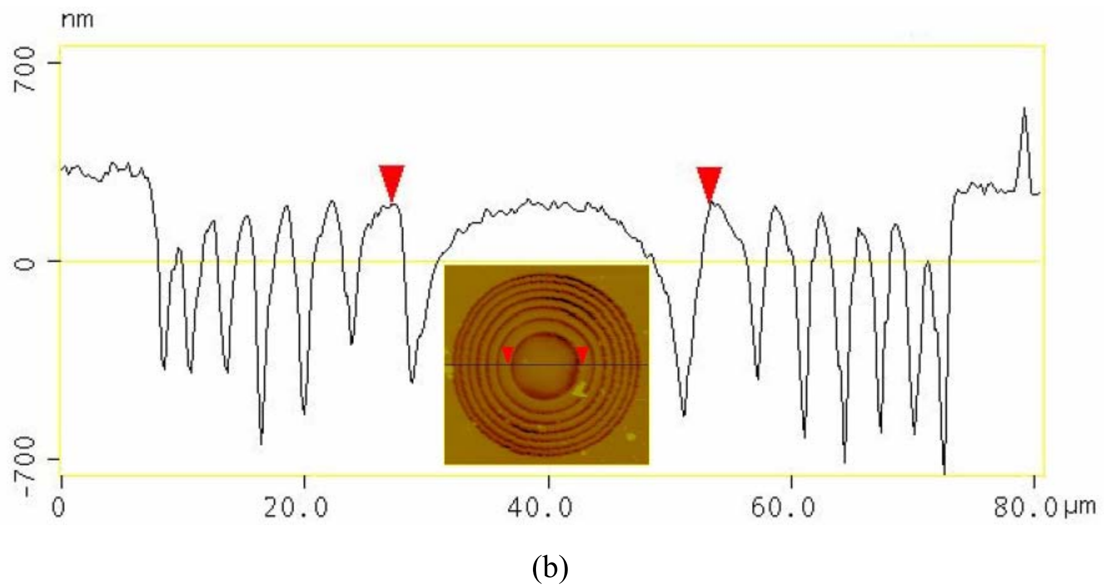

(b)

Figure 1-21: (Continued) Diffractive lens on silicon by use of FIB milling. It was characterized by the AFM with a tapping mode. (a) 2D profile in the horizontal direction. (b) SEM micrograph of the fabricated device. [13]

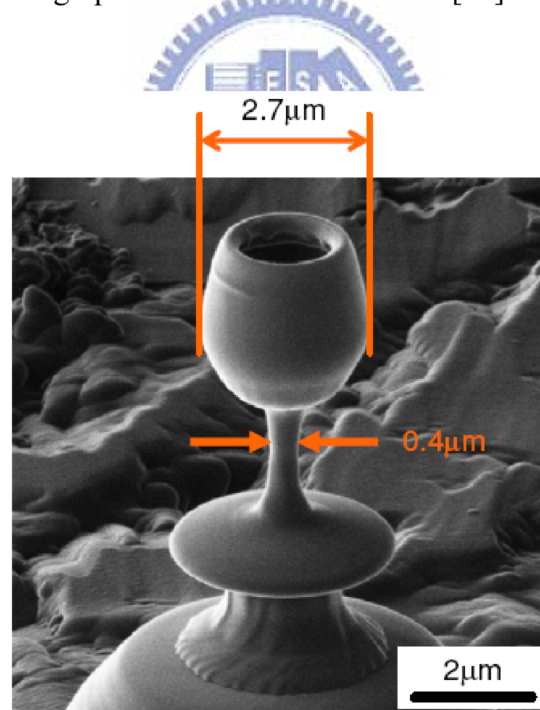

Figure 1-22: SEM micrograph of the nano wine glass made by FIB milling. [14]

In this thesis, the FIB system is used to mill the silicon nitride films on the silicon substrate to produce microlenses. Since silicon nitride has high absorption in the ultraviolet (UV) wavelength used in photolithography, such milled pattern can

also be used as a gray-scale mask. Moreover, the detailed design concepts and fabrication process of the microlenses and gray-scale masks will be discussed in Chapters 2 and 3.

The specifications and functions of the FIB system in the Semiconductor Research Center (SRC) at National Chiao Tung University (NCTU) are listed below [15]:

- xT Nova NanoLab 200 system of FEI company
- Ion source: Ga^+ LMIS
- Acceleration voltage range: 0.5 to 30 kV for electron beam and 5 to 30 kV for ion beam
- Image resolution: 1.5nm for SEM and 7 nm for FIB
- Working distance range: 50 mm
- Data storage
- Process yield engineering
- Etching
- Lithography
- Metal (i.e., Pt and W) and other materials deposition
- Fabrication of micro- and nanostructures

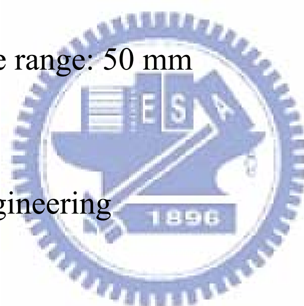

1-4 Objectives and Thesis Overview

There are two major objectives in this thesis:

(a) using the FIB system to directly write the microlens patterns on the silicon nitride film to form the lens.

(b) producing microlenses by using the gray-scale mask on the silicon nitride film fabricated by the FIB system.

The fundamental principles and design concepts of the gray-scale mask and

microlenses are described in Chapter 2. The fabrication processes of the lens and mask are discussed in Chapter 3. Then, the profiles of the FIB pattern measured by AFM and the results of the optical experiments of the lens are described and discussed in Chapter 4. Finally, conclusion and future work of the research are discussed in Chapter 5.

Chapter 2 Principle and Design

In this research, microlenses and gray-scale masks are fabricated. The principle and design are considered in this chapter. Silicon nitride and photoresist AZ4620 are used as the materials of the microlenses and gray-scale masks. Focused ion beam is used to fabricate the lenses and the masks. The Fresnel microlens in silicon nitride is produced by FIB milling, and the microlens in AZ4620 is fabricated through the contact-mode photolithography with the FIB-milled gray-scale mask in silicon nitride. The design of the microlenses and gray-scale masks is based on the material properties and optical characteristics of the photoresists and silicon nitride, and the characteristics of the FIB system.

2-1 Material Properties

2-1-1 Photoresist AZ4620

AZ4620, a positive photoresist, is a macromolecular compound that comprises three basic constituents: a base resin, a photoactive inhibitor, and a solvent. The base resin is a binder to increase the stiffness of the resist through the photo-chemical reaction. The photoactive inhibitor is a material whose photo-chemical properties will be changed by the exposure to the light source. The concentration of inhibitor strongly influences the dissolution rate of the photoresist in a developer solution. The solvent is used to render a mixture of base resin and photoactive inhibitor into a liquid state. This allows for spin coating of the resulting photoresist onto a silicon wafer or another material substrate.

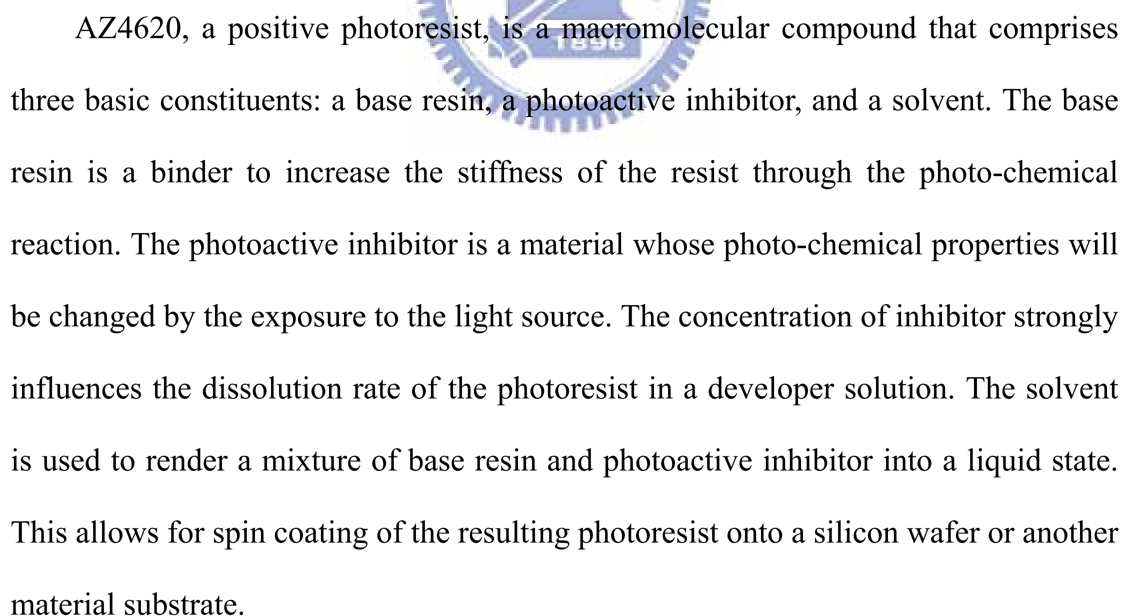

As a result of various factors in the exposure and the development processes, the dissolution rate of exposed photoresist tends to exhibit a nonlinear relation with respect to inhibitor concentration. It is quite difficult to characterize the exposure and the development processes on the molecular level. But various properties of the resist

can be combined into a macroscopic analysis to find a functional relation between the dissolution rate and the mask transmission [16]. In order to develop the model of photoresist, it is assumed that the initial photoresist consists of material *C* and that, on exposure to UV irradiation, is transformed into a second material, named material *S*, without any intermediate materials during the transformation. In the developer solvent, the development rate of material *C* is denoted D_C, and the development rate of material *S*, *Ds*. Thus, $D_S >> D_C$ for the positive photoresist. In the gray-scale process, the resultant photoresist film is composed of both material *C* and material *S*. In the following derivation, the percentage of material *C* is denoted as *C*, and the percentage of material *S* as *S*.

Now consider a positive photoresist which is entirely unexposed initially at $t = 0$:

$$\begin{cases} S_{t=0} = S(0) = 0 \\ C_{t=0} = C(0) = 1 \end{cases}. \tag{2-1}$$

The film is transformed during an exposure interval Δt. It is assumed that the change ΔS is proportional to the amount of unchanged material *C* and to the intensity *I* of UV light, according to

$$\Delta S(t) = \mu C(t) I \Delta t \,. \tag{2-2}$$

The constant μ is the optical response parameter, which describes the material's sensitivity to UV irradiation. The total amount of photoresist is conserved during the process. As the result,

$$C(t) + S(t) = 1 \,. \tag{2-3}$$

Thus, solving Eqs. (2-2) and (2-3) and enforcing the initial condition in Eq. (2-1), one can obtain

$$S(t) = 1 - \exp(-\mu I t) \,. \tag{2-4}$$

In the gray-scale technique, the optical intensity is controlled by the mask, which has a transmittance *T*. The intensity of light that reaches the photoresist is $I=I_oT$, where I_o

is the intensity without the mask. After exposure time t_0 in seconds, the percentage of material *S* is

$$S(t) = 1 - \exp(-\mu I_o T t_0)\,. \tag{2-5}$$

Define a new variable $\kappa = \mu I_o t_0$, and Eq. (2-5) becomes

$$S(t) = 1 - \exp(-\kappa T)\,. \tag{2-6}$$

The depth of the developed photoresist is proportional to the solubility of the final material, which is also proportional to *S*:

$$\text{Solubility} = D_S S + D_C(1 - S) = D_C + (D_S - D_C)S\,. \tag{2-7}$$

From Eq. (2-5), the percentage of chemical change in the resist is not directly linear to the transmittance. The nonlinear relation can be observed clearly in Figure 2-1.

In our research, the positive photoresist AZ4620 is used for the gray-scale photolithography. To find the parameters of AZ4620 for the above model, the resist

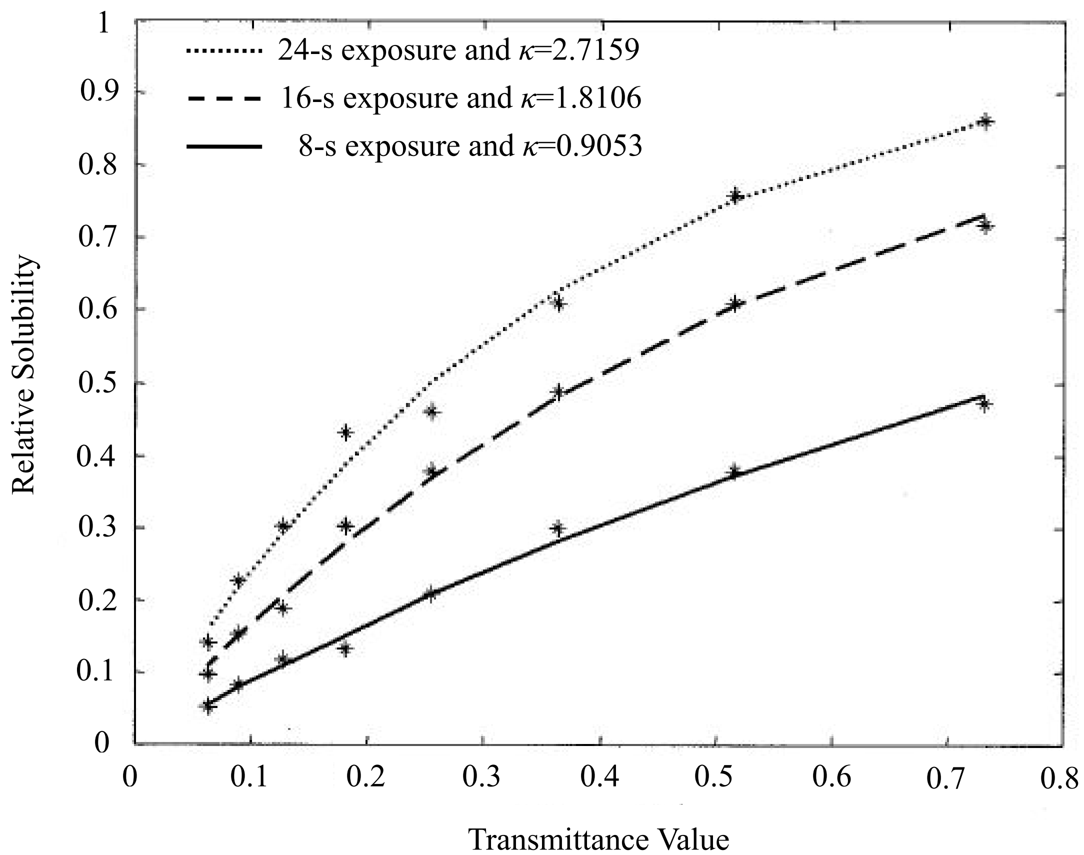

Figure 2-1: Solubility versus the transmittance for the photoresist samples. [16]

was spin coated with the recipe of spread cycle speed = 1000 rpm for 10 seconds and spin cycle speed = 2750 rpm for 35 seconds. After 4-minute soft-bake process, the obtained photoresist thickness was measured as 8 μm. The resist was exposed through a grayscale film mask consisting of regions with transmittance from 0.017 to 0.232. The energy of the UV light of the photolithography system was measured as 10.8 mW without filter and the exposure time was fixed to 90 seconds. Next, the development time was adjusted as 4 minutes to obtain as many gray levels in the photoresist as possible. Then different depths of the developed photoresist were measured for solubility of the resist. Finally, the relative solubility versus transmittance was obtained and shown as Figure 2-2.

In Figure 2-2, the parameters for the linearized model of the photoresist AZ4620 are: the solubility of the material S, $D_S = 0.69\,\mu\text{m}/\text{min}$, the solubility of the material C, $D_C = 0.0003\,\mu\text{m}/\text{min}$, and the optical response parameter, μ=0.015. The relation $D_S >> D_C$ is reasonable for the positive photoresist AZ4620. The model established in

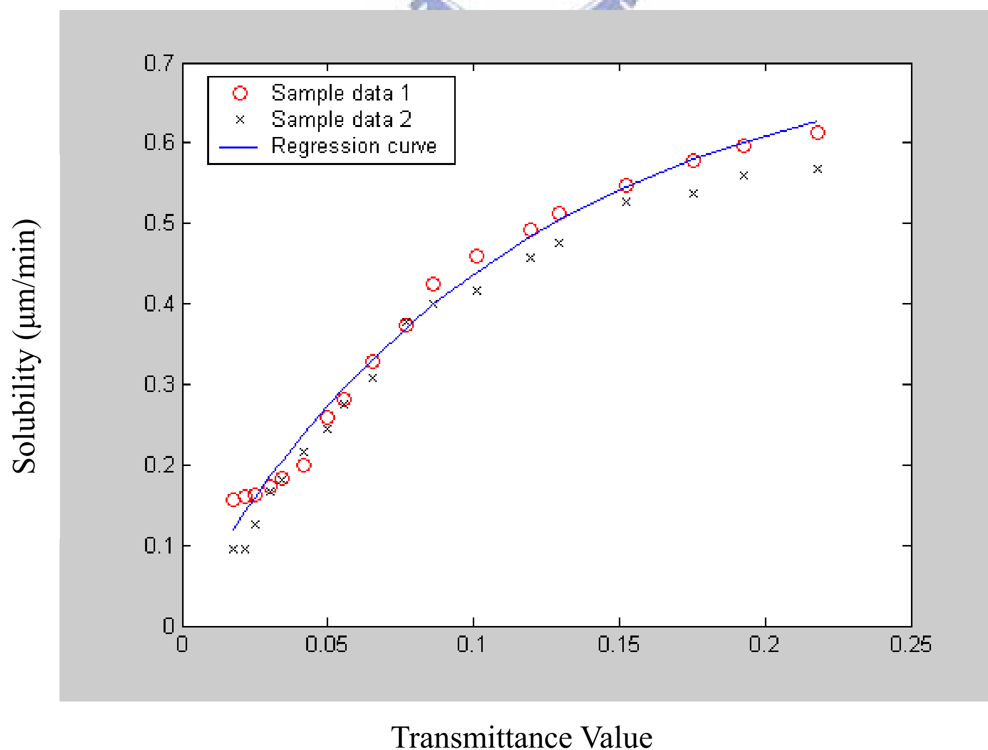

Figure 2-2: Solubility versus the transmittance for AZ4620.

the Figure 2-2 will be used to design the gray-scale masks and Fresnel microlenses in AZ4620 fabricated by the FIB method.

2-1-2 Silicon Nitride

Silicon nitride (Si_xN_y) is a material widely used in microcircuit and microsensor fabrication due to its superior chemical, electrical, optical, and mechanical properties [17]. Si_xN_y is usually used as a hard mask layer or etch stop layer because of the highly selective etch rates over the silicon oxide and silicon nitride in many etching process. Other applications of silicon nitride are optical waveguides (nitride/oxide), insulators, mechanical protection layer, oxidation barrier, and ion implant mask. Silicon nitride is also hard, with a Young's modulus higher than that of Si, and it can be used, for example, as a bearing material in micromotors. In micromachining, silicon nitride serves as an important mechanical membrane material and isolation/buffer layer.

Silicon nitride can be deposited by a wide variety of CVD techniques, such as LPCVD and PECVD. Silicon nitride is often deposited from SiH_4 or other Si containing gases and NH_3 in a reaction such as:

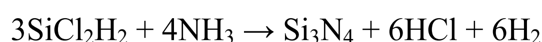

$$3SiCl_2H_2 + 4NH_3 \rightarrow Si_3N_4 + 6HCl + 6H_2$$

The optical properties of the silicon nitride can be controlled by the specifics of the LPCVD process. In the IC industry, silicon nitride is deposited by LPCVD at 700 to 900˚C and at 200 to 500mTorr. In our research, silicon nitride was deposited by LPCVD at 850˚C and 180mTorr in the Semiconductor Research Center (SRC) at National Chiao Tung University (NCTU). The measured refractive index *n* and extinction coefficient *k* by ellipsometry of the LPCVD nitride is shown in Figure 2-3. The absorption of silicon nitride increases sharply in the UV region, so that it can be used as a mask. Moreover, AZ4620 is sensitive to the wavelength 320nm used in the

contact-mode aligner in SRC. Therefore, silicon nitride and AZ4620 are suitable to be the material of the microlens and gray-scale mask.

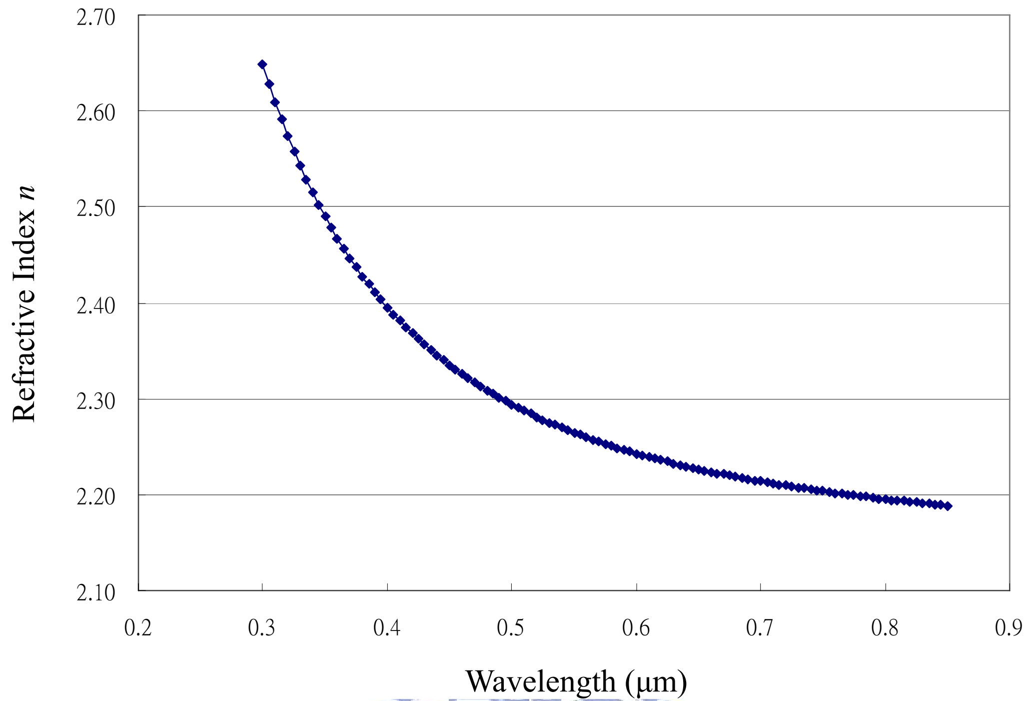

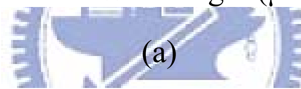

(a)

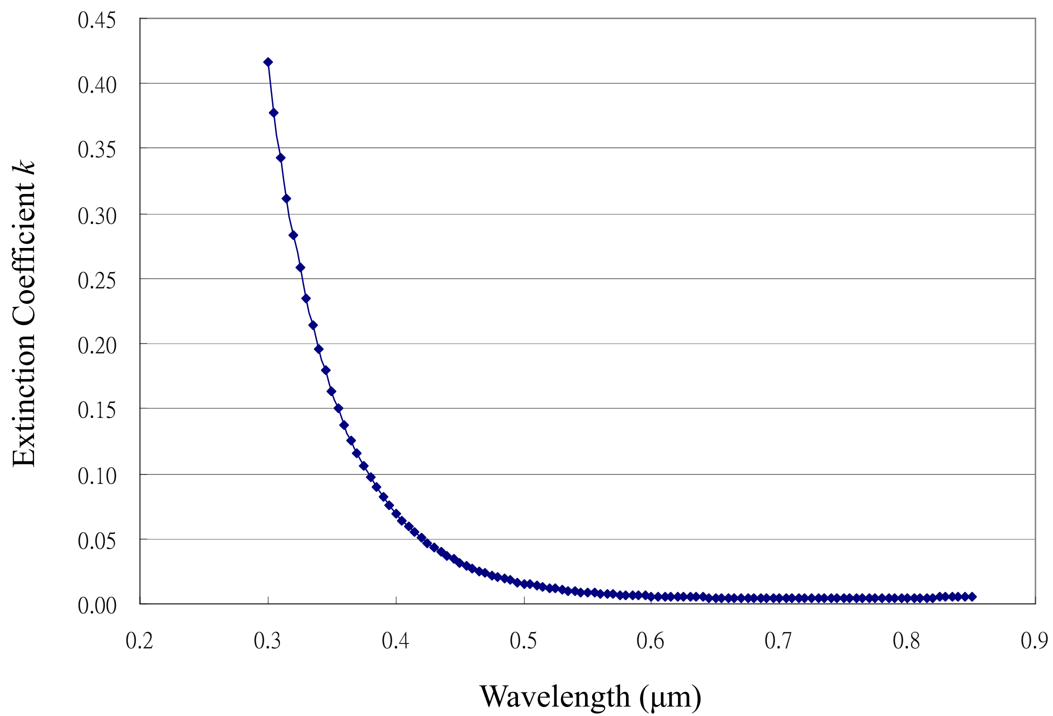

(b)

Figure 2-3: (a) Refractive index and (b) extinction coefficient of LPCVD nitride.

2-2 Fresnel Microlens Design

Fresnel microlens, characterized by its thinness, lightness, high optical efficiency, good focusing and reproducibility, is very attractive in mircooptics, opto-eletro-mechanical, optical communications and optical computing systems. The optical effect of the lens is similar to that of the Fresnel zone plate, but it achieves much higher diffractive efficiency. For the requirement of the DVD micro optical pick-up head, the numerical aperture (N.A.) shown in Figure 2-4 is 0.65.

Based on the definition of the numerical aperture, the focal length of the lens can be decided as:

$$\text{N.A.} = n_{air} \sin\theta = 0.65\,, \tag{2-8}$$

$$\theta = \sin^{-1} 0.65 \approx 40.542^{\circ}\,, \tag{2-9}$$

$$f_o = \frac{R}{\tan\theta}\,, \tag{2-10}$$

where n_{air} is the refractive index of the air, R is the radius of the lens, and f_o is the focal length of the lens. The calculated diameter and focal length of the lens are listed in Table 2-1.

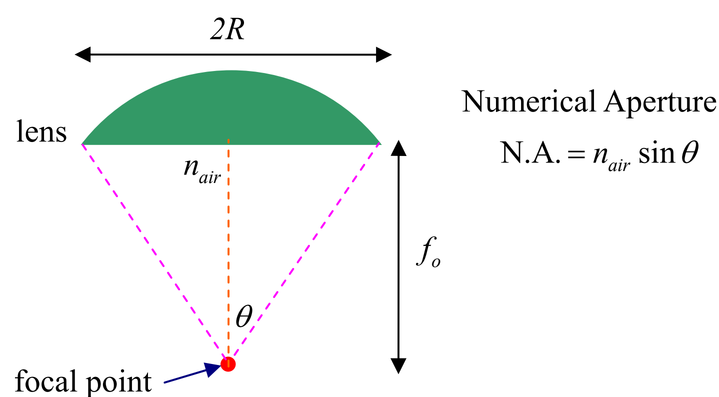

Figure 2-4: Schematic diagram of N.A.

Table 2-1: Focal length calculation.

Diameter ($2R$, μm)	N.A. Value	Focal Length (f_o, μm)
600	0.65	350.74
100	0.65	58.46
50	0.65	29.23
35	0.65	20.46
30	0.65	17.54
20	0.65	11.69

After the focal length and diameter are determined, the microlens can be designed according to Figure 2-5. A parallel light wave changes its direction and focuses on the focal point due to refraction after passing through the lens. In the path of light, different thickness of the lens causes the different phase delay. As Figure 2-5 shows, parallel wavefronts change into approximately spherical wavefronts when passing through the lens. The phase delay from the focal point to flat lens surface can be calculated as

$$\phi(r) = \frac{2\pi d}{\lambda_{air}} = \frac{2\pi}{\lambda_{air}} \cdot \sqrt{r^2 + z^2}\ , \qquad (2\text{-}11)$$

where λ_{air} is the wavelength of the light in the air, d is the distance from focal point to any point on the flat lens surface, and r is the radius in the lens. Based on the assumption that the light passes through the lens straightly, the phase delay from point A on a parallel wavefront to point B on the flat lens surface can be calculated as

$$\Delta\phi(r) = 2\pi \cdot \left(\frac{L_{air}}{\lambda_{air}} + \frac{L_{lens}}{\lambda_{lens}} \right), \qquad (2\text{-}12)$$

where λ_{lens} is the wavelength of the light in the lens material. For silicon nitride as the lens material $\lambda_{lens}=\lambda_{air} n_{lens}^{-1}$ and n_{SiN}=2.23 at wavelength 650 nm; for photoresist AZ4620, n_{AZ4620}=1.6963 at 650 nm.

According to the characteristics of equal phase on the wavefronts, the thickness

$h(r)$ as a function of the lens radius r can be determined by considering the boundary conditions at the center C and edge D of the lens, as shown in Figure 2-5,

$$\phi(r) + \Delta\phi(r) = c\,, \tag{2-13}$$

$$\Rightarrow L_{air} + n_{lens} L_{lens} = -\sqrt{r^2 + z^2} + c_1\,, \tag{2-14}$$

$$\Rightarrow \begin{cases} (C)\ n_{lens} h(0) = -f_o + c_1 \\ (D)\ h(R) = h(0) = -\sqrt{R^2 + f_o^{\,2}} + c_1 \end{cases}, \tag{2-15}$$

$$\Rightarrow c_1 = \frac{n_{lens}\sqrt{R^2 + f_o^{\,2}}}{n_{lens} - 1}\,, \tag{2-16}$$

$$\Rightarrow h(0) = \frac{-f_o + c_1}{n_{lens}} = -\frac{f_o}{n_{lens}} + \frac{\sqrt{R^2 + f_o^{\,2}}}{n_{lens} - 1}\,, \tag{2-17}$$

where c and c_1 are constants, and $h(0)$ is the maximum thickness of the lens. The profile of the microlens can be calculated as

$$h(r) = \left(-\sqrt{r^2 + z^2} + \sqrt{R^2 + f_o^{\,2}} + {f_o}/{n_{lens}}\right) \Big/ \left(n_{lens} - 1\right) \tag{2-18}$$

The diameter and the corresponding maximum thickness of the microlenses made of silicon nitride and AZ4620 are listed in Tables 2-2 and 2-3, respectively. Due to the time restriction of the FIB system in SRC, the diameter of the nitride microlens and AZ4620 microlens must be 20 μm and 35 μm, respectively.

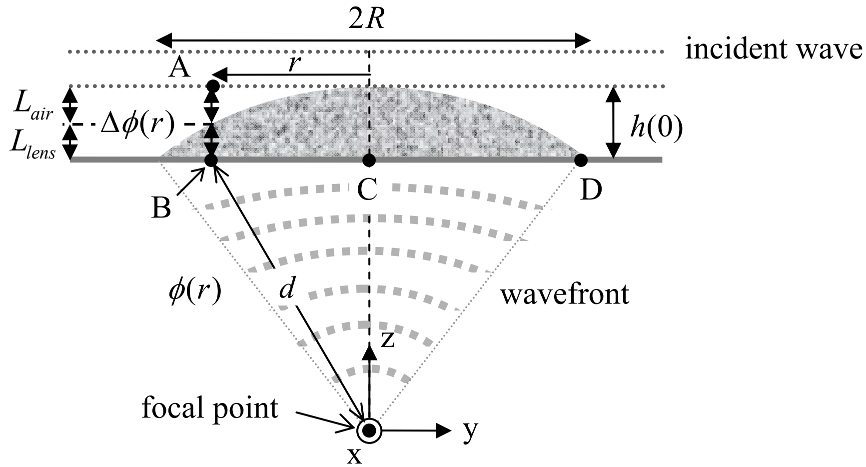

Figure 2-5: Schematic diagram of microlens design.

Table 2-2: Calculated results of the silicon nitride microlens.

Diameter ($2R$, μm)	Focal length (f_o, μm)	Constant (c_1)	Max. thickness ($h(0)$, μm)
100	58.46	91.94	15.01
50	29.23	45.97	7.51
30	17.54	27.58	4.50
20	11.69	18.39	3.00

Table 2-3: Calculated results of the AZ4620 microlens.

Diameter ($2R$, μm)	Focal length (f_o, μm)	Constant (c_1)	Max. thickness ($h(0)$, μm)
100	58.46	103.44	26.52
50	29.23	51.72	13.26
35	20.46	36.21	9.28
20	11.69	20.69	5.30

However, the maximum thickness of the lenses in Tables 2-2 and 2-3 is too large to be deposited by IC processes such as LPCVD. Eq. (2-19) is therefore adopted to slice the microlens, as described in Chapter 1:

$$t = \frac{\lambda}{\left(n_{lens} - 1\right)} \times m, \qquad (2\text{-}19)$$

where t is the sliced thickness, λ is the wavelength of the incident light, n_{lens} is the refractive index of the lens material, and m is an integer. Consider the limited thickness of the LPCVD silicon nitride and m=1, the sliced thickness of silicon nitride and AZ4620, i.e., t_{SiN} and t_{AZ4620}, are 528 nm and 933 nm separately. The calculated results are listed in Tables 2-4 and 2-5, where the minimum thickness is the thickness of the outmost ring, the maximum thickness is the sliced thickness, the minimum line-width is the width of the outmost ring, and the maximum line-width is the radius of the middle circle. The calculated profiles are shown in Figures 2-6 and 2-7

Table 2-4: Calculated results of sliced silicon nitride microlens.

Material	Diameter	Focal length	Max. thickness	Max. line-width	Min. thickness	Min. line-width
Silicon nitride	50 μm	29.23 μm	528.46 nm	12.40 μm	108.37 nm	0.21 μm
	30 μm	17.54 μm	528.46 nm	9.64 μm	276.41 nm	0.53 μm
	20 μm	11.69 μm	528.46 nm	7.90 μm	360.42 nm	0.70 μm

Table 2-5: Calculated results of sliced AZ4620 microlens.

Material	Diameter	Focal length	Max. thickness	Max. line-width	Min. thickness	Min. line-width
AZ4620	50 μm	29.23 μm	933.51 nm	12.40 μm	191.44 nm	0.21 μm
	35 μm	20.46 μm	933.51 nm	10.40 μm	880.81 nm	0.96 μm
	30 μm	17.54 μm	933.51 nm	9.64 μm	488.27 nm	0.53 μm

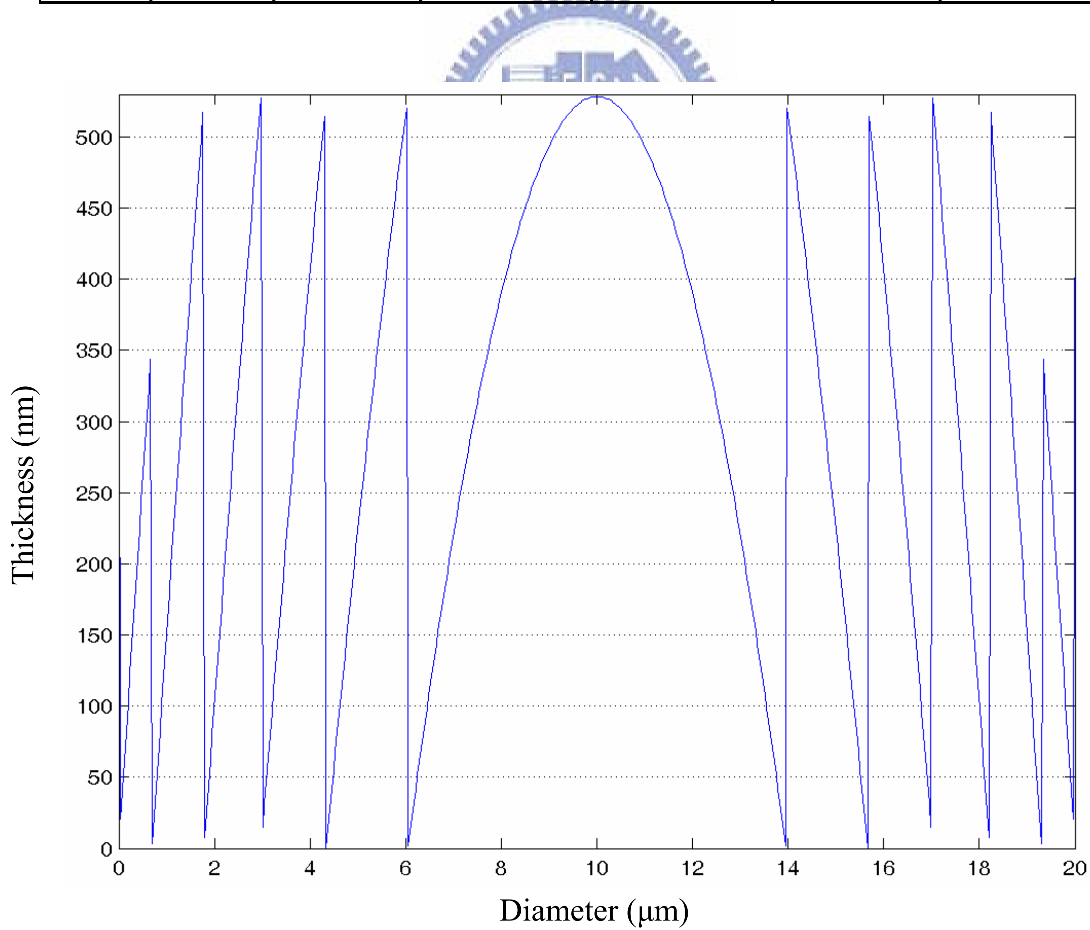

Figure 2-6: Profile of the silicon nitride microlens.

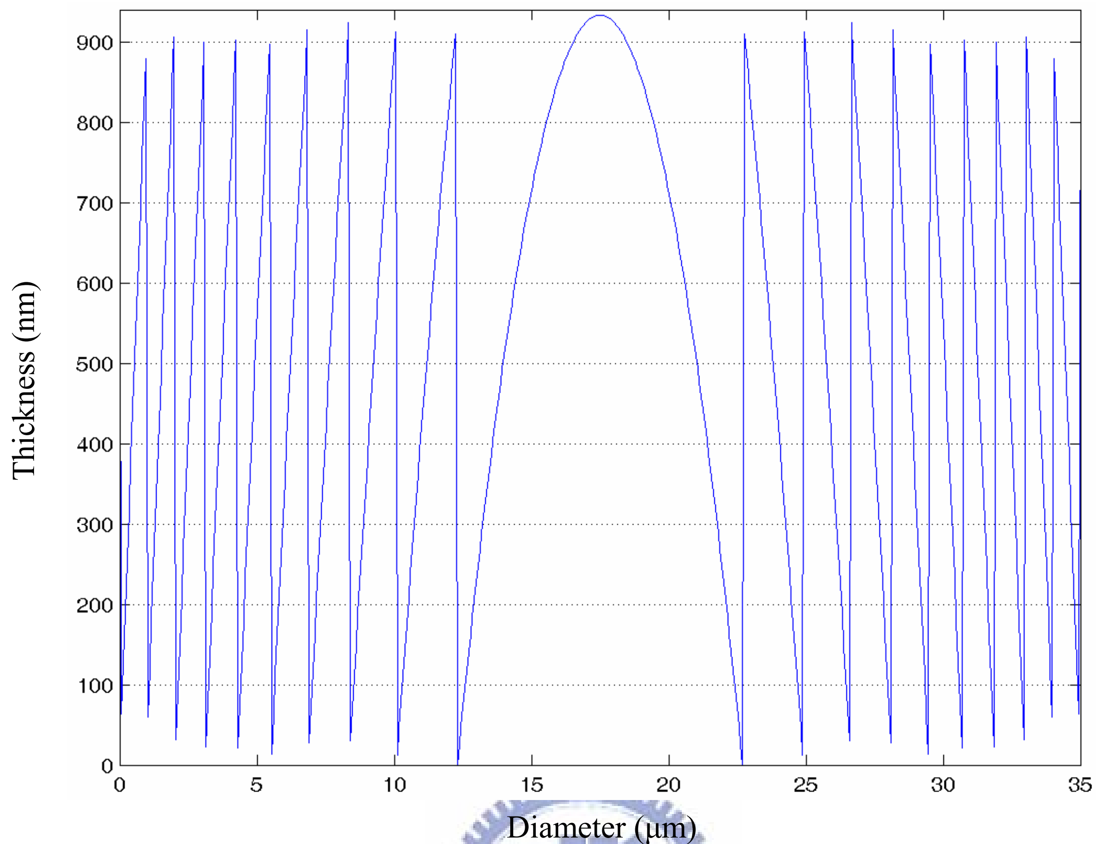

Figure 2-7: Profile of the AZ4620 microlens.

2-3 FIB Pattern Design

The development and functions of the FIB system was discussed in Chapter 1. The milling process is used to fabricate the microlens and gray-scale mask. The dual-beam FIB system (FEI series) in SRC can directly write the lens pattern on the silicon nitride membrane by using a stream file or a bitmap file, the latter of which is used in this research. Besides, the microlens can also be produced by the contact-mode photolithography through the gray-scale mask fabricated in silicon nitride by the FIB system.

2-3-1 Fresnel Microlens Pattern

According to the microlens design and characteristics of the FIB system, the microlens pattern for FIB can be determined. First, the pixel number of the bitmap file must be as large as possible for a good approximation. However, the FIB system has a

constraint on the maximum number of pixels, i.e. the range in x is 0~4095 and in y is approximately 280~3816. Consider the suitable number for approximation and enough space for adding blank pixels, the number of pixels was chosen as 512×512. Then the gray-scale pattern was sampled by the 512×512-pixel matrix and transferred to the 3-D profile by the FIB system. Each pixel in the matrix has three bytes with same values for the gray-scale pattern. Therefore, there are 256 gray levels in the design. The gray-scale pattern of the 20 μm-diameter silicon nitride microlens is shown in Figure 2-8.

2-3-2 Gray Scale Mask Pattern

Based on the photoresist model as discussed above and the transmittance of the silicon nitride membrane, the depth of the gray-scale mask pattern in the silicon nitride films can be determined. Figure 2-9 is a diagram which describes how the gray-scale pattern is transferred to the positive photoresist AZ4620. When the light

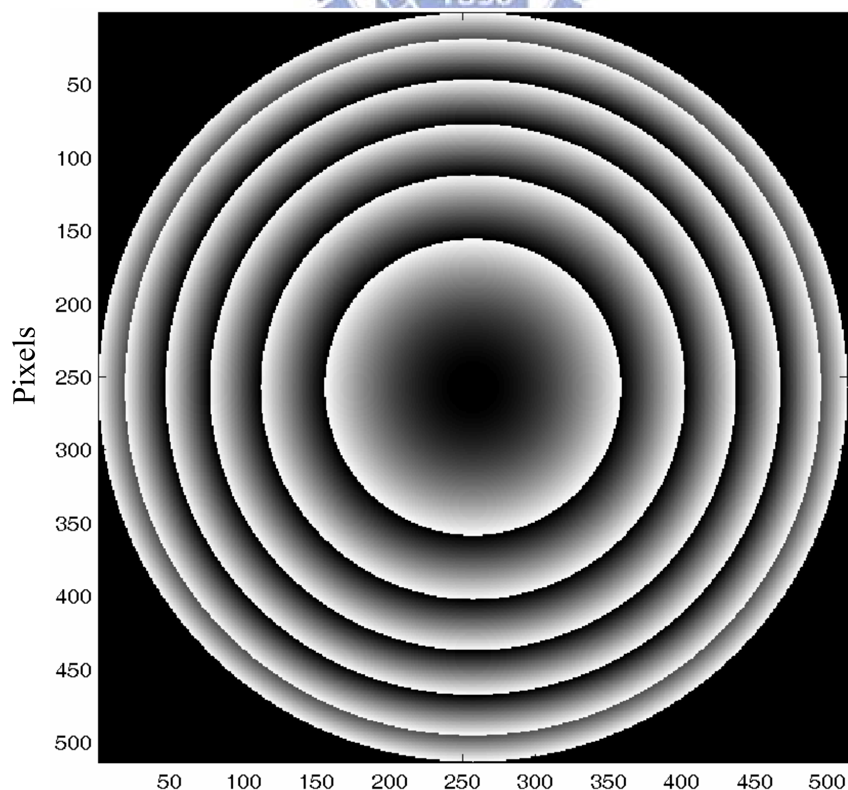

Figure 2-8: Gray-scale pattern of the silicon nitride microlens in 512×512 pixels.

passes through the silicon nitride membrane, the intensity of the light is attenuated in an exponential form, as shown in

$$I = I_o e^{-\alpha x} \propto |E|^2 = |E_o|^2 e^{-\frac{4\pi k}{\lambda_{exp}} x} , \qquad (2\text{-}20)$$

where I is the intensity of the light passing through the membrane, I_o is the incident intensity, E is the electric field of the light passing through the membrane, E_o is the electric field of the incident light, k is the extinction coefficient (0.283) of the nitride film at the wavelength of 320 nm, λ_{exp} is the wavelength (320nm) of the mask aligner in SRC, and x is the thickness of the membrane.

Transmittance can be controlled by the thickness of the nitride membrane, so different thickness causes the difference of the transmitted light intensity, as shown in

$$\frac{I_2}{I_1} \propto |E|^2 = e^{-\frac{4\pi k}{\lambda_{exp}} x} = \frac{0.03}{0.2} = 0.15 , \qquad (2\text{-}21)$$

where I_1 and I_2 are the intensity after passing through different nitride thickness as shown in Figure 2-9. According to the photoresist AZ4620 model in Figure 2-2, there is a transition region of solubility, which is used in the gray-scale photolithography, for the transmittance value between 0.2 and 0.03. From Eq. (2-21), the maximum thickness of the 3-D profile of the gray-scale mask can be determined in

$$x = \frac{\ln(0.15) \times \lambda_{exp}}{-4\pi k} \approx 170.7nm . \qquad (2\text{-}22)$$

According to the AZ4620 microlens design and characteristics of the FIB system, the gray-scale mask pattern can be determined. The gray-scale mask pattern for the 35 μm-diameter AZ4620 microlens is shown in Figure 2-10, and the number of pixels is 512×512.

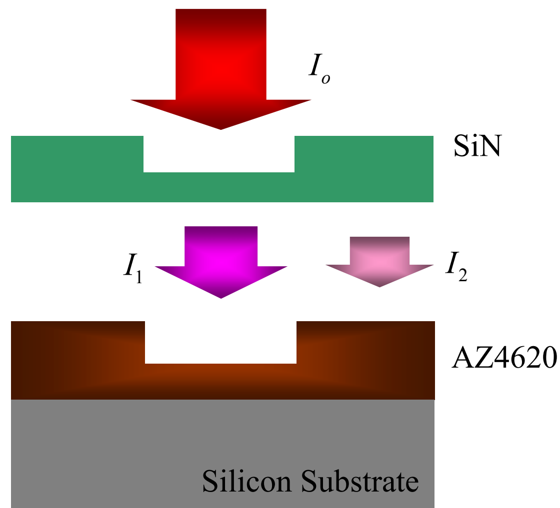

Figure 2-9: Gray-scale pattern transfer.

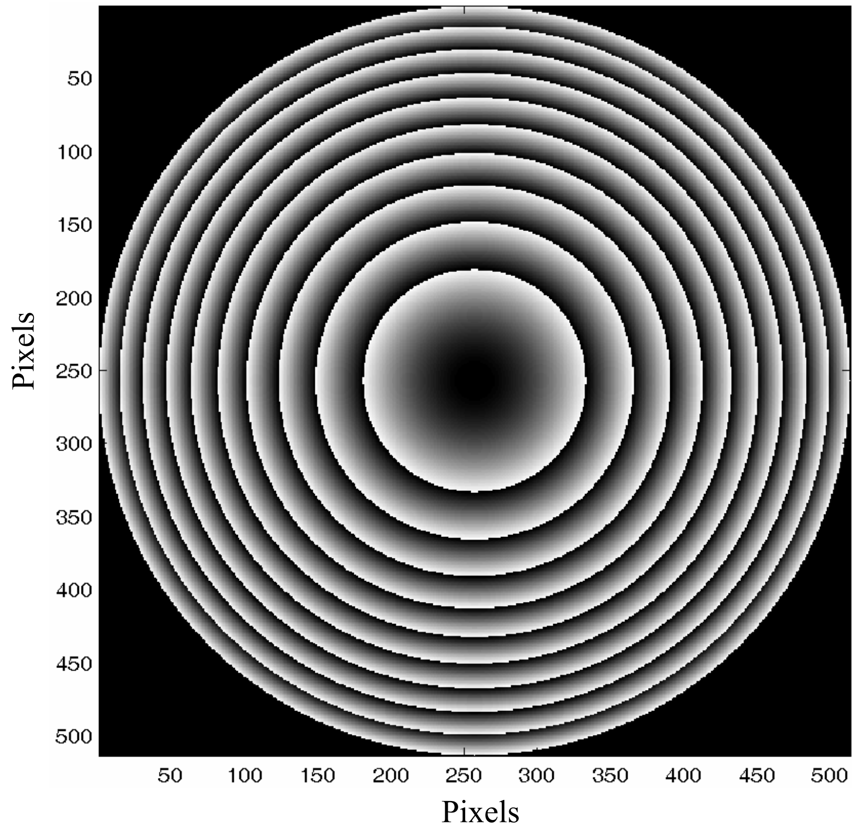

Figure 2-10: Gray-scale mask pattern for the AZ4620 microlens in 512×512 pixels.

2-4 Summary

In this research, silicon nitride and a positive photoresist AZ4620 are used as the lens material, and silicon nitride is also the material of the gray-scale mask. The

Fresnel micolenses with N.A. of 0.65 in silicon nitride and AZ4620 are designed. However, due to the time restriction of the FIB system in SRC, the diameter of the microlens in silicon nitride and AZ4620 must be designed as 20 μm and 35 μm, respectively. The thickness of the microlens in silicon nitride and AZ4620 is designed as 528 nm and 933 nm, respectively. In addition, the gray-scale mask in silicon nitride is also determined. According to the photoresist model of AZ4620 and the optical characteristics of the silicon nitride, the thickness of the mask is designed as about 170 nm. Herein, thickness means the maximum FIB-milled depth. The detailed fabrication processes will be discussed in Chapter 3.

Chapter 3 Fabrication Process

The microlens and gray-scale mask on the silicon substrate can be fabricated by IC processing steps. The patterns of the lens and mask have been determined in Chapter 2. The fabrication processes are discussed in this chapter.

3-1 FIB Milling of Silicon Nitride

In this research, FIB-milled Fresnel microlenses and gray-scale masks were fabricated in the silicon nitride film on the silicon substrate. The schematic diagram of the fabrication process is shown in Figure 3-1, and the details of the process are described as follows. A (100)-orientated bare silicon wafer was used for the substrate. After RCA clean, 1 μm-thick silicon nitride (Si_3N_4) was deposited on the silicon substrate by LPCVD (Figure 3-1(a)). A positive photoresist layer of FH6400 spin-coated on the backside of the wafer was used as the etching mask for the subsequent silicon nitride RIE (Reactive Ion Etching) process (Figure 3-1(b)). After the RIE process, the etching window for bulk-micromachining was opened. The silicon substrate was removed by the KOH etching process so that the light can pass through the nitride film (Figure 3-1(c)). A 80°C 45% KOH solution was used to etch off 500 μm-thick silicon for 10 hours. After KOH etching, the angle between the final etch-stop plane and the (100) plane was almost 55°, as shown in Figure 3-2. Finally, the microlens and gray-scale mask were patterned in the silicon nitride film by FIB-milling (Figure 3-1(d)).

In order to avoid the charge accumulation on the silicon nitride membrane, gold (Au) or platinum (Pt) is sputtered on both sides of the specimen before the FIB process. The FIB parameters, i.e., dwell time, passes, and Z-size, were tuned to get smooth profiles and enough depth of the desired pattern. After the FIB patterning, the silicon nitride microlens and gray-scale mask were complete. The SEM micrographs

of the microlens or the gray-scale mask was shown in Figure 3-3(a) and Figure 3-3(b), respectively.

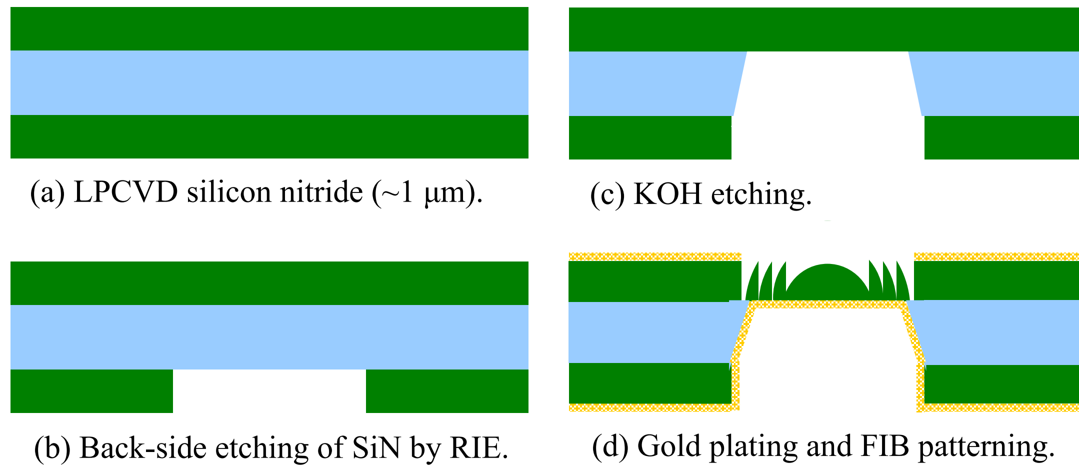

Figure 3-1: Schematic diagram of the fabrication process.

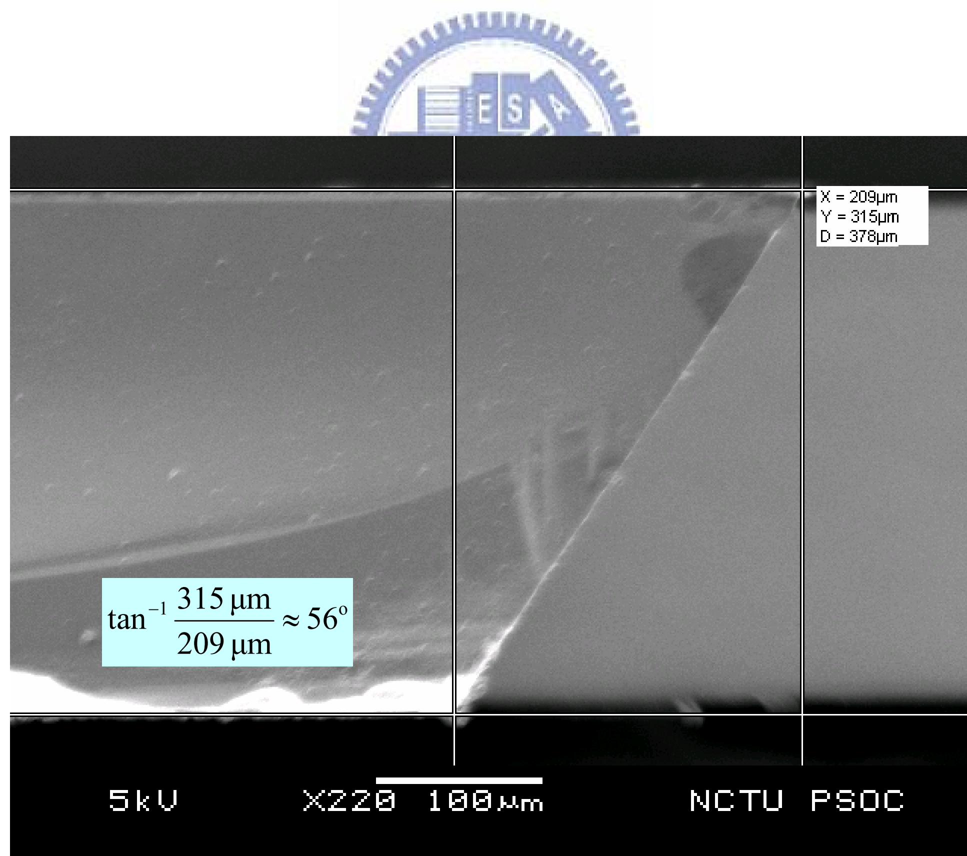

Figure 3-2: SEM micrograph of the KOH etching process.

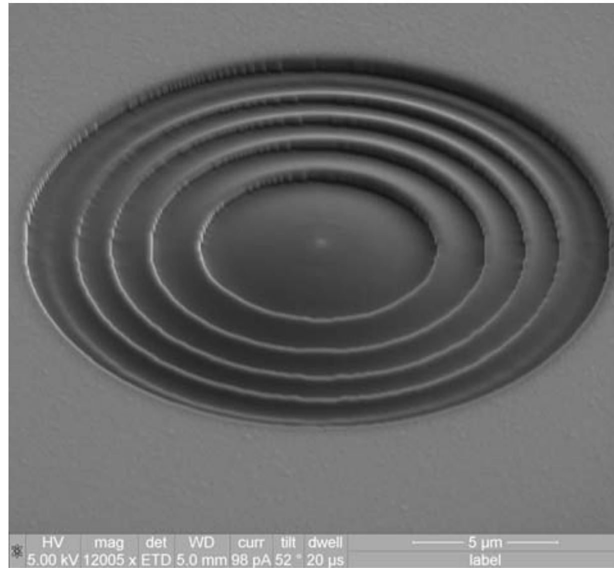

(a)

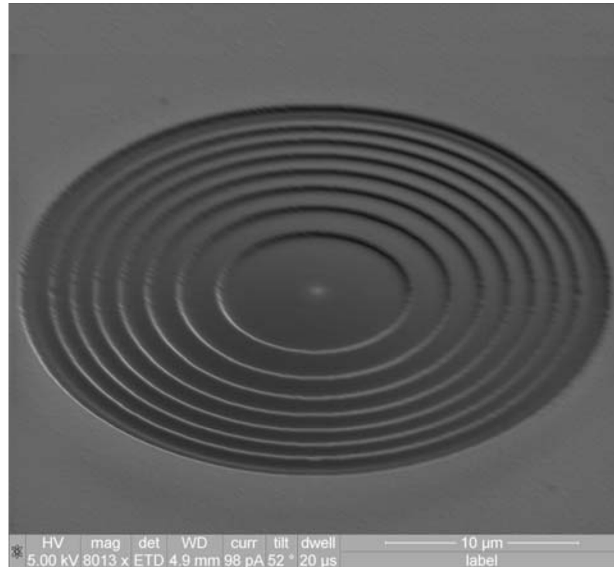

(b)

Figure 3-3: SEM micrograph of the (a) microlens and (b) gray-scale mask.

3-2 Microlens in Photoresist

The microlens can be directly patterned in the silicon nitride film by the FIB system. Alternatively, the microlens can be produced in photoresist by photolithography. The FIB system was used to define the gray-scale pattern of the gray-scale mask on the Si_3N_4 film without silicon substrate under it. The AZ4620 microlens was produced through the contact-mode exposure process as shown in

Figure 3-4. From the parameters of photolithography for the photoresist model mentioned in Chapter 2, the photoresist AZ4620 was spin coated with the recipe of spread cycle speed = 1000 rpm for 10 seconds and spin cycle speed = 2750 rpm for 35 seconds. After 4-minute soft-bake process, the resist was exposed through the FIB-milled gray-scale mask and the exposure time was fixed to 10 minutes. The development time was adjusted to 4 minutes to obtain the microlens in the photoresist. Figure 3-5 shows the optical micrograph of a Fresnel microlens in AZ4620 of diameter 35 μm. As the figure shows, the pattern of the microlens is roughly transferred into the AZ4620 layer by photolithography using the gray-scale mask. However, the outer rings in the lens ars not fully developed. So the parameters of photolithography should be adjusted to get a better lens profile.

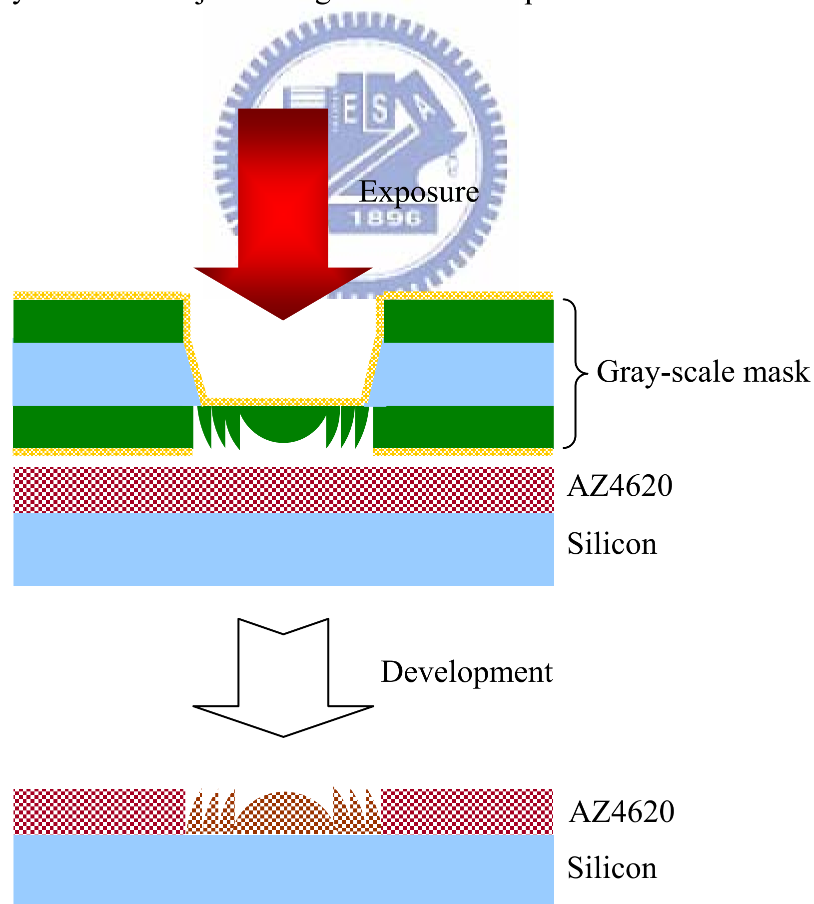

Figure 3-4: Schematic diagram of the exposure process.

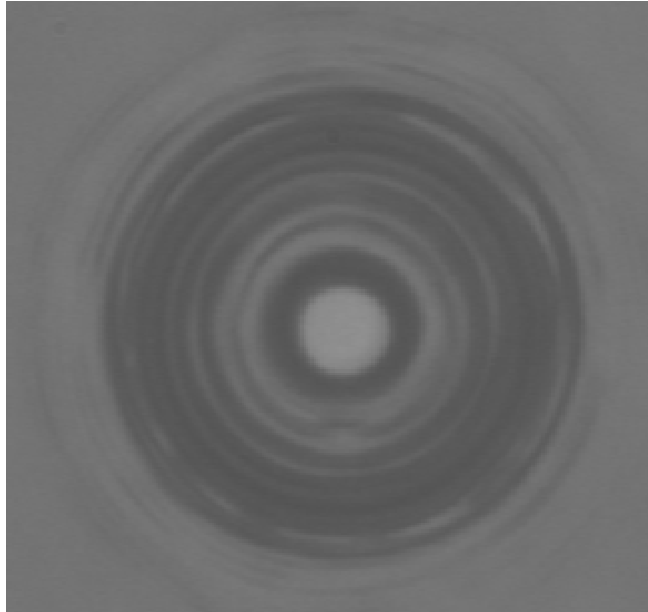

Figure 3-5: Optical micrograph of the microlens in AZ4620 of diameter 35 μm.

3-3 Summary

The fabrication processes of the microlens in silicon nitride and AZ4620 are proposed. Microlenses and gray-scale masks in silicon nitride films have been fabricated. Although the fabrication processes are simple, several issues must be considered, such as the charge accumulation on the silicon nitride membrane and fragility of the samples. In addition, microlenses in AZ4620 through the contact-mode exposure process have been investigated. The measurement results of the FIB-milled patterns will be discussed in Chapter 4.

Chapter 4 Measurement and Experiment

After FIB milling, atomic force microscopy (AFM) was used to examine the 3D profile and depth of the FIB-milled pattern. Optical experiments were used to measure the characteristics of the microlens. The results of the measurements and experiments are presented in this chapter.

4-1 Test Pattern Measurement

Test patterns for the FIB milling were designed to characterize the milled spot size, and the pixel number of the test pattern was 512×512. The FIB parameters, such as step size of each pixel, dwell time, passes, and Z-size, etc., were varied to reveal the characteristics of the milled spot. Herein, the step size means the distance between non-blank pixels in the bitmap figure. Dwell time is the time for which the ion beam stays on a pixel. Passes is the number of times the 24-bit bitmap file is scanned by the ion beam on the sample surface. Z-size is the expected depth of the pattern. The Z-size will be increased as dwell time or passes increases. In addition, the magnification and beam current of the FIB system determine the actual distance between pixels and the actual depth of each pixel. Herein, magnification is the ratio of the viewing area on the monitor screen to the scanned area on the sample. The SEM micrograph of the test pattern in the conditions of magnification as 480x and beam current as 0.3 nA is shown in Figure 4-1. Figure 4-2 shows the AFM measurement results of the FIB-milled test pattern. The profile of the ion-milled spot is shown in Figure 4-3.

Several relations between the measured results, such as “spot size”, “depth”, and “distance”, etc., are discussed below. Herein, as Figure 4-3 shows, “spot size” means the diameter of the ion-milled spot, “depth” means the maximum depth of the spot profile, and “distance” means the actual distance between spots. The relation between

the beam current and “spot size” is shown in Figure 4-4. The milled spot size increases as the beam current or dwell time increases, as shown in the figure. The relation between the step size and “distance” is shown in Figure 4-5. The slope of the curves (a) and (b) in the figure is about 65 nm/step and 26 nm/step, respectively. As the figure shows, the actual distance correlates closely with the magnification and is independent of the beam current. When the magnification increases, the actual distance decreases concurrently. The relation between the dwell time and “depth” is shown in Figure 4-6. The ion-milled depth increases for either increased dwell time or beam current. Also, the milled depth is related to the magnification. In the conditions of the larger magnification and smaller step size, the actual distance will be smaller than the ion-milled spot size. Therefore, a larger depth will be induced by the overlap of the ion-milled spots. The relation between the step size and “depth” is shown in Figure 4-7. According to the trend of the curves, the sudden increase of the depth at small step size is caused by the overlap. From the discussion about the spot profile and overlap conditions, the gray-scale profile can be designed for the FIB process.

In summary, the characteristics of the FIB-milled spots were obtained through the test patterns. In order to achieve the desired depth and retain the better shape of the ion spot, the maximum dwell time and ion beam current of the FIB system are chosen as 1 msec and 0.5 nA, respectively. To avoid the overlap, blank pixels can be inserted into the bitmap, as will be considered as follows.

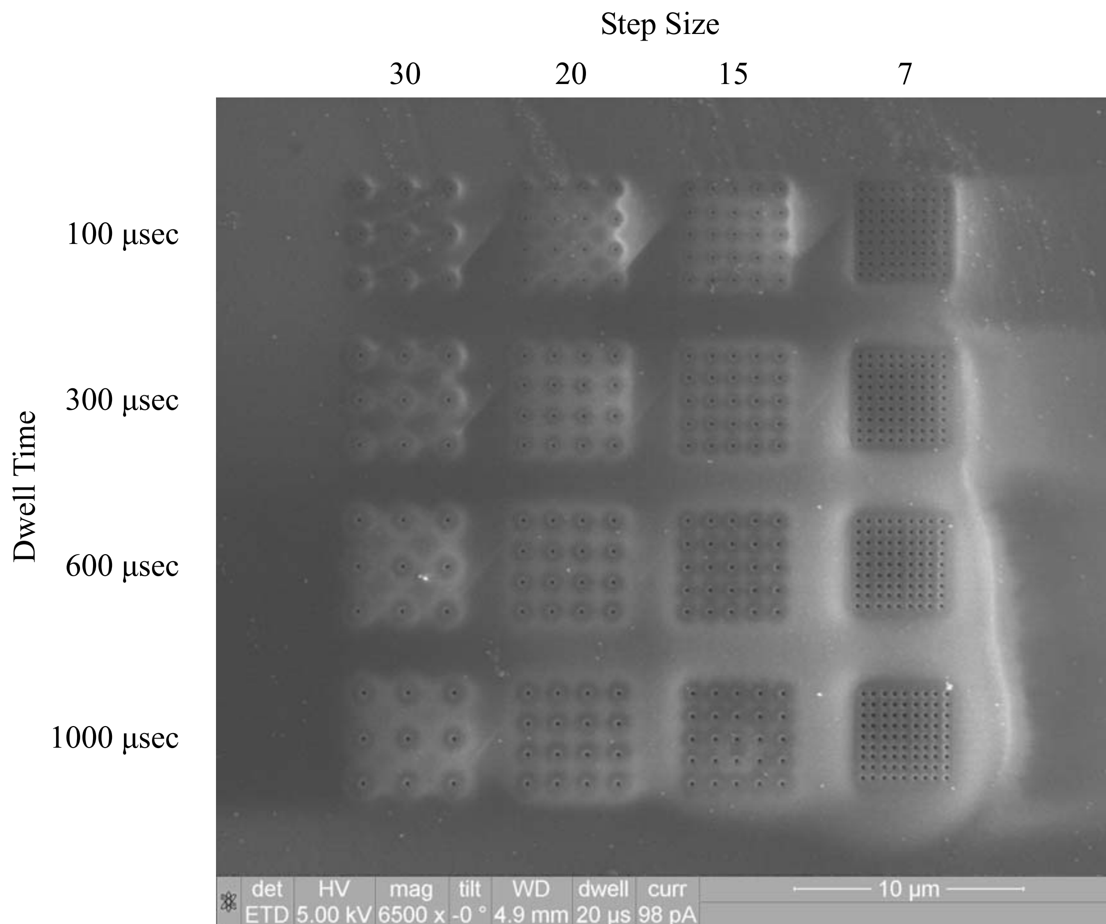

Figure 4-1: SEM micrograph of the test pattern. (Conditions: 480x and 0.3 nA)

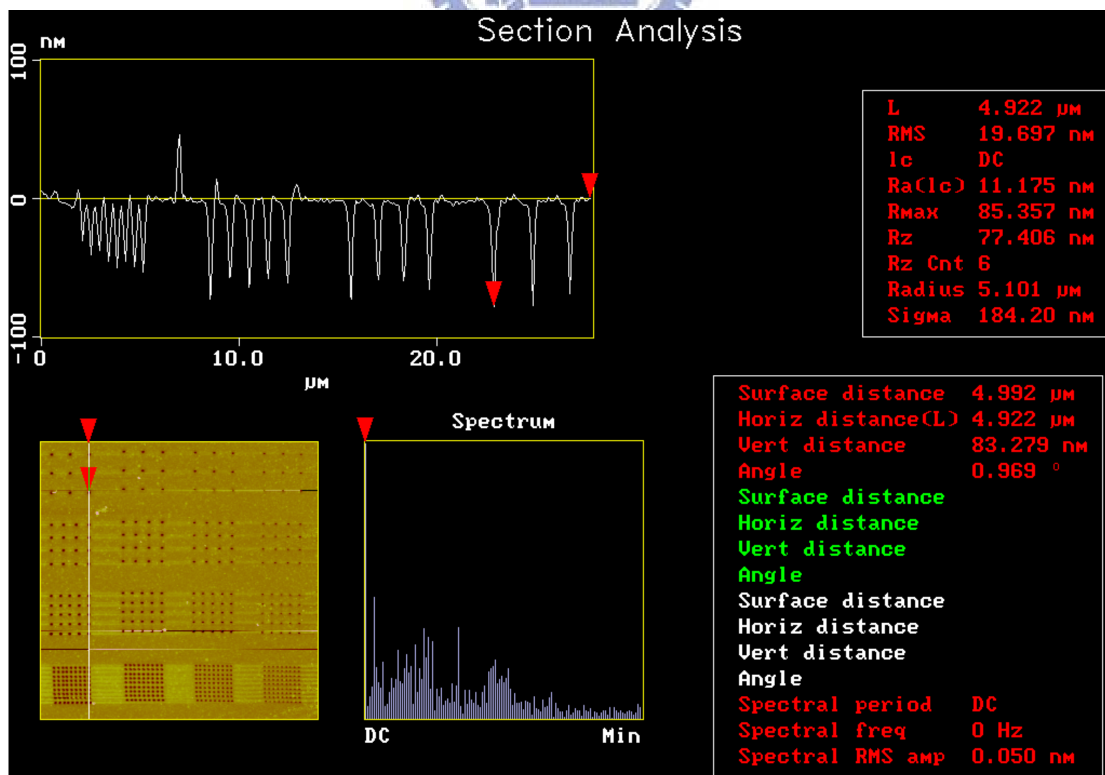

Figure 4-2: AFM profile result of the test pattern.

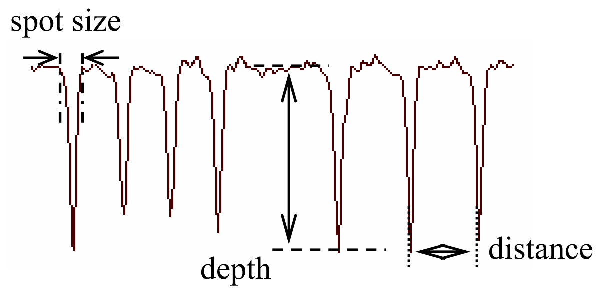

Figure 4-3: Diagram of the spot profile.

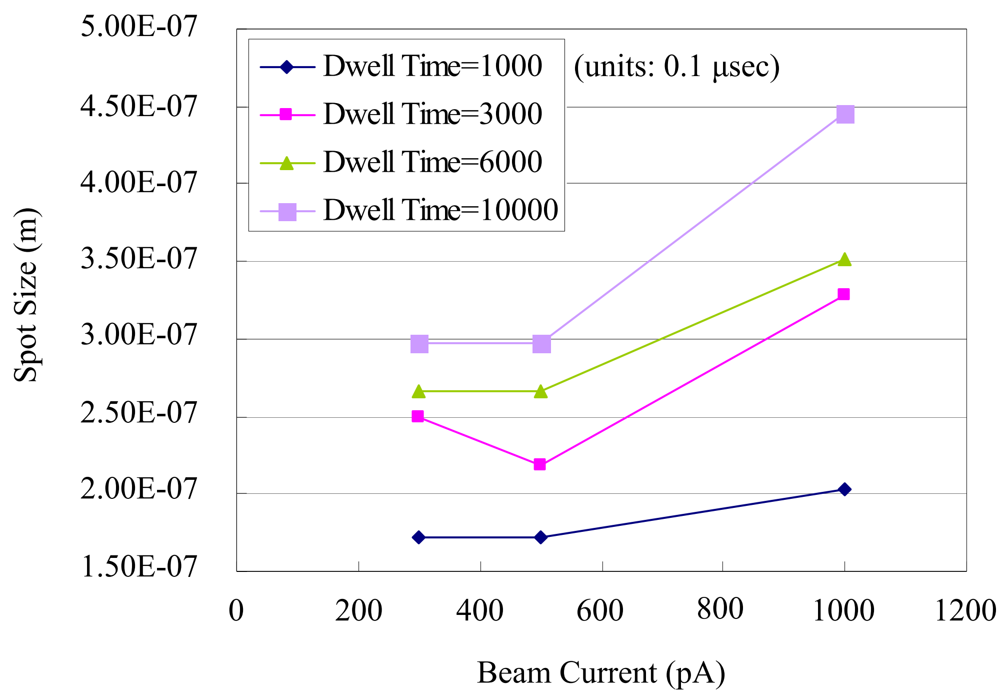

Figure 4-4: Ion-milled spot size versus beam current for various dwell time for 1200x magnification.

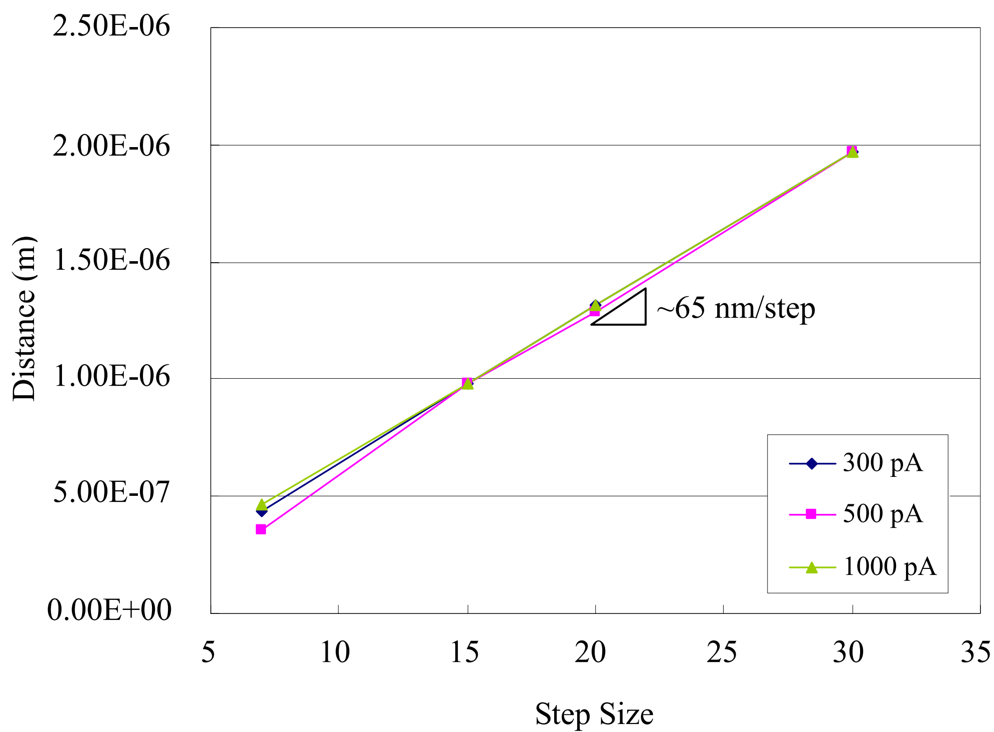

(a)

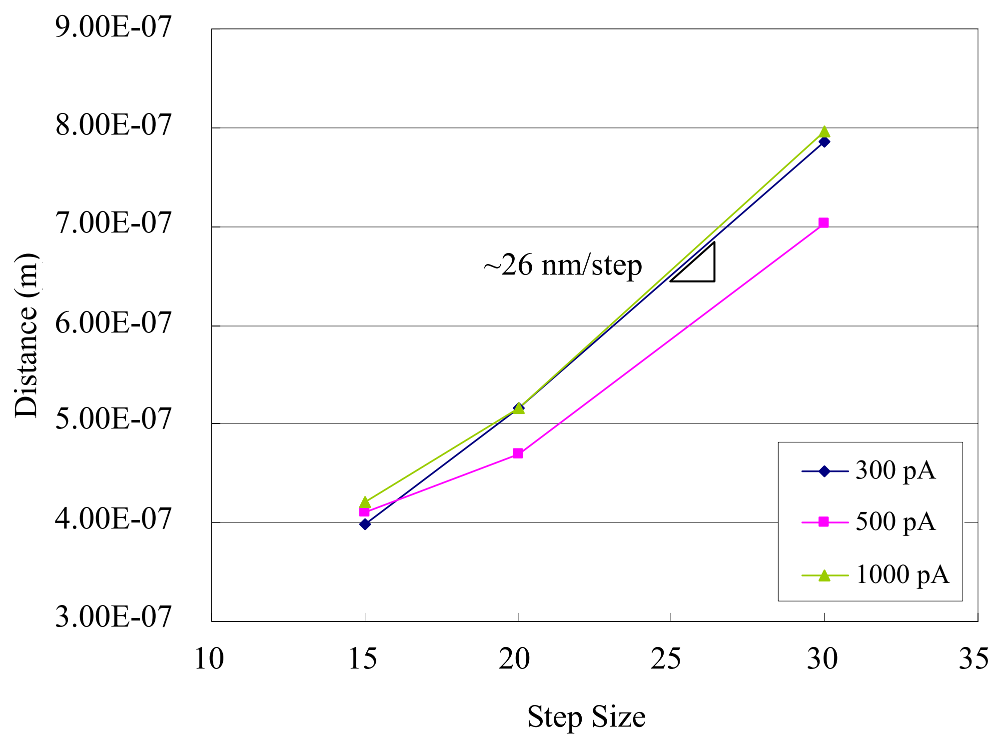

(b)

Figure 4-5: Actual distance versus pixel step size for various beam current for (a) 480x and (b) 1200x magnification.

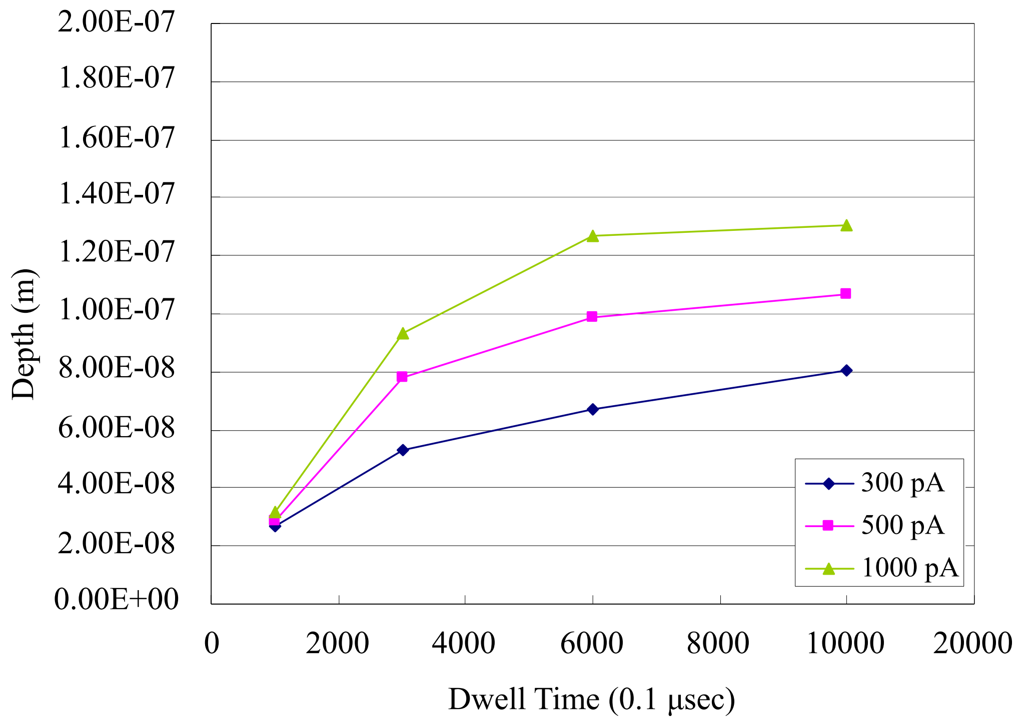

(a)

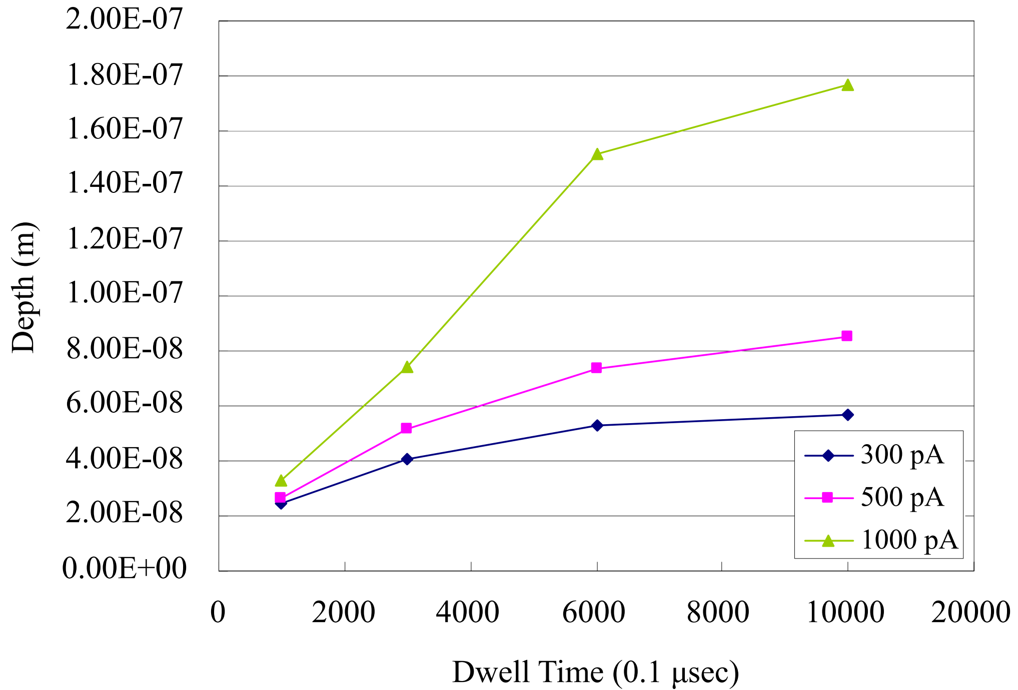

(b)

Figure 4-6: Depth versus dwell time for various beam current for (a) 480x and (b) 1200x magnification.

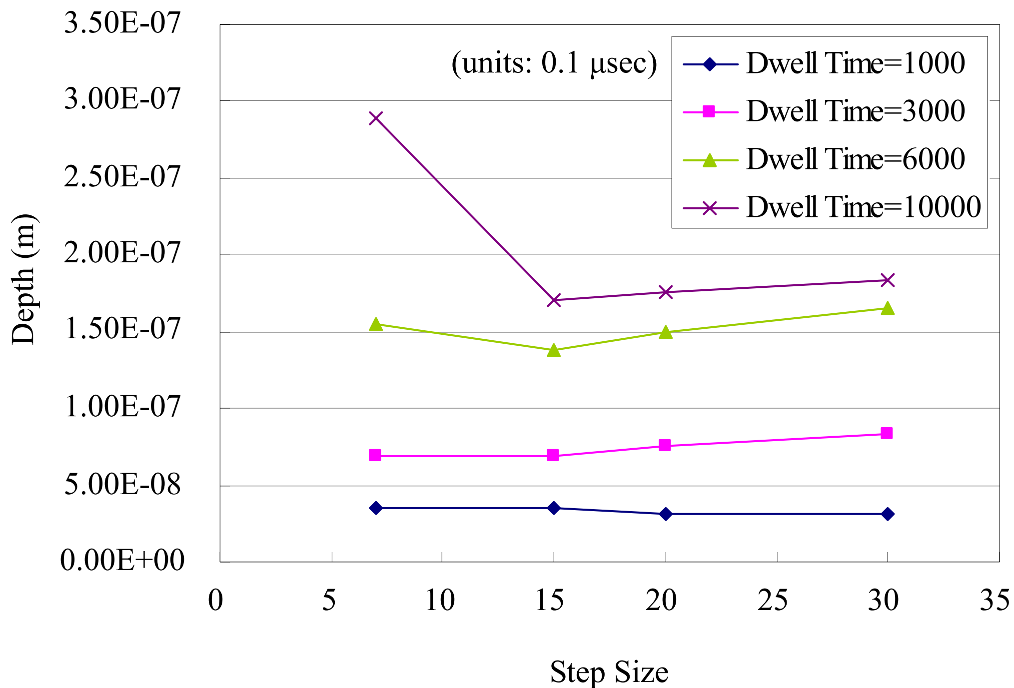

Figure 4-7: Depth versus pixel step size for various dwell time for 1200x magnification and beam current of 1 nA.

4-2 Microlens and Mask Pattern Measurement

According to the information from the test pattern measurement, the FIB parameters for the milled patterns, i.e., the Fresnel microlens and gray-scale mask, are determined. The maximum dwell time and beam current are fixed to 1 msec and 0.5 nA as discussed above. To begin with, the microlens pattern had a diameter of 100 μm and the desired depth was about 528 nm. The step size was 1 in the bitmap. The FIB-milled pattern was measured by AFM, as shown in Figure 4-8. As the figure shows, the actual depth, about 24 nm, is too small and the milled profile loses the desired shape due to the overlap of the ion-milled spot.

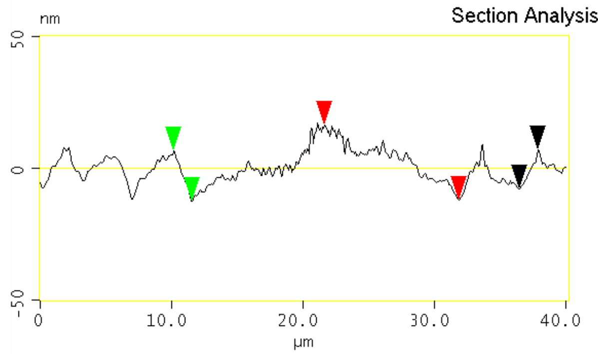

L	1.406 µm
RMS	4.232 nm
lc	DC
Ra(lc)	0.362 nm
Rmax	3.118 nm
Rz	1.586 nm
Rz Cnt	6
Radius	69.678 µm
Sigma	0.991 nm

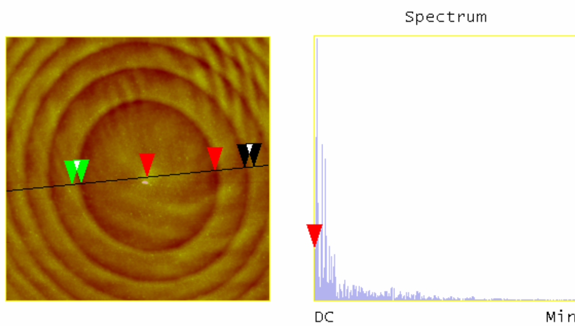

Surface distance	10.235 µm
Horiz distance(L)	10.234 µm
Vert distance	28.353 nm
Angle	0.159 °
Surface distance	1.406 µm
Horiz distance	1.406 µm
Vert distance	19.185 nm
Angle	0.782 °
Surface distance	1.406 µm
Horiz distance	1.406 µm
Vert distance	15.050 nm
Angle	0.613 °
Spectral period	DC
Spectral freq	0 /µm
Spectral RMS amp	0.728 nm

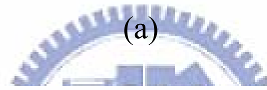

(a)

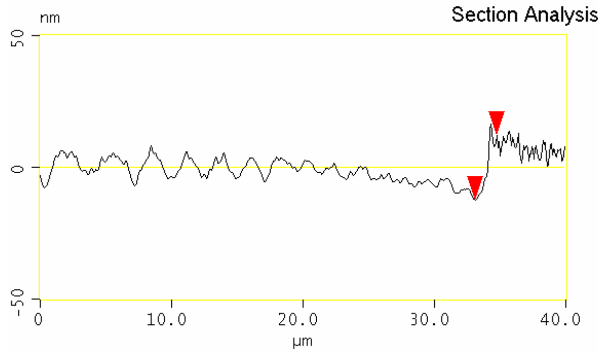

L	1.641 µm
RMS	9.833 nm
lc	DC
Ra(lc)	3.058 nm
Rmax	14.132 nm
Rz	10.418 nm
Rz Cnt	4
Radius	1.443 µm
Sigma	76.635 nm

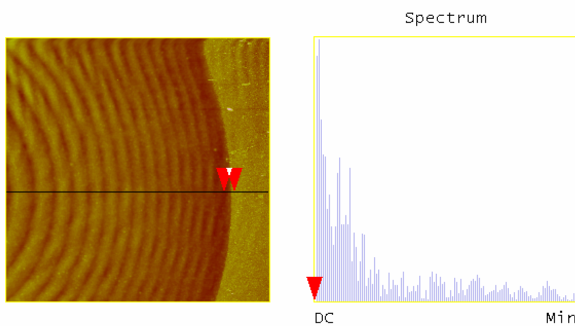

Surface distance	1.642 µm
Horiz distance(L)	1.641 µm
Vert distance	24.454 nm
Angle	0.854 °
Surface distance	
Horiz distance	
Vert distance	
Angle	
Surface distance	
Horiz distance	
Vert distance	
Angle	
Spectral period	DC
Spectral freq	0 /µm
Spectral RMS amp	0 nm

Depth

(b)

Figure 4-8: AFM measurement of the (a) middle region and (b) right-side region of the microlens pattern of diameter 100 µm.

The shallow milled depth was caused by the limited milling time allowed for each run. In this case, the depth problem can be solved by reducing the pattern diameter. The loss of fine structures in the outer rings in the milled pattern was caused by the overlapped ion spot. Therefore, blank pixels can be inserted in the bitmap figures for compensation. Figure 4-9 shows the measurement of a sample with a diameter of 50 μm and two inserted blank pixels. The whole profile of the pattern is shown in Figure 4-10. As the figures show, the profile is deeper than the non-compensated one and profile is closer to the design. But the depth of the pattern, about 88 nm, is still not enough, so the area of the milled region must be reduced again.

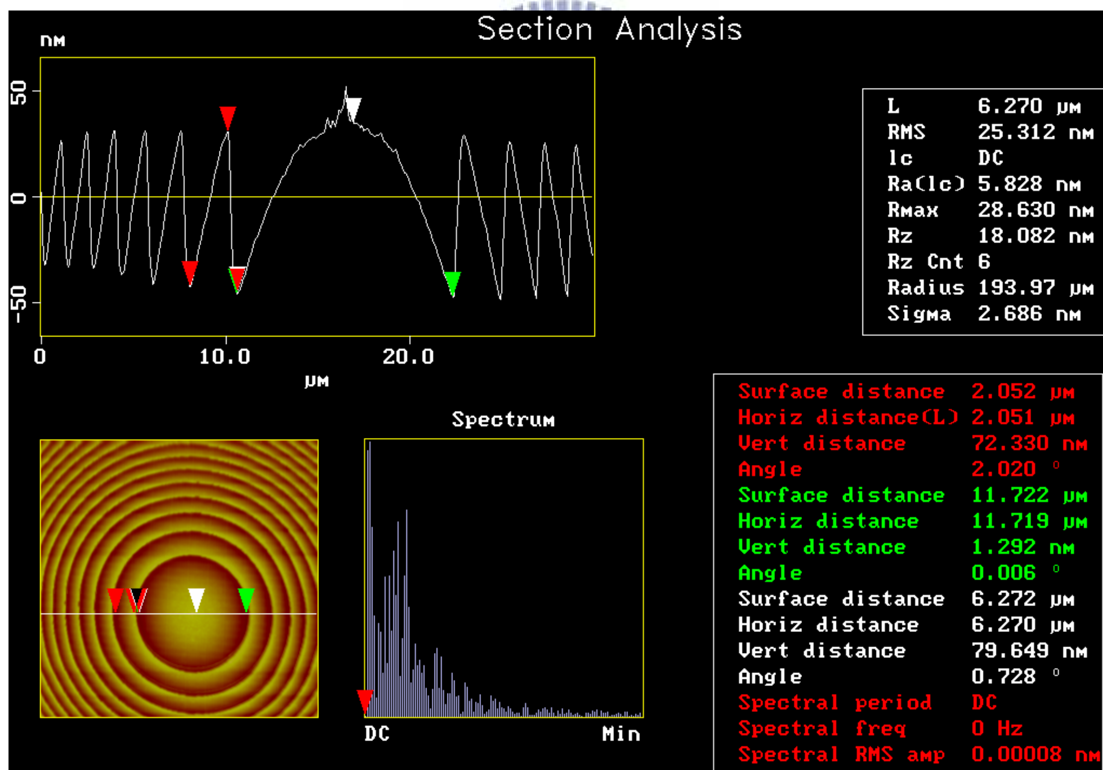

(a)

Figure 4-9: AFM measurement of the (a) middle region and (b) right-side region of the microlens pattern of diameter 50 μm.

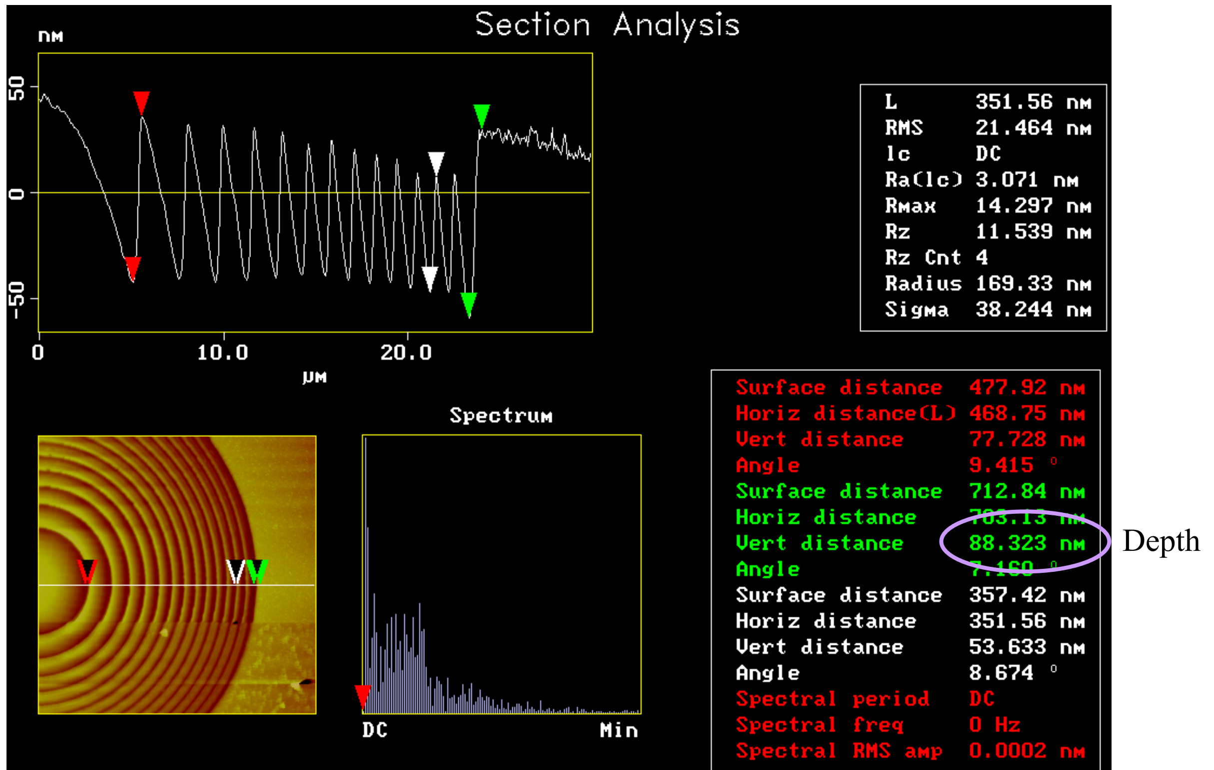

(b)

Figure 4-9: (Continued) AFM measurement of the (a) middle region and (b) right-side region of the microlens pattern of diameter 50 μm.

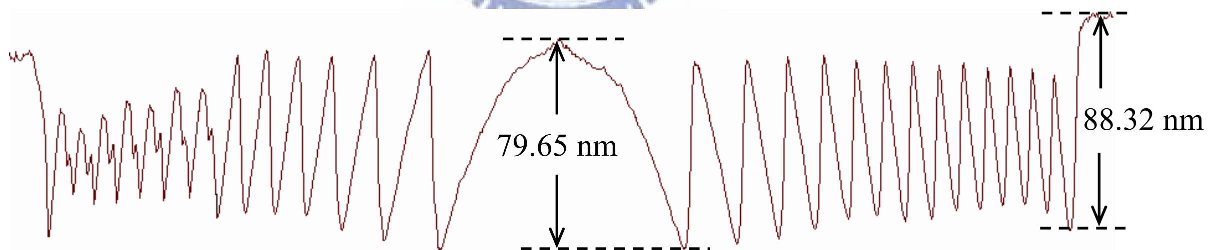

Figure 4-10: AFM profile of the microlens pattern of diameter 50 μm.

For different magnification and pattern diameter, the total volume removed by the focused ion beam should be equal for the same dwell time and ion current. Based on this principle, the depth of the milled pattern can be roughly calculated as

$$L_1^{\ 2} \times d_1 = L_2^{\ 2} \times d_2 = V_{removed}\,, \tag{4-1}$$

where L_1 and L_2 represent the pattern diameters in two different magnification, and d_1

and d_2 represent the corresponding depth of the FIB-milled patterns. The desired depth of the microlens and gray-scale mask is about 530 nm and 170 nm respectively; the pattern diameter of the lens and mask can be calculated as 20 μm and 30 μm. To avoid the overlap caused by the reduced pattern diameter, seven blank pixels were inserted into the 20-μm microlens pattern and four blank pixels were inserted into the 30-μm gray-scale mask pattern. The AFM measurement results of the microlens are shown in Figure 4-11. Figure 4-12 shows the AFM measurement results of the gray-scale mask, and Figure 4-13 shows the whole profile of the mask. As the figures show, the depth of the gray-scale mask, about 211 nm, is a little larger than the desired depth, 170 nm; the depth of the microlens, about 525 nm, is close to the desired depth, 530 nm. So the pattern diameter of the mask should be tuned to match the design. Besides, the height of the outer rings is decreased due to the overlap, so more blank pixels must be inserted into the bitmap figures.

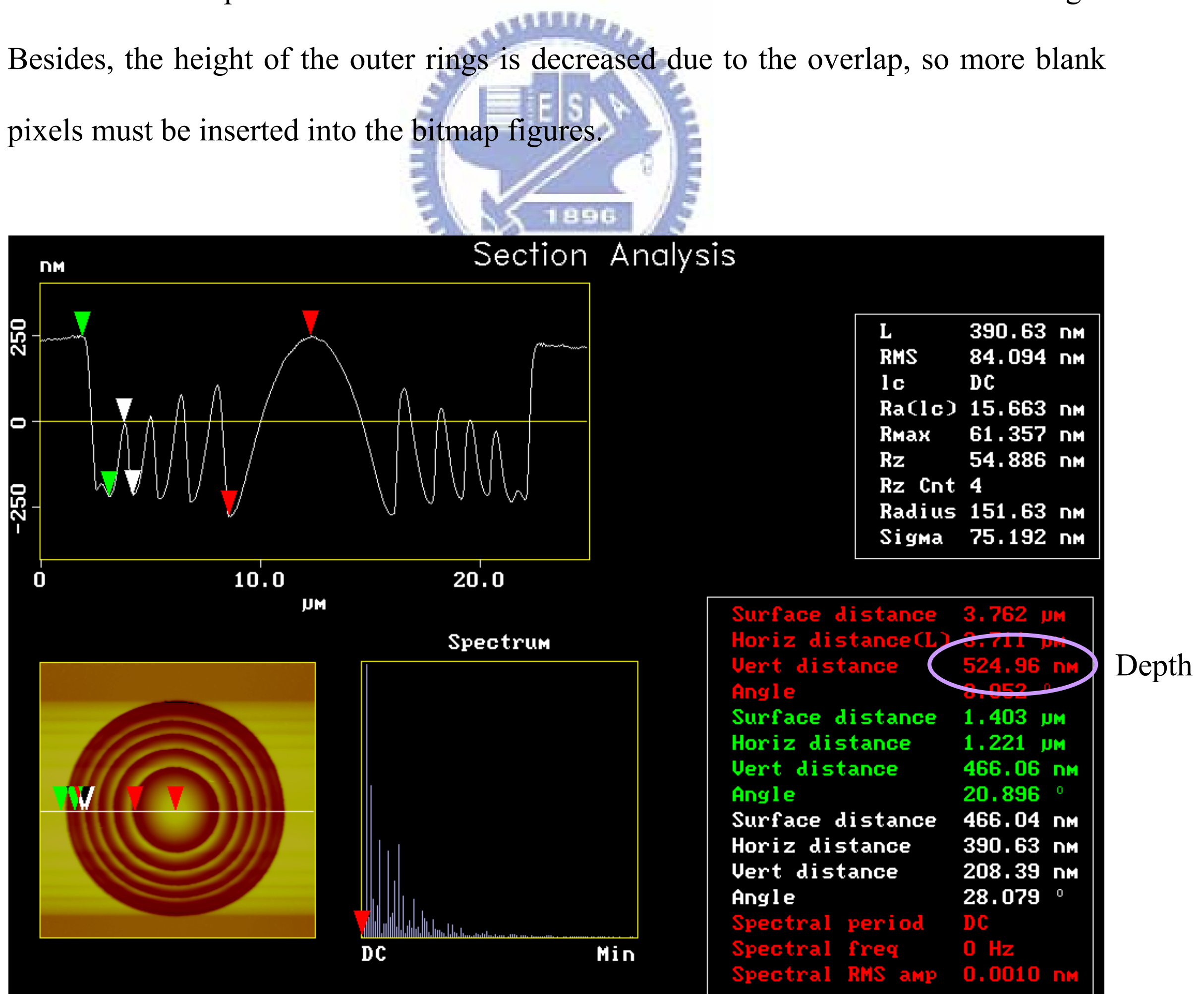

Figure 4-11: AFM measurement of the microlens pattern of diameter 20 μm.

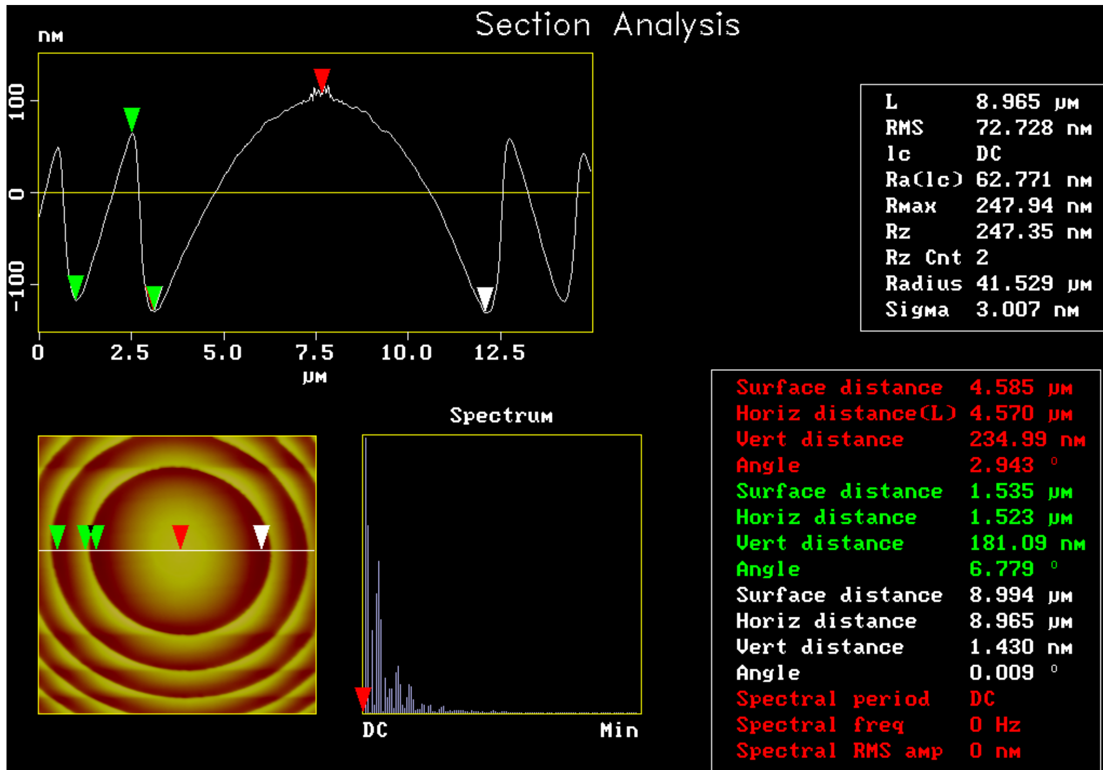

(a)

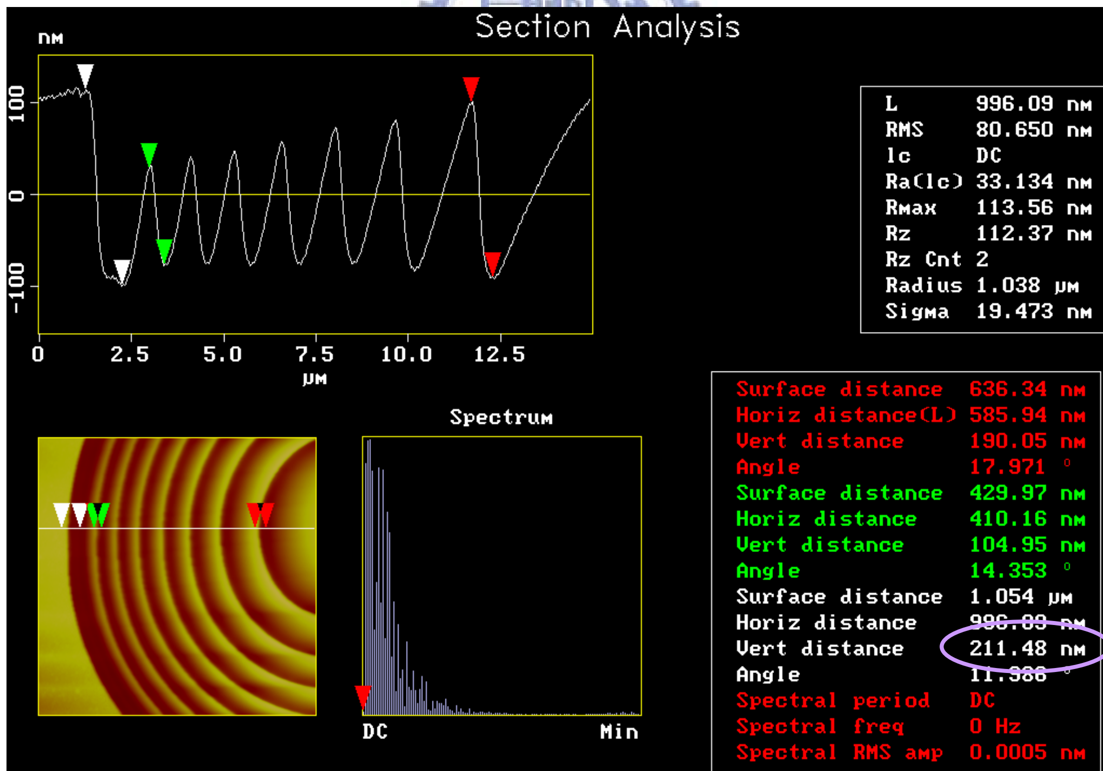

(b)

Figure 4-12: AFM measurement of the (a) middle region and (b) left-side region of the mask pattern of diameter 30 μm.

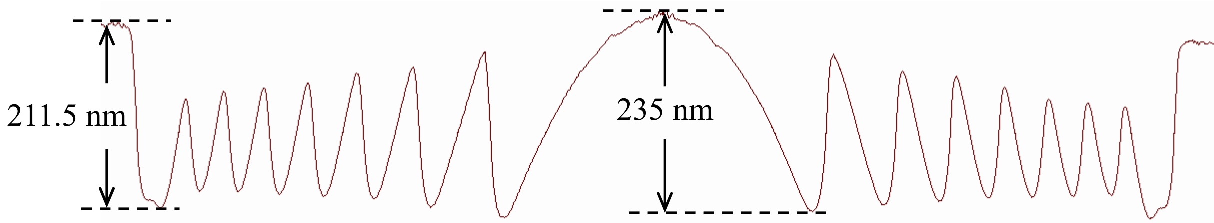

Figure 4-13: AFM profile of the mask pattern of diameter 30 μm.

The diameter of the third compensated patterns was 20 μm for the microlens and 35 μm for the gray-scale mask. In addition, ten blank pixels were inserted into the microlens pattern and six blank pixels into the gray-scale mask pattern. The 2D and 3D profile of the patterns are shown in Figure 4-14 and 4-15, respectively. The roughness analysis of the patterns is shown in Figure 4-16 to be about 3 to 4 nm, which is suitable for optical components. As the figures show, the depth of the microlens and mask was measured as 530 nm and 180 nm respectively, which is close to the desired value. But some overlap issues still cause the reduced height of the outer blazing rings. So, inserting more blank pixels must be considered to avoid the occurrence of the overlap. Figures 4-17 and 4-18 show the measured profiles of the nitride microlens and gray-scale mask compared with the designed 2D profiles, respectively.

Finally, the relation between the depth and pattern size, i.e., ion-scanned area, is shown in Figure 4-19. The measured data can be fitted by the curve

$$\text{depth} \times \text{pattern size} = c\,, \qquad (4\text{-}2)$$

where c is a constant and can be calculated as 1.9×10^{2} μm^{3}, as shown in the figure.

In summary, the Fresnel microlens in silicon nitride and the gray-scale mask for the microlens in AZ4620 are fabricated. The profile of the patterns is close to the design. In addition, the loss of fine structures can be overcome by inserting blank pixels into the bitmap figures.

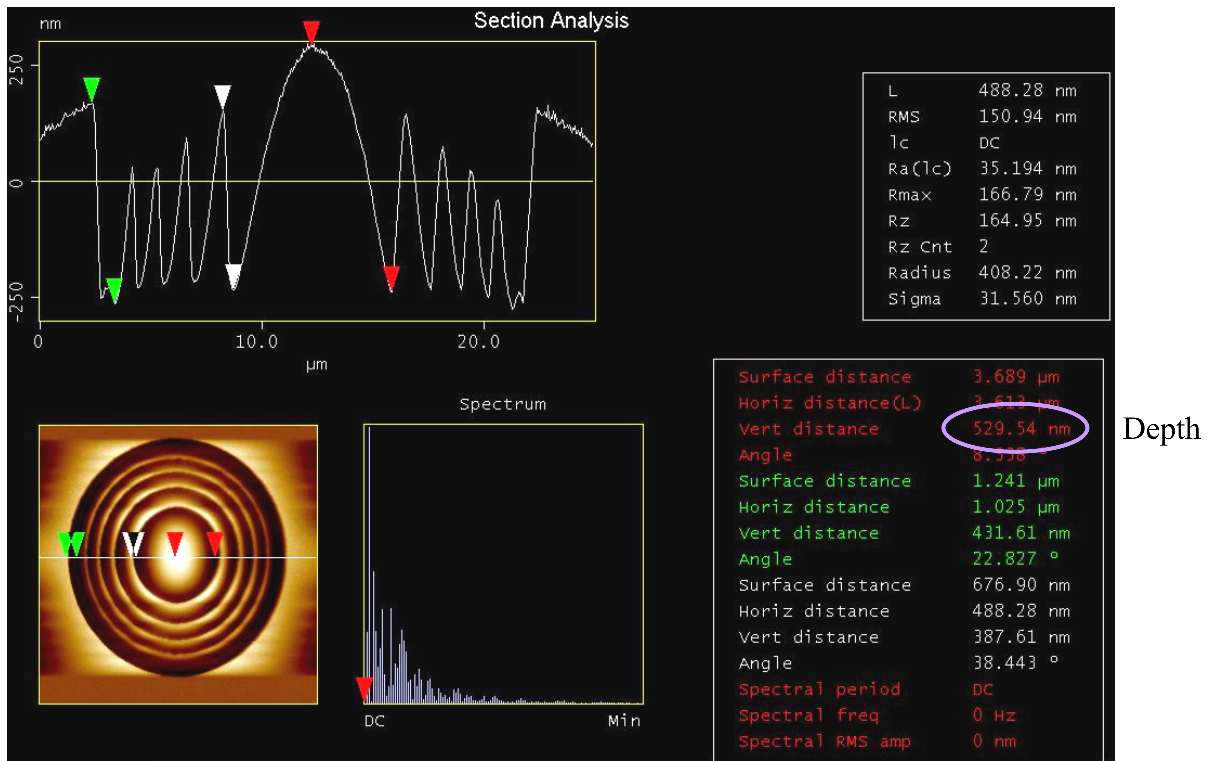

(a)

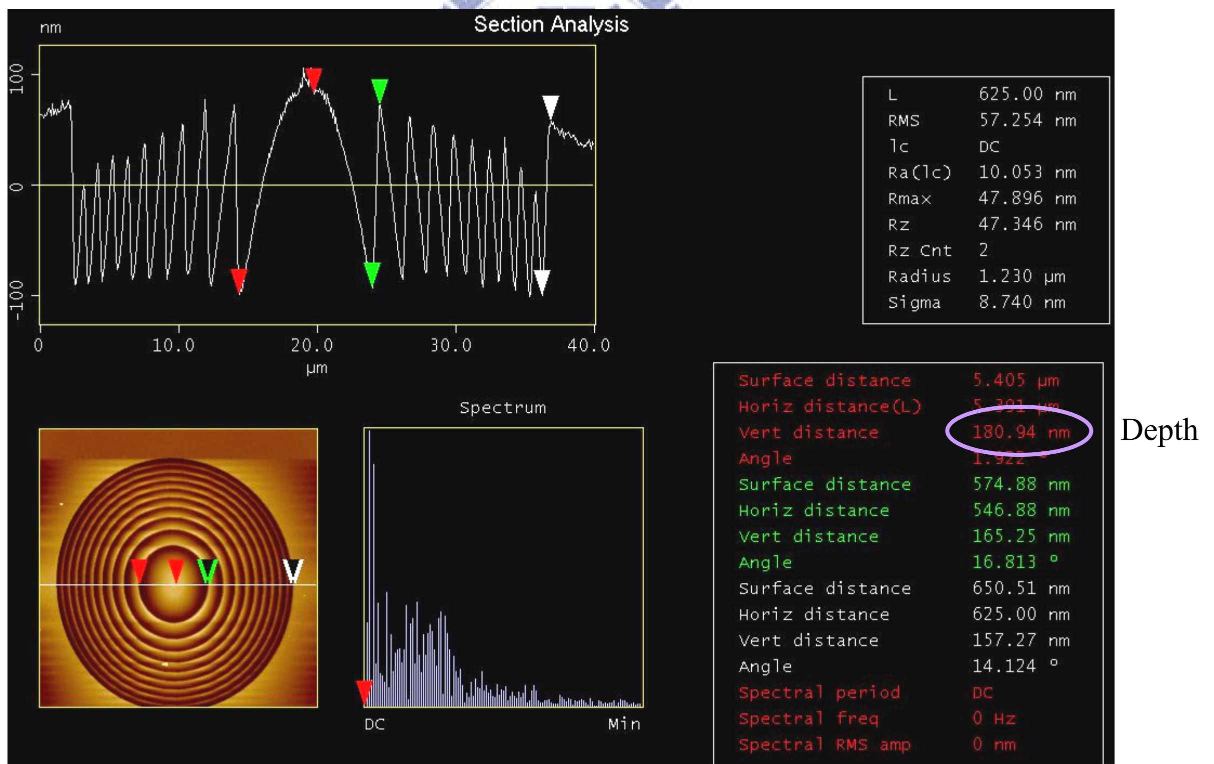

(b)

Figure 4-14: 2D profile of the (a) microlens and (b) gray-scale mask.

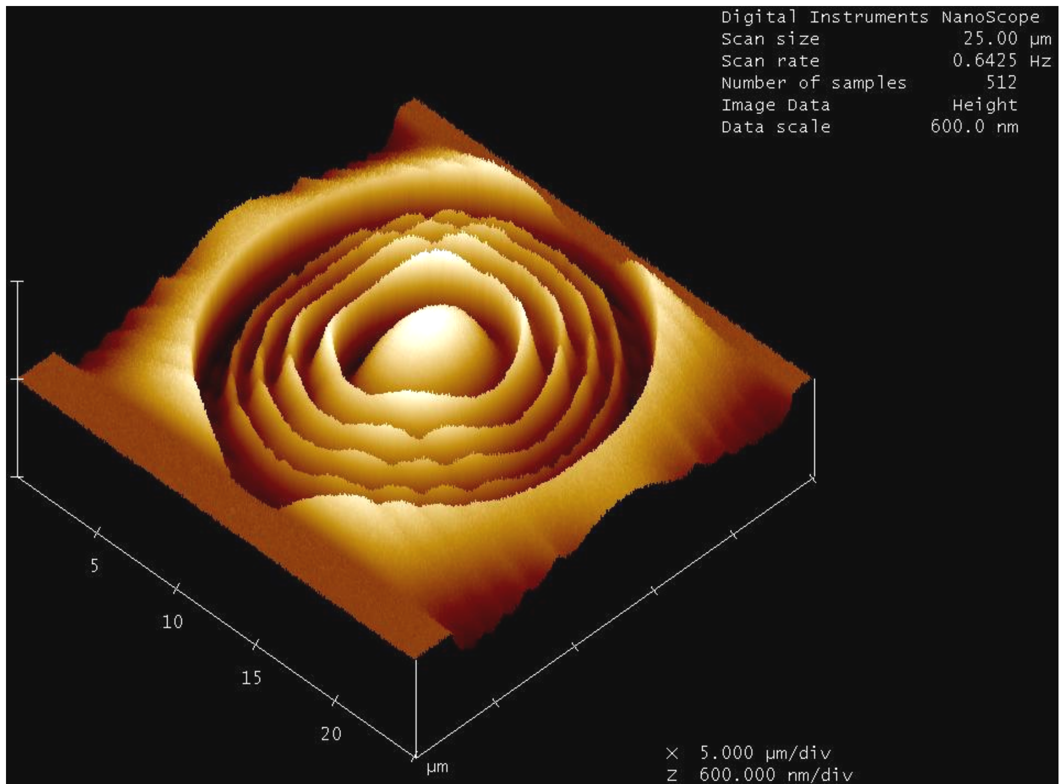

(a)

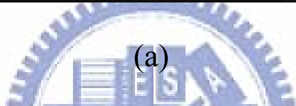

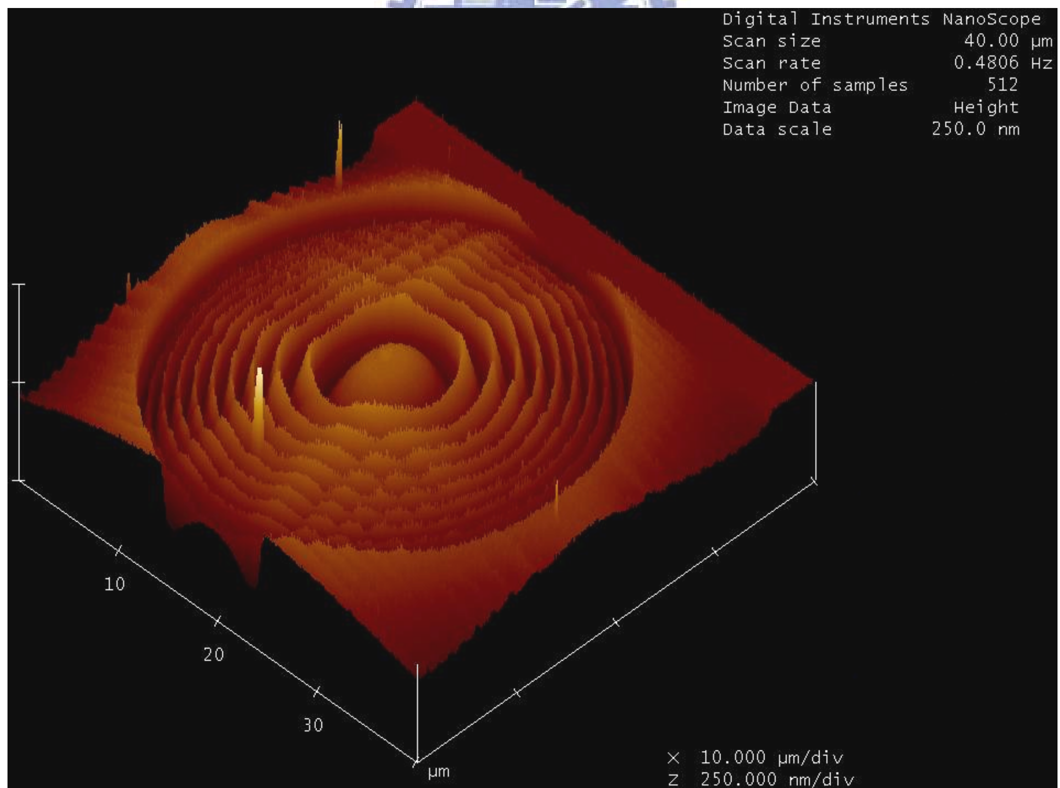

(b)

Figure 4-15: 3D profile of the (a) microlens and (b) gray-scale mask.

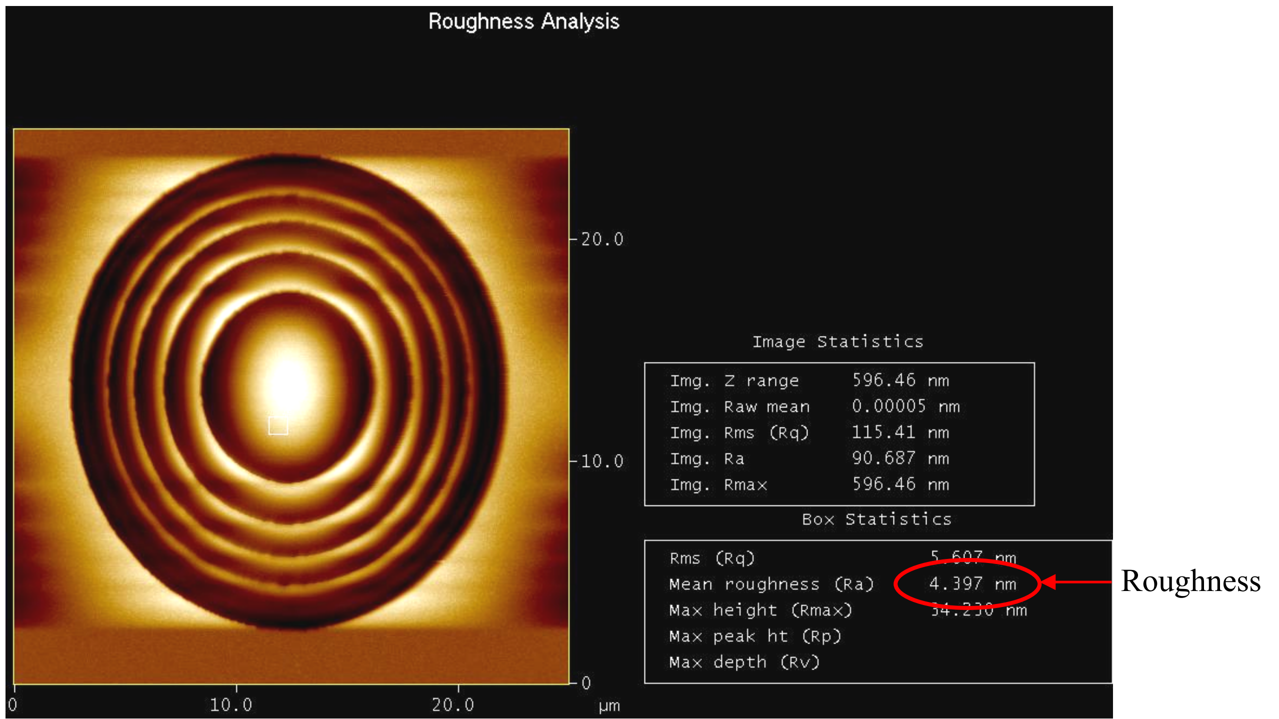

(a)

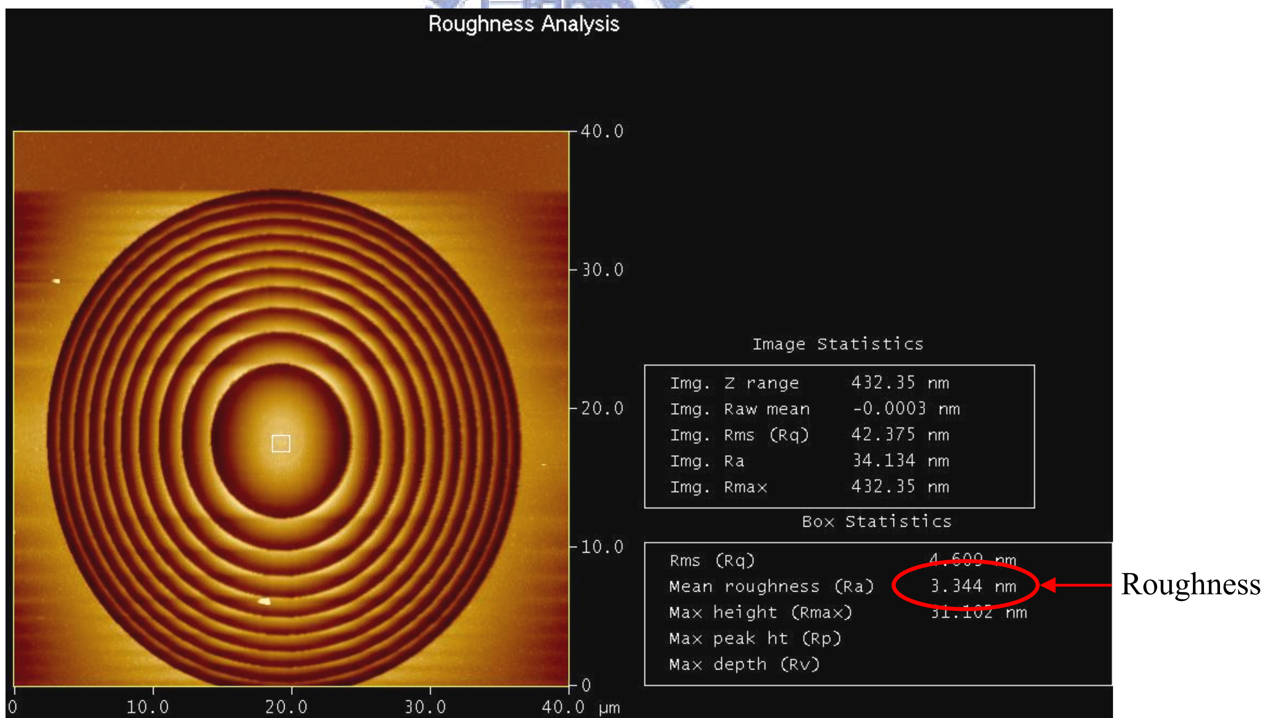

(b)

Figure 4-16: Roughness of the (a) microlens and (b) gray-scale mask.

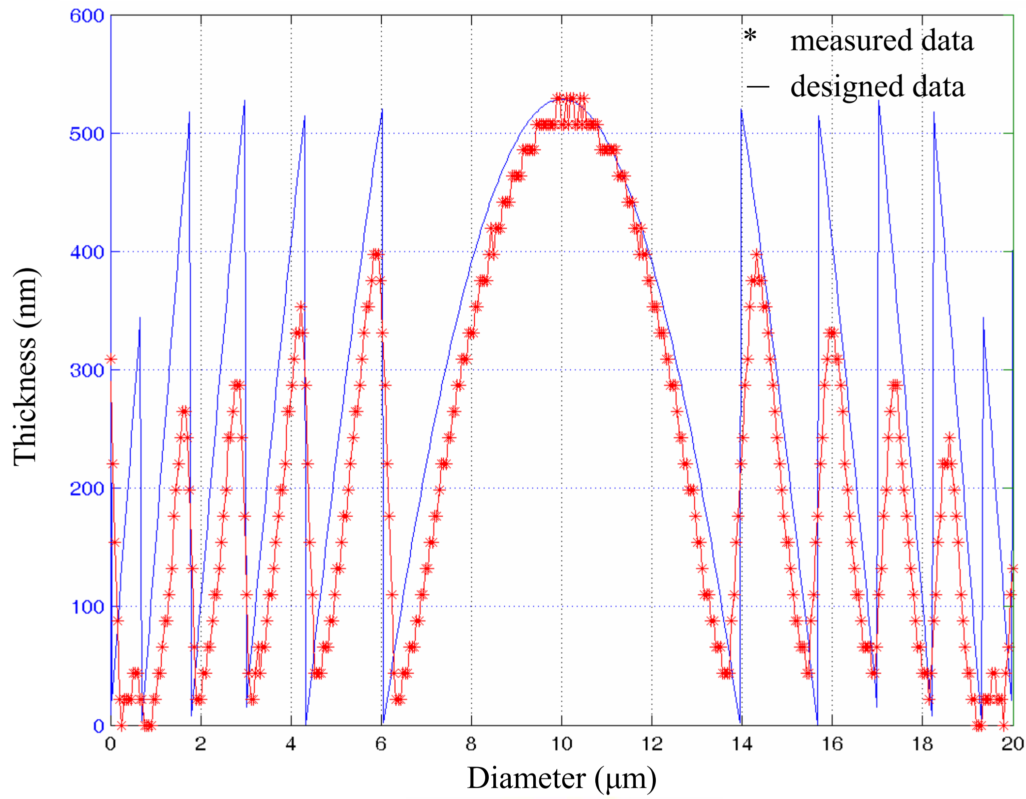

Figure 4-17: Comparison between the measured profile and designed profile for the silicon nitride microlens of diameter 20 μm.

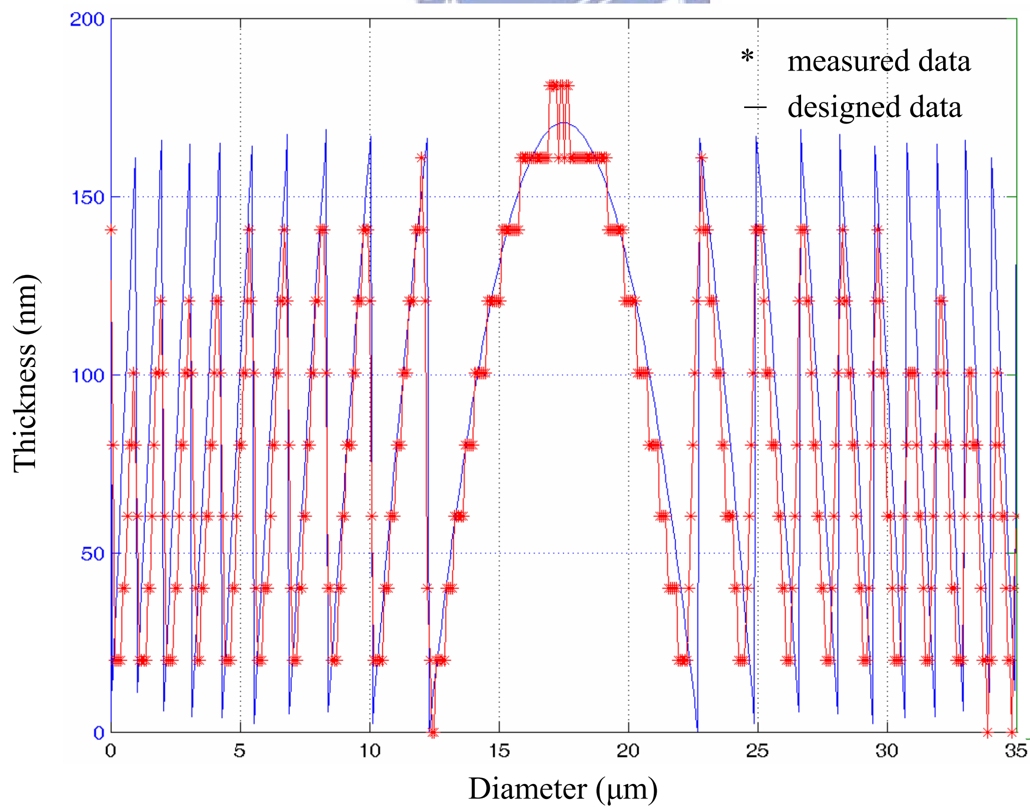

Figure 4-18: Comparison between the measured profile and designed profile for the gray-scale mask of diameter 35 μm.

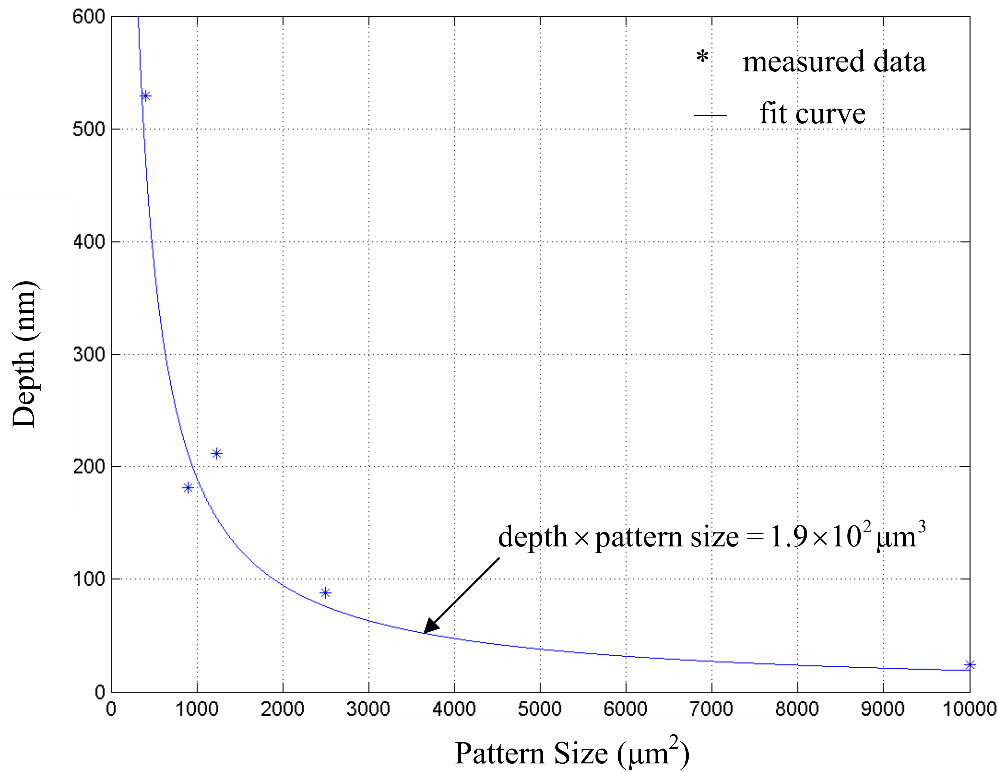

Figure 4-19: Pattern size versus milled depth.

4-3 Optical Experiment

The Fresnel microlens was directly patterned in the silicon nitride film by the FIB system. Optical experiment was conducted to verify the performance of the microlens, as shown schematically in Figure 4-20. First, a proper distance was selected to ensure that the pattern of microlens is clearly displayed on the screen. Then, the microlens or the objective lens was moved a certain distance to make the pattern on the screen shrink to a bright point, i.e., a focused spot. Therefore, the distance is the focal length of the microlens fabricated by the focused ion beam. After a series of optical experiments, the focal length was measured as about 12 μm, and the N.A. value of the microlens can be calculated as

$$\mathrm{N.A.} = \sin(\tan^{-1}(\frac{10\ \mu\mathrm{m}}{12\ \mu\mathrm{m}})) \approx 0.64\,. \tag{4-3}$$

In addition, the screen was replaced by a CCD camera to check the profile of the focused spot. Figure 4-21 shows the image of the focused spot captured by the CCD camera. The intensity profile of the focused spot is shown in Figure 4-22, and the cross-section of the profile is shown in Figure 4-23, respectively. The FWHM (full-width at half-maximum) of the focused spot in the x-direction and y-direction can be calculated as about 0.64 μm and 0.66 μm, respectively. Therefore, the fabricated microlens is symmetric. The diffraction limit of a 0.64 N.A. lens is

$$d \approx \frac{0.5\lambda}{\text{N.A.}} = \frac{0.5 \times 0.633\ \mu\text{m}}{0.64} \approx 0.494\ \mu\text{m}, \tag{4-4}$$

where λ is the wavelength of the laser used for the experiment, and N.A. is the numeric aperture of the microlens. Therefore, the numerical aperture, 0.64, of the fabricated microlens in silicon nitride is close to the specification, 0.65, of a DVD optical pick-up head. But the measured spot size of the focused spot is larger than the diffraction limit of the lens. The reason is that the height of the outer blazing rings is a little different from that of the design. The reduced height causes the reduction of the focusing ability.

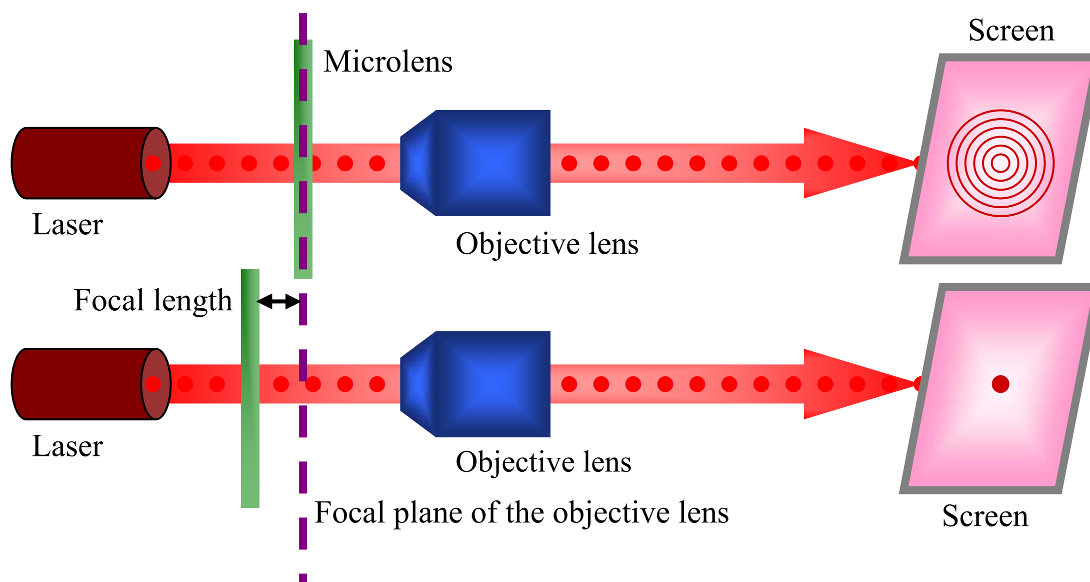

Figure 4-20: Schematic diagram of the optical measurement.

Figure 4-21: Image of the focused spot on the CCD camera.

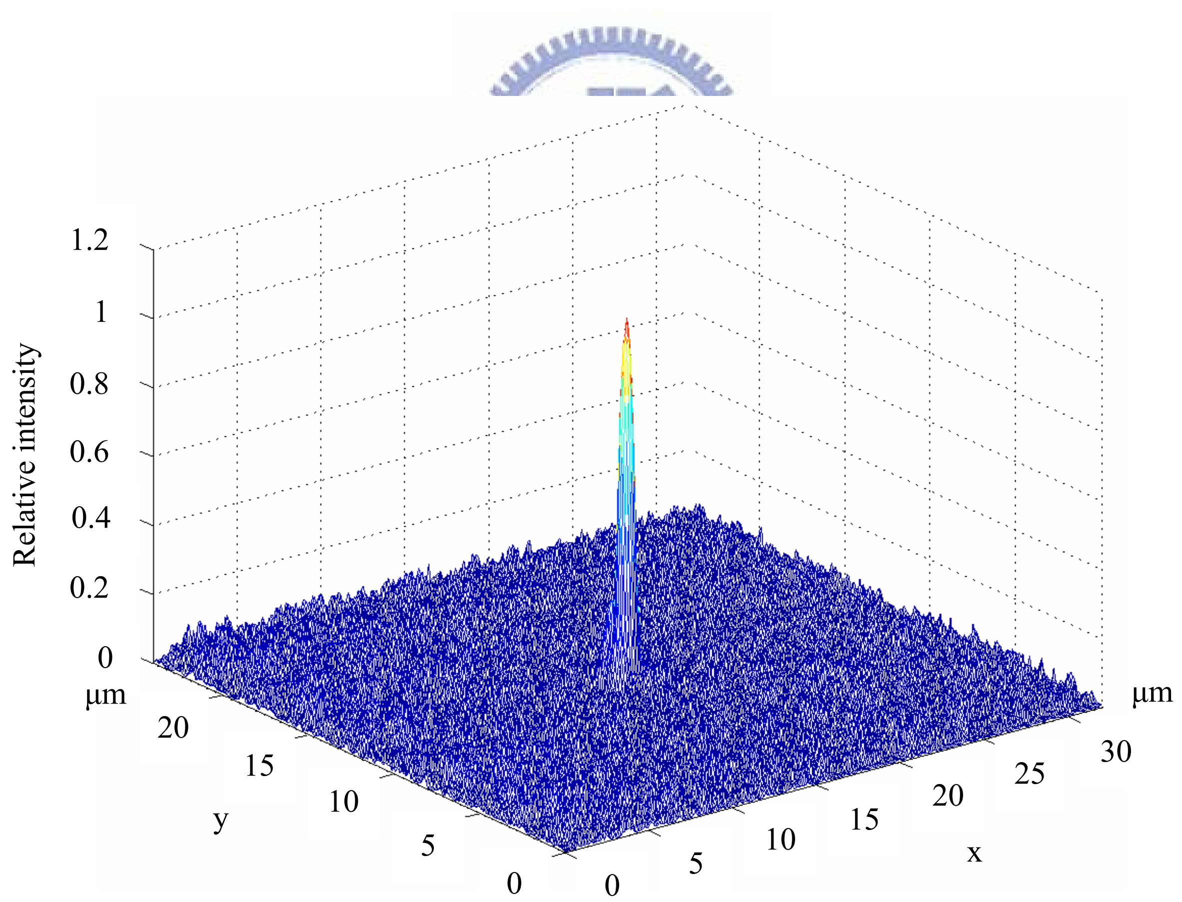

Figure 4-22: Intensity profile of the focused spot.

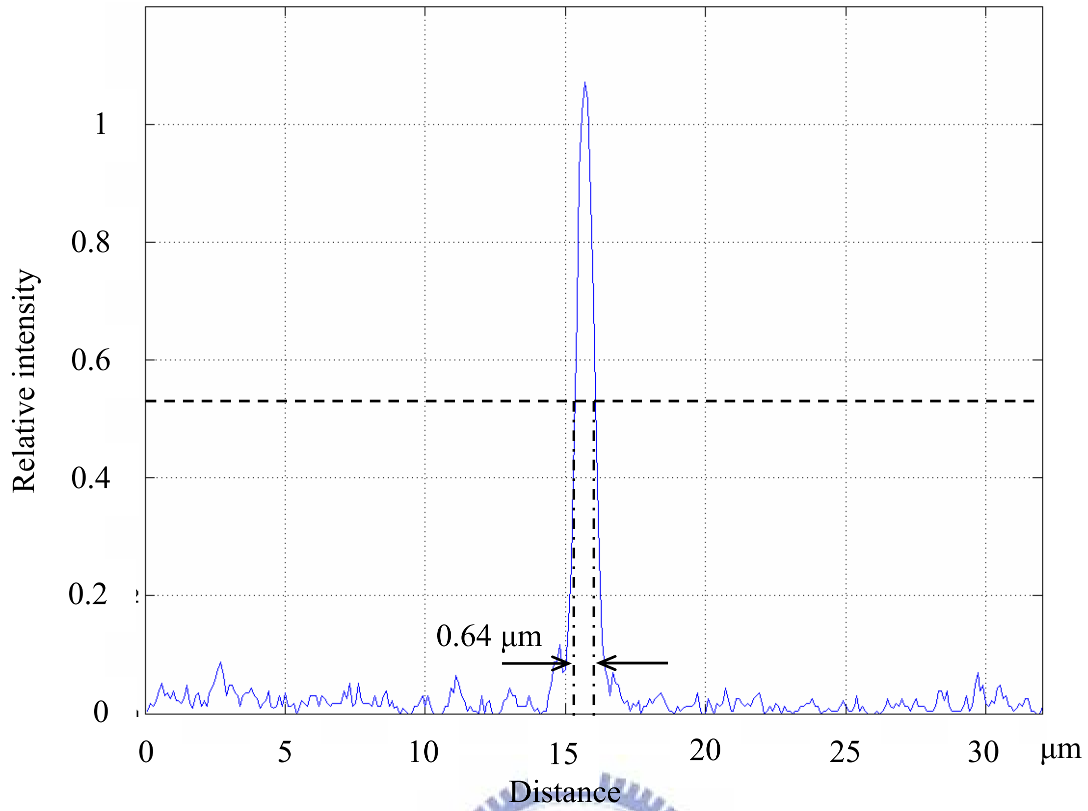

(a)

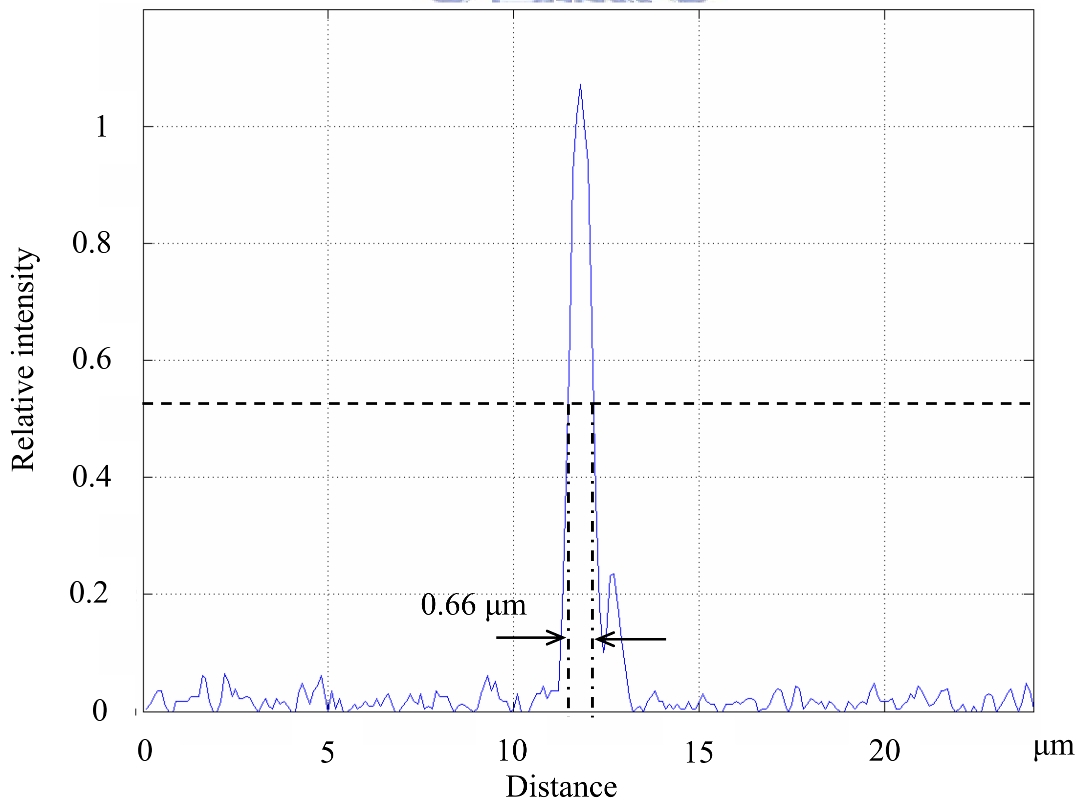

(b)

Figure 4-23: Cross-section of the intensity profile in (a) the x-direction and (b) the y-direction.

4-4 Summary

The relations between the FIB parameters, such as step size, dwell time, passes, and Z-size, etc., have been obtained through the test patterns. The profiles of the Fresnel microlens and gray-scale mask in silicon nitride fabricated by FIB milling has also been measured by AFM. Through the optical experiment, the numerical aperture of the fabricated microlens in silicon nitride is measured as 0.64, close to the specification of a DVD optical pick-up head. However, due to the reduced height of the outer rings, the measured spot size of the focused spot is larger than the diffraction limit of the lens.

Chapter 5 Conclusion and Future Work

5-1 Conclusion

In this research, the FIB-milled Fresnel microlens and gray-scale mask are proposed and fabricated. Silicon nitride is used as the material of the mask and lens, and positive photoresist AZ4620 is also used as the material of the microlens. The numeric aperture of the microlens on the nitride film is measured as 0.64, close to the specification, 0.65, of the DVD pick-up head. Due to the reduced height of the outer rings in the microlens, the spot size of the focal point is about 0.64 μm, larger than the diffraction limit of 0.494 μm of the lens. More blank pixels can be added into the bitmap pattern to avoid the ion beam spot overlap, which is the reason of the reduced height. In addition, the microlens can also be produced by the contact-mode photolithography. Moreover, the photoresist model of AZ4620 has been built for the exposure process.

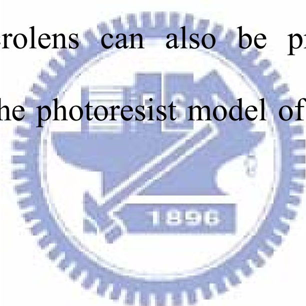

5-2 Future Work

In the lens design of Chapter 2, the assumption that the light passes through the lens straightly leads to errors in the lens profile $h(r)$. The profile can be adjusted by the optical simulation tools, such as ZEMAX. In addition, a new compensated gray-scale pattern is being developed, in which more blank pixels are added to reduce the influence of the overlap. In the future, the deposition of the FIB system can be considered to fabricate the gray-scale mask on the transparent substrate, such as glass or quartz wafer. The FIB-deposited materials include platinum (Pt), tungsten (W), or some insulators. The extinction coefficient of metallic materials is much larger than that of silicon nitride, so the thickness deposited by FIB can be reduced. In addition, the transparent substrate is also the solution of fragile samples caused by the KOH wet etching process.

References

[1] L. Y. Lin, J. L. Shen, S. S. Lee, and M. C. Wu, "Realization of novel monolithic free-space optical disk pickup heads by surface micromachining," *Optics Letters*, Vol. 21, No. 2, pp. 155-7, 1996.

[2] S. Sinzinger and J. Jahns, *Microoptics*, Second edition, Wiley-VCH, pp. 133-134, 2003.

[3] C. R. King, L. Y. Lin, and M. C. Wu, "Out-of-plane refractive microlens fabricated by surface micromachining," *IEEE Photonics Technology Letters*, Vol. 8, No. 10, pp. 1349-51, 1996.

[4] T. R. Jay and M. B. Stern, "Preshaping photoresist for refractive microlens," *Optical Engineering*, Vol. 33, No. 11, pp. 3552-5, 1994.

[5] B. P. Keyworth, D. J. Corazza, J. N. McMullin, and L. Mabbott, "Single-step fabrication of refractive microlens arrays," *Applied Optics*, Vol. 36, No. 10, pp. 2198-202, 1997.

[6] S. Biehl, R. Danzebrink, P. Oliveira, and M. A. Aegerter, "Refractive microlens fabrication by ink-jet process," *Journal of Sol-Gel Science and Technology*, Vol. 13, No. 1, pp. 177-82, 1998.

[7] H. Sankur, E. Motamedi, R. Hall, W. J. Gunning, and M. Khoshnecisan, "Fabrication of refractive microlens array," *Proc. SPIE, Micro-Optics Micromechanics and Laser Scanning and Shaping*, Vol. 2383, pp. 179-83, 1995.

[8] M. C. Wu, "Micromachining for optical and optoelectronic systems," *Proceedings of the IEEE*, Vol. 85, No. 11, pp. 1833-56, 1997.

[9] C. M. Waits, A. Modafe, and R. Ghodssi, "Investigation of gray-scale technology for large area 3D silicon MEMS structures," *Journal of Micromechanics and Microengineering*, Vol. 13, No. 2, pp. 170-7, 2003.

[10] W. Daschner, P. Long, R. Stein, C. Wu, and S. H. Lee, "Cost-effective mass fabrication of multilevel diffractive optical elements by use of a single optical exposure with a gray-scale mask on high-energy beam-sensitive glass," *Applied Optics*, Vol. 36, No. 20, pp. 4675-80, 1997.

[11] M. R. Wang and H. Su, "Laser direct-write gray-level mask and one-step etching for diffractive microlens fabrication," *Applied Optics*, Vol. 37, No. 32, pp. 7568-76, 1998.

[12] Giannuzzi, A. Lucille, and F. A. Stevie, *Introduction to Focused Ion Beam: Instrumentation, Theory, Techniques, and Practice*, New York Kluwer Academic Publishers, pp. 1-12 and 107-8, 2005.

[13] Y. Fu and N. K. A. Bryan, “Influence of astigmatism on the fabrication of diffractive structures by use of focused ion-beam milling,” *Optics Express*, Vol. 12, No. 17, pp. 3954-66, 2004.

[14] T. Fujii, K. Iwasaki, M. Munekane, T. Takeuchi, M. Hasuda, T. Asahata, M. Kiyohara, T. Kogure, Y. Kijima, and T. Kaito, “A nanofactory by focused ion beam,” *Journal of Micromechanics and Microengineering*, Vol. 15, No. 10, pp. S286-91, 2005.

[15] M. Hayles and M. Dufek, *xT Nova NanoLab User's Manual*, Fourth edition, FEI company, pp. 33-7, 2005.

[16] M. LeCompte, X. Gao, and D. W. Prather, “Photoresist characterization and linearization procedure for the gray-scale fabrication of diffractive optical elements,” *Applied Optics*, Vol. 40, No. 32, pp. 5921-7, 2001.

[17] M. J. Madou, *Fundamentals of Microfabrication: The Science of Miniaturization*, Second edition, CRC Press, USA, pp. 299-301, 2002.